# COMBINATORIAL STUDY OF THE LI-NI-MN-CO OXIDE PSEUDO-QUATERNARY SYSTEM FOR USE IN LI-ION BATTERY MATERIALS RESEARCH

by

Colby Brown

Submitted in partial fulfillment of the
requirements for the degree of
Master of Science

at

Dalhousie University
Halifax, Nova Scotia
November 2014

# Table of Contents

# List of Tables

# List of Figures

# Abstract

Samples of the Li-Ni-Mn-Co-O system were prepared using a combinatorial and high throughput method at two separate cooling rates and were subsequently studied by X-ray diffraction to determine the crystal structure of each sample. Two separate series were investigated. The first series of samples spanned the entire pseudo-ternary phase diagram planes defined at the fractional cobalt metal contents of 10 %, 20 % and 30 % in the Li-Ni-Mn-Co-O system and the second series spanned the entire Li-Co-Mn-O pseudo-ternary phase diagram. Retrieved crystal structure data from fitting the XRD patterns of every sample were used to map out the phase diagrams of the targeted regions. Two large single-phase regions were observed in the system: the layered region and cubic spinel region. These regions were each found to stretch over a wide range of compositions in the Li-Ni-Mn-Co-O pseudo-quaternary system and had complex coexistence regions existing between them. Sample cooling rate was determined to have a significant effect on the position of phase boundaries to single-phase regions. Materials contained in these systems are of high interest for improved cathode materials for use in lithium-ion batteries. The results of this thesis are intended to guide further research by mapping out the structures of phases existing in the regions of interest.

# List of Abbreviations and Symbols Used

| | |
|---|---|
| $2\theta$ | Scattering angle |
| $2\theta_m$ | Diffraction angle of the monochromator |
| $\eta$ | Lorentzian componenent in the pseudo-Voigt function |
| $\phi$ | Phase difference between wave vectors |
| $\Psi(\boldsymbol{r}, t)$ | Wave function of two superimposed reflected waves of $\psi(\boldsymbol{r}, t)$ out of phase by $\phi$ |
| $\psi(\boldsymbol{r}, t)$ | Reflected plane waves from lattice |
| $\lambda$ | Wavelength |
| $\boldsymbol{a}_i$ | Lattice primitive vectors |
| $\boldsymbol{b}_i$ | Reciprocal lattice primitive vectors |
| $\boldsymbol{d}$ | Displacement vector between adjacent atoms in a lattice |
| $DW$ | Debye-Waller factor |
| EV | Electric vehicle |
| $F$ | Geometrical structure factor |
| $F_k$ | Sample scattering X-ray diffraction intensity for the k-th peak |
| FWHM | Full width at half maximum |
| $G$ | Gaussian function |
| $\boldsymbol{G}$ | Reciprocal lattice vector |
| $H_k$ | FWHM of k-th X-ray diffraction peak |
| $(hkl)$ | Miller index for diffraction planes |
| ICP | Inductively coupled plasma optical emission spectroscopy |
| $I_k$ | Calculated X-ray diffraction intensity for the k-th peak |
| $I'_k$ | Integrated peak intensity for the k-th X-ray diffraction peak |
| JCPDS | Joint Committee on Powder Diffraction Standards |

| | |
|---|---|
| $\boldsymbol{k}_f$ | Wave vector of diffracted beam |
| $\boldsymbol{k}_i$ | Wave vector of incident beam |
| $L$ | Lorentz function |
| $L'$ | Lorentz correction factor |
| $M$ | XRD machine peak broadening function |
| $P$ | Polarization factor of radiation |
| $\boldsymbol{q}$ | Scattering vector |
| $\boldsymbol{r}$ | 3-dimensional position vector |
| $R$ | Bravais lattice vector |
| TM | Transition metal |
| XRD | X-ray diffraction |

# Chapter 1

# Introduction

## 1.1   Motivations for Researching Li-Ni-Mn-Co Oxide Materials

Lithium (Li)-ion batteries are currently the most widely used rechargeable energy storage devices in the world and their high demand is expected to grow in the coming decades [1]. Li-ion battery technology is ideal for numerous energy storage applications due to the combination of high specific energy, a low amount of charge-loss during storage, and the lack of a memory effect from charging. Increasing energy demands for applications such as off-grid energy storage systems and electric vehicles (EVs) have forced the production of more energy dense Li-ion electrode materials that cycle longer and more efficiently [1, 2]. In particular, for EV applications, materials that combine a high energy density with a high charge and discharge rate capability are required to extend the range of EVs to eventually compete with their gas-fueled counterparts [2].

There are four key components to a Li-ion battery: the anode, cathode, electrolyte, and separator. The anode is the negative electrode and generally has an active material comprised of graphitized carbon which has a layered structure. The cathode is the positive electrode and generally has a lithium transition metal (TM) oxide active material with atoms arranged in either a layered or cubic spinel structure. The electrolyte is the medium which facilitates the transport of $Li^+$ from one electrode to the other within the cell and is typically composed of a Li-containing salt (commonly $LiPF_6$) dissolved in a carbonate-based solvent. The separator is a micro-porous membrane situated between the electrodes and it acts as an electrically insulating barrier that prevents short-circuiting of the electrodes. The micro-porous property of the separator allows for electrolyte to transport through the cell while the separator remains electrically insulating.

During charge, the lithium ions are driven from the structure of the cathode material to intercalate into the anode material. $Li^+$ has a higher chemical potential

**Table 1.1:** The specific capacity, median voltage, crystallographic density and calculated volumetric energy density of oxide materials existing within the system targeted by this thesis. $LiCoO_2$ is currently the most commonly used cathode material in commercial Li-ion cells. Many other materials in the table are also commercially available. The crystallographic densities for these materials were retrieved from the JCPDS database while the specific capacity and median voltages were found in [3], [4] and [5].

| Material | Specific Capacity (mAh/g) | Median Voltage (V) | Crystallographic Density (g/cm$^3$) | Volumetric Energy (Wh/cm$^3$) |
|---|---|---|---|---|
| $LiCoO_2$ | 155 | 3.88 | 5.05 | 3.04 |
| $LiCoO_2$ (coated with $ZrO_2$) | 175 | 4.05 | 5.05 | 3.58 |
| $LiMn_2O_4$ | 120 | 4.00 | 4.29 | 2.05 |
| $LiNiO_2$ | 200 | 3.55 | 4.78 | 3.39 |
| $Li[Ni_{0.9}Co_{0.1}]O_2$ | 220 | 3.76 | 4.79 | 3.96 |
| $Li[Ni_{0.7}Co_{0.3}]O_2$ | 190 | 3.70 | 4.86 | 3.42 |
| $Li[Li_{1/9}Ni_{1/3}Mn_{5/9}]O_2$ | 240 | 3.80 | 4.45 | 4.06 |

in the anode than anywhere else in the cell and thus electrochemical energy is stored when it is located there. During discharge, the process is reversed to have $Li^+$ extracted from the anode structure to intercalate back into the cathode, which is accompanied by electrons traveling through the external circuit to perform work.

The cathode accounts for roughly 1/3 the total cost of the cell [1, 6]. The cathode is therefore a crucial component to upgrade in order to improve the performance and lower the cost of Li-ion cells. The main improvements sought after in Li-ion electrode materials are increased volumetric energy density, lowered manufacturing cost, enhanced lifetime and better safety.

Table 1.1 shows the volumetric energy density of some example cathode materials existing within the Li-Co-Mn-Ni-O system, calculated from data contained in [3], [4], and [5]. Many commercially competitive cathode materials reside within the Li-Ni-Mn-Co-O system targeted by this thesis. In particular, lithium-rich layered materials such as $Li[Li_{1/9}Ni_{1/3}Mn_{5/9}]O_2$ are of interest due to their higher energy densities [4]. $LiCoO_2$ is currently the most commonly used commercial cathode material due to the combination of its reliable charge-discharge performance, high charge capacity and ease of manufacturing. Coating $LiCoO_2$ with

metal oxides, in particular $ZrO_2$, has been determined to greatly improve cycling performance and capacity [5], which allows $LiCoO_2$ to remain a competitive option despite the many developments in positive electrode materials research.

Lithium-rich layered materials exist over large composition ranges within the Li-Ni-Mn-Co-O system [4, 7]. Many lithium-rich materials existing in the Li-Ni-Mn-O system have been investigated in detail both structurally and electrochemically by McCalla for samples heated to 800°C in oxygen [8]. For EV applications where the objective is to maximize the energy stored within a limited volume, volumetric energy is the most important factor to distinguish the rank of competing electrode technologies. From the positive electrode materials listed in Table 1.1, it is evident that the Li-Ni-Mn-Co-O system is of interest for materials with high volumetric energy density. Due to the high cost of cobalt and its higher toxicity, it is desired to minimize the amount of Co included in cathode materials while simultaneously maximizing its electrochemical benefits. This suggests that investigating the low cobalt region of the Li-Ni-Mn-Co-O system has the potential to discover improved cathode materials.

Many results have been published regarding materials throughout the Li-Ni-Mn-Co-O system as potential cathode materials. These studies often investigate individual composition lines in regions of interest within the phase system and result in the discovery of interesting single-phase compositions such as the lithium-rich spinel $Li_{1+x}Mn_{2-x}O_4$ ($0 \leq x \leq 0.05$ at 800°C) [10, 11, 12]. The current project investigates the Li-Ni-Mn-Co-O system at cobalt contents of 10%, 20% and 30% of overall metal content, in addition to investigating the entire Li-Co-Mn-O system, using combinatorially made samples heated to 800°C and subsequently quenched or cooled slowly. The objective of the project is to map the phase diagram of the Li-Ni-Mn-Co-O system at low cobalt content, which has never been done prior to this work. A phase diagram of the Li-Ni-Mn-Co-O system was constructed for each of the two cooling rates used in the study. The combinatorial synthesis method used to accomplish this task was originally developed by Carey and Dahn [13] as a solutions-based approach to synthesize Li-Ni-Mn-O spinel materials and was further optimized by McCalla during his Ph.D work on the
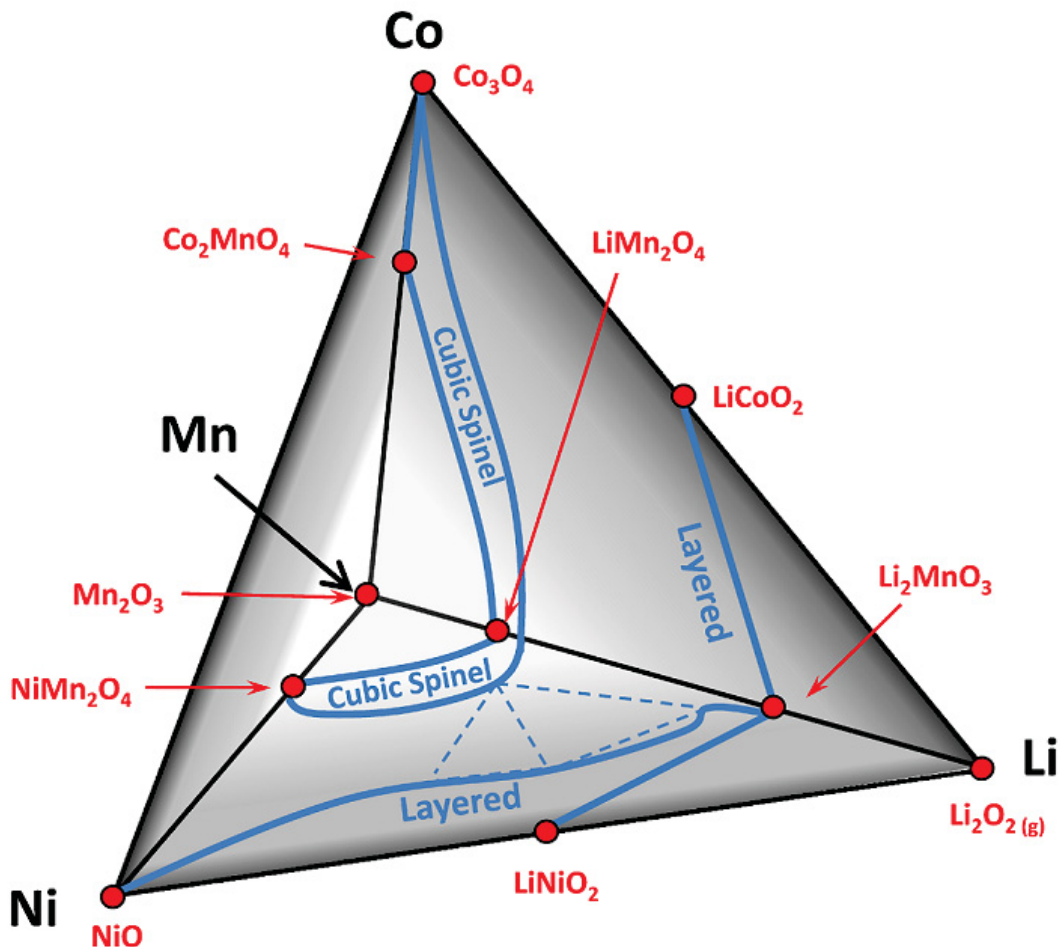
**Figure 1.1:** The Li-Ni-Mn-Co-O pseudo-quaternary system investigated by this thesis. The *black lines* indicate the binary axes. The gradients illustrate depth by further points being represented by a lighter background (*i.e.* the Mn corner is into the page). The *red dots* represent single-phase materials known prior to the current work. The *solid blue lines* indicate boundaries to single-phase regions of the Li-Co-Mn and Li-Mn-Ni faces as determined for samples quenched from 800°C. The *dashed blue lines* bound three-phase regions. The results for the Li-Ni-Mn face of this diagram were determined by McCalla [8, 9].

Li-Ni-Mn-O and Li-Co-Mn-O systems [8].

Every ternary system investigated in this thesis can be considered as a Gibbs triangle such that the oxide compositions are plotted by their metallic fractions only. The oxygen content of the samples are not controlled during synthesis so the samples reach equilibrium oxygen concentrations determined by the synthesis conditions [8]. Thus, the ternary and quaternary systems presented in this thesis

will be referred to as "pseudo-ternary" and "pseudo-quaternary" phase diagrams due to the oxygen content of their contained samples not being controlled. The presented pseudo-ternary and pseudo-quaternary phase diagrams therefore represent the phase stabilities that exist for the given synthesis conditions. Non-quenched samples only reach a metastable equilibrium since the oxygen content in samples cooled slowly is affected by diffusion kinetics during cooling [8, 12]. Prior to the current project and the work by McCalla [8], no surveys covering a wide range of compositions in the Li-Co-Mn-Ni-O system had been performed and there was a limited knowledge of the single-phase regions in this system. In particular, the coexistence regions throughout this system have not yet been fully understood, which poses difficulty for the study of composite electrodes [14, 15].

Figure 1.1 shows the Gibbs pyramid representing the Li-Ni-Mn-Co-O pseudo-quaternary system targeted by this thesis work. The phase structure of the Li-Co-Mn and Li-Ni-Mn faces of the pseudo-quaternary system are shown as determined for samples quenched from 800°C. The phase structures of the Li-Ni-Mn face shown in Figure 1.1 were determined by McCalla [8, 9]. The combinatorial methods used to synthesize and characterize the thousands of samples produced in this thesis work will be explained in detail in Chapter 2. The remainder of this introduction will discuss the relevant knowledge existing prior to the current project and will motivate the topics discussed in the following chapters.

## 1.2  Spinel and Layered Structures

Two large single-phase regions exist within the Li-Ni-Mn-Co-O pseudo-quaternary system as seen in Figure 1.1: the layered region and cubic spinel region. These regions contain numerous compositions of interest, some of which are included in Table 1.1. The layered materials can be viewed as ordered rocksalt structures constructed from the close-packed stacking of parallel sheets of atoms where each sheet is composed of a hexagonal arrangement of atoms. These layers are stacked in the pattern: lithium, oxygen, TM, oxygen, lithium ... The lithium atoms sit at octahedral sites surrounded by six nearest-neighbour oxygen atoms. Figures 1.2 (a)-(f) show the ideal atomic crystal structures of the layered, cubic spinel and tetragonal spinel phases that exist within the Li-Ni-Mn-Co-O system and Figures

1.2 (g)-(h) show 3-D models for the unit cell of hexagonal layered and cubic spinel structures with octahedral and tetrahedral sites indicated where applicable.

Some commonly used layered metal oxides in commercial batteries are $Li[Co]O_2$ and $Li[Ni_{1/3}Mn_{1/3}Co_{1/3}]O_2$, where the square brackets indicate the TM layer. This commonly used notation distinguishes the composition of the lithium and TM layers and is useful for indicating the lithium occupation of TM sites in lithium-rich materials such as $Li[Li_{1/9}Ni_{1/3}Mn_{5/9}]O_2$ [3]. Layered oxide materials in the Li-Ni-Mn-Co-O system typically have a one-to-one metal-to-oxygen ratio if there are no defects or oxygen vacancies present in the material [8, 9]. Furthermore, certain synthesis conditions can force the lithium and TM layers of a layered oxide material to mix slightly, resulting in a structural variant from the ideal shown in Figures 1.2 (a)-(b) [4].

The spinel structure is characterized by lithium atoms in tetrahedral sites and TM atoms in octahedral sites with oxygen placed at all nearest neighbour locations throughout the structure. The unit cell of the resulting arrangement of atoms is shown in Figures 1.2 (c)-(d) for cubic unit cell geometry. Lithium within the cubic spinel structure is intrinsically arranged into a 3-D network of tunnels, which allows for the extraction and reinsertion of lithium during charge-discharge cycling. Spinel materials can be arranged to have either a cubic or a tetragonal distorted unit cell [16, 17]. The tetragonal spinel structure common for $Mn_3O_4$ or $CoMn_2O_4$ is shown in Figures 1.2 (e)-(f) and is characterized by TM atoms in both the tetragonal and octahedral sites. In contrast with the cubic spinel structure, the tetragonal spinel structure has very little to no lithium content. These materials exist in the Li-Co-Mn-Ni-O system at high Mn content and can be detected as a contaminant in cubic spinel materials. The lack of lithium in tetragonal spinel materials mean they are of little interest in the context of Li-ion battery research.

## 1.3 Li-Co-Mn-O Pseudo-Ternary System

Figure 1.3 shows the single-phase compositions known to exist in the Li-Co-Mn-O system prior to the current work. The ternary diagrams in this thesis are constructed such that the position of a sample on a diagram is defined only by its
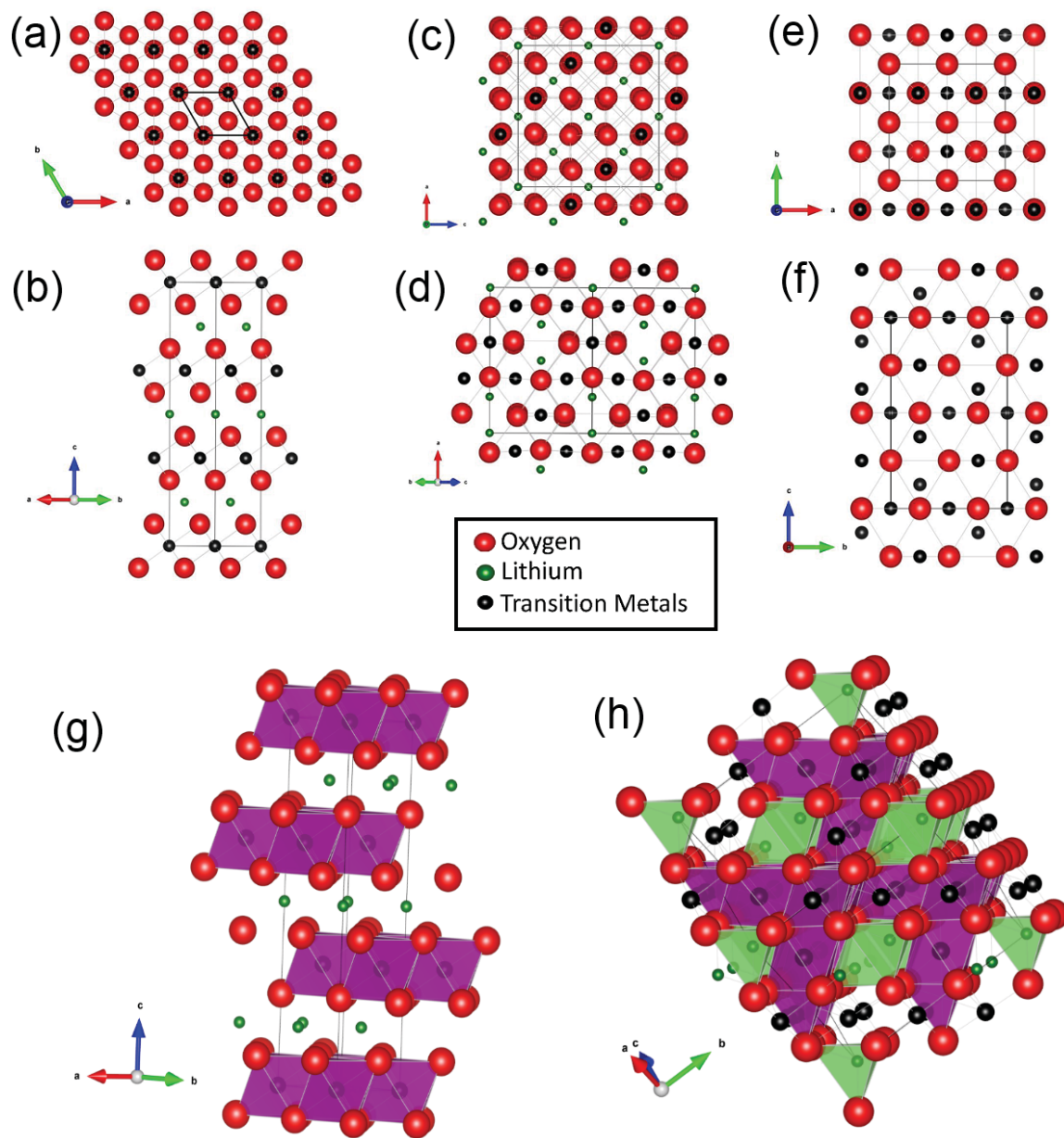
**Figure 1.2:** Structure of a layered lithium TM oxide material along the (a) 001 projection and (b) 110 projection. Structure of a cubic spinel along the (c) 010 projection and (d) 011 projection. Structure of a tetragonal spinel along the (e) 001 projection and (f) 010 projection. The polyhedra structure of (g) octahedral sites in hexagonal layered materials are drawn in purple and (h) octahedral and tetrahedral sites in cubic spinel materials are drawn in purple and green respectively. The darker lines within each structure outline one unit cell and the lighter lines represent bonds. The species of the atoms are indicated in the center of the figure.

metallic fractions. As is true for the pseudo-quaternary diagrams, the oxygen contents of materials existing in the ternary are free to vary throughout the system. Thus, only the metal atoms obey the rules of a Gibbs triangle and the three axes of Figure 1.3 are therefore the metal atom fractions with $Li + Co + Mn = 1$ for all points within the ternary diagram. Furthermore, since the lithium content can be calculated as $1 - Co - Mn$, all points in this system will be referred to as [Co, Mn], such that [0.5, 0] refers to $LiCoO_2$, [0, 0.333] refers to $Li_2MnO_3$ and so on. The composition labels at the corners of the ternary diagram indicate the phases present at those locations for the specified synthesis conditions.

Due to the oxygen content varying throughout the phase system, these Gibbs triangles represent a non-planar surface in the Li-Co-Mn-O quaternary system. As a result, the oxygen content at any given position within the triangle is a function of not only the sample metal content, but also the synthesis conditions. Both the heating atmosphere and temperature profile used during heating highly influence the resulting oxygen content of a material [8, 12].

The layered solid solution line connecting $LiCoO_2$ to $Li_2MnO_3$ in the Li-Co-Mn-O pseudo-ternary system for samples heated to 800°C was determined by McCalla for multiple cooling rates [8, 18]. Along this solid solution line, cobalt is constrained to the +3 oxidation state and is ideally located at the octahedral sites of the TM layers. A significant result of the work by McCalla in this system was the discovery of a phase separation on the layered solid solution line resulting from slower cooling rates used after heating. McCalla found a maximum phase separation for the solid solution existing from $x = 0.2$ to $0.8$ in $Li[Li_{(1-x)/3}Co_xMn_{(2-2x)/3}]O_2$ for samples slow-cooled at a rate of 1°C/min from 900°C [18]. The same composition range existed as a homogeneous single-phase solid solution for samples quenched from 900°C. For intermediate cooling rates, McCalla determined that nanodomains of both layered phases in the 2-10 nm length scale were formed on the same lattice due to the lack of time for the system to produce the large scale crystallites observed at the lowest cooling rate studied [8, 18]. Tie-lines connecting the layered and cubic spinel regions investigated in this study within the Li-Co-Mn-O pseudo-ternary system were determined from a combination of the layered solid solution work by McCalla and the single-phase cubic spinel work presented in
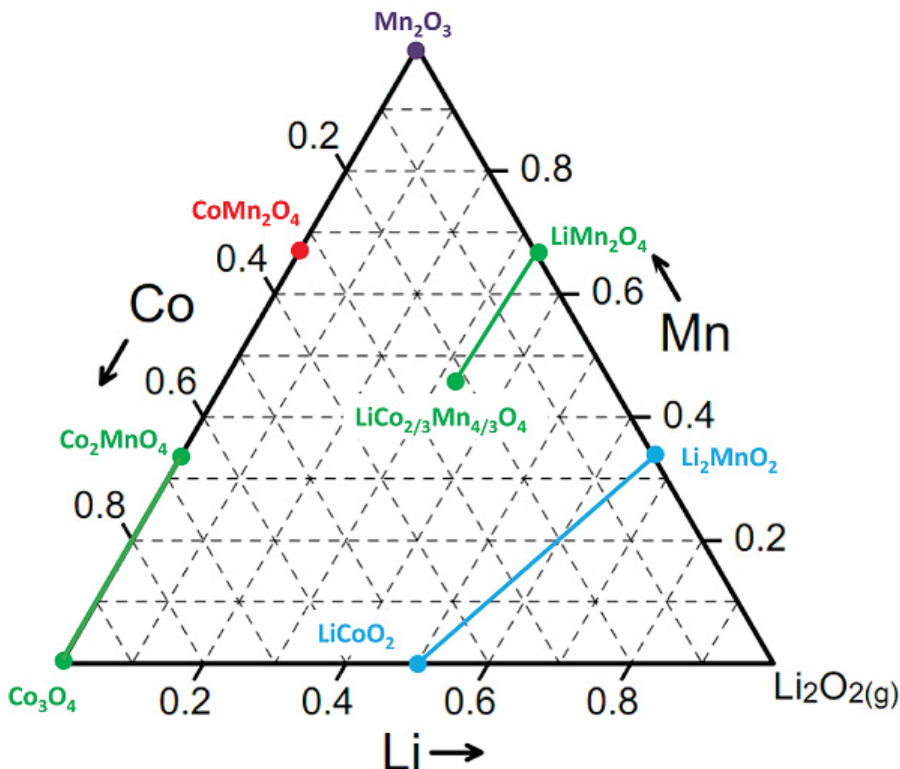
**Figure 1.3:** The Li-Co-Mn-O pseudo-ternary system with single-phase materials known prior to the current combinatorial studies for samples quenched from $800°C$ in air. The compositions marked in *green* indicate cubic spinel, *light blue* indicates layered, *red* indicates tetragonal phase and *purple* indicates bixbyite $Mn_2O_3$. The lithium corner is labeled as $Li_2O_{2(g)}$ which is a gaseous compound formed by the oxidation of excess lithium during heating and is the primary reason for lithium loss in the combinatorial samples of this work [8].

Chapter 3 of this thesis. The method used to calculate tie-lines through the layered-spinel coexistence region and their direction will be discussed in Chapter 2.

A recent paper by Long et al. [19] reported that regardless of the cooling rate used during synthesis, there was no change in the local structure of materials existing throughout the layered solid solution line extending from $LiCoO_2$ to $Li_2MnO_3$. The study by Long et al. included high resolution synchrotron x-ray diffraction measurements and x-ray absorption near-edge spectroscopy (XANES) spectra analysis for several samples prepared at a targeted composition of $Li_{1.2}Mn_{0.4}Co_{0.4}O_2$. The results of their research seemingly contradict the results of the combinatorial studies performed by McCalla [8, 18]. However, all but two of the samples in the work by Long et al. underwent an initial $550°C$ annealing step that caused the x-ray diffraction peaks of the material to have more pronounced

high-angle broadening and peak shoulders when compared to samples that were not subject to the annealing step. Long et al. prepared one slow-cooled (1°C/min) and one rapidly quenched (30°C/sec) sample at 850°C without the 550°C annealing step and claim that they have matching XRD spectra [19]. Elemental analysis results were not published by Long et al. for these two samples, but the elemental analysis results of samples with the 550°C intermediate step showed good agreement with the targeted composition. Transmission electron microscopy results presented by Long et al. for a pair of samples that underwent a 550°C annealing step and subsequently rapidly quenched or slow-cooled from 850°C suggest that some disorder was present in the slow-cooled sample and not present in the rapidly quenched sample [19]. Ultimately, the 550°C annealing step adds further complication to samples of the Li-Co-Mn-O system and likely explains the conflicting results between their work and the work by McCalla. Furthermore, there is not enough data in the work by Long et al. for samples of similar synthesis conditions to those of McCalla to conclude that it is impossible for the layered solid solution line extending from $LiCoO_2$ to $Li_2MnO_3$ to phase separate due to lower cooling rates.

Prior to the current work on the spinel region of the Li-Co-Mn-O system, only a few spinel structures were known to exist in the system [20, 21, 22, 23], which are shown in green in Figure 1.3. In addition to these spinel structures, two solid solution lines of spinel structures have also been determined. Amarilla et al. observed the $LiCo_xMn_{2-x}O_4$ ($0 \leq x \leq 0.66$) spinel solid solution (green line in Figure 1.3), which was determined for samples regular-cooled from 600°C [20]. Guohua et al. also observed the $LiCo_xMn_{2-x}O_4$ ($0 \leq x \leq 0.33$) spinel solid solution for samples synthesized at 750°C with regular-cooling [21].

Aukrust and Muan observed the quenched Co-Mn binary for temperatures in the range of 900°C to 1500°C and determined the range of the cubic spinel region existing within it [23]. Aukrust and Muan inferred the behaviour of the binary for temperatures below 900°C by extrapolating the results from a few samples of high Mn content. At 800°C their binary phase diagram predicts a cubic spinel solid solution ranging from $x = 1.11$ to 3 for $Co_xMn_{3-x}O_4$ [23]. This predicted region by Aukrust and Muan is much larger than that determined in this work. This

discrepancy is likely the result of statistical error from extrapolating boundary lines from only a few samples synthesized at higher temperatures and higher Mn content. In Figure 1.3, the solid solution line from $Co_3O_4$ to $Co_2MnO_4$ was drawn as it matches the results found in the current work on the quenched Li-Co-Mn-O pseudo-system for samples heated to 800°C in air [24].

Although the amount of spinel structures in the Li-Co-Mn-O system published in the literature prior to this work is relatively sparse, the fact that the cobalt corner forms the spinel structure $Co_3O_4$ suggests the existence of a spinel solid solution spanning from $Co_3O_4$ to $LiMn_2O_4$. Similarly, the existence of the spinel composition $Co_2MnO_4$ suggests a spinel solid solution spanning from $Co_2MnO_4$ to $LiMn_2O_4$. The combination of these two solid solutions with the solid solution from $Co_3O_4$ to $Co_2MnO_4$ would define a large single-phase cubic spinel region within the Li-Co-Mn-O system. Chapter 3 of this thesis investigates the single-phase cubic spinel region of the Li-Co-Mn-O pseudo-ternary system and determines the effect of cooling rate on the position and shape of the region.

## 1.4  Li-Ni-Mn-O Pseudo-Ternary System

The current thesis work seeks to understand the structure of the Li-Ni-Mn-Co-O pseudo-quaternary phase diagram (shown in Figure 1.1) at low cobalt contents. In order to interpret the results of this work, an understanding of the Li-Ni-Mn-O system must be established beforehand. The results of the Li-Ni-Mn-O system by McCalla [8, 9] will be used as the groundwork for this study and will help isolate the effects of cobalt within the Li-Ni-Mn-Co-O system by comparing the Li-Ni-Mn-O phase diagram with the phase diagrams determined in this study at 10%, 20% and 30% cobalt fractional metal content.

Figure 1.4 shows the Li-Ni-Mn-O pseudo-ternary phase diagrams determined in their entirety by McCalla for samples either quenched or regular-cooled from 800°C in $O_2$ [8, 9]. As is true in the Li-Co-Mn-O system, the most important structures in the Li-Ni-Mn-O system for Li-ion cathode material applications are either cubic spinel or hexagonal layered. The locations of these regions are labeled in Figure 1.4. Coordinates of the Gibbs triangles are determined from only the fractional metal content of a composition and are represented as: (Ni, Mn). The lithium content can
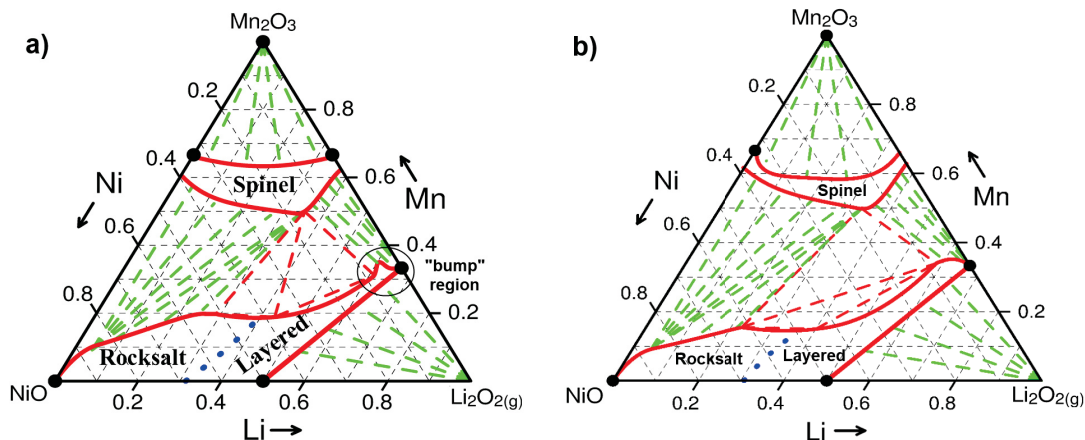
**Figure 1.4:** Complete pseudo-ternary diagrams for the Li-Ni-Mn-O ternary system determined combinatorially. Samples were heated to 800°C for 3 h in an $O_2$ atmosphere and (a) quenched or (b) slow-cooled to room temperature. The spinel and rocksalt-layered single-phase regions are bounded by the *solid red lines* as shown. The *blue dotted line* defines the phase transition between rocksalt and layered. Green lines are tie-lines of constant lattice parameters. (Reprinted from [9] with permission from the American Chemical Society)

be calculated as 1 - Ni - Mn. The combinatorial methods used to determine the phase diagrams shown in Figure 1.4 are the same as those used in the current work, which were developed by Carey and Dahn [13] and further optimized by McCalla [8].

Carey and Dahn [13] used a combinatorial solutions-processing robot to successfully synthesize spinel samples in the $LiNi_xMn_{2-x}O_4$ composition region through carbonate coprecipitation of nickel, manganese, and lithium nitrate microliter solutions. The precipitated samples were heated to 800°C in air to form the desired spinel oxide structures. The scope of the project was expanded by McCalla to investigate the entire Li-Ni-Mn-O pseudo-ternary system using the same combinatorial synthesis methods. However, McCalla discovered a significant challenge while investigating regions of higher lithium content: these regions tended to show extreme lithium loss during heating such that certain compositions could not be synthesized in air even at temperatures as low as 700°C [8, 25]. McCalla determined that this effect was the result of $Li_2O_2$ being formed during the synthesis of compounds in which lithium had low binding energies and one of the largest lithium losses was observed in $LiNiO_2$ [8, 25]. In $LiNiO_2$, lithium has a low binding energy within the layered structure. Lithium is therefore more likely to be removed from $LiNiO_2$ during heating by oxidizing to form lithium peroxide, resulting in lithium loss from the structure. Measurements of gram-scale $LiNiO_2$

samples synthesized by solid-state reactions and heated in air have shown lithium losses on the order $5\%$ [26, 27]. Microgram-scale combinatorial samples (such as the materials made for this work) result in far larger amounts of lithium loss compared to bulk samples due to the larger surface-area-to-volume ratio of combinatorial samples during heating. Spinel samples of the $LiNi_xMn_{2-x}O_4$ composition line produced combinatorially showed negligible lithium loss [13] due to the higher binding energy of lithium within the spinel structure. To effectively study the entire Li-Ni-Mn-O pseudo-ternary system, McCalla realized that the effects of lithium loss had to be minimized. This task was accomplished successfully [8, 25] and will be discussed further in Chapter 2.

### 1.4.1   Li-Ni-Mn-O Rocksalt and Layered Single-Phase Regions

The dotted blue lines dividing the layered regions of both phase diagrams in Figure 1.4 indicate the transition between a cubic rocksalt and a hexagonal layered structure. The rocksalt materials are of a disordered cubic type, where metal atoms occupy a face-centered cubic lattice and each metal site is randomly occupied by Li, Ni or Mn. The line from $x = 0$ to 1 for $Li_xNi_{2-x}O_2$ (from Ni corner of Figure 1.4 to $LiNiO_2$) has been studied previously and was found to have a disordered rocksalt structure for $x < 0.62$ [28]. These rocksalt materials often appear as contaminants when synthesizing either spinel or layered-spinel composite materials, which motivates research seeking to minimize their presence. Above $x = 0.62$, the structures are layered hexagonal as illustrated in Figures 1.2 (a)-(b) [28]. McCalla determined the location of the transition lines by fitting the XRD patterns of both structures as hexagonal and plotting the $c/a$ lattice parameter ratio versus $x$ [8]. The results were extrapolated to the point where the $c/a$ ratio reaches $\sqrt{24}$, which is the expected value for a cubic structure [28], giving the position of the rocksalt-layered phase transition boundary.

The circled "bump region" within the layered single-phase region of Figure 1.4 (a) contains single-phase layered structures that have a significant amount of metal site vacancies within their crystal structures [8, 29]. McCalla determined that the maximum vacancy content found in the material $Li[Ni_{1/6}\square_{1/6}Mn_{2/3}]O_2$ resulted in

highly ordered monoclinic structures whereby manganese occupies 2/3 of the $\sqrt{3}\times\sqrt{3}$ superlattices on the transition metal layer and the remaining 1/3 superlattices were occupied by nickel, lithium, and vacancies [8]. These metal site vacancy compounds showed electrochemical behavior similar to that of lithium-rich materials, but are themselves not actually lithium-rich as lithium occupies only 50 % of total metal sites [8]. Furthermore, McCalla observed a roughly 1 % vacancy content in lithium-rich materials existing along the layered solid solution extending from $Li_2MnO_3$ to $LiNi_{0.5}Mn_{0.5}O_2$ which, as suggested by Monte Carlo simulations, allows for $Ni^{3+}$ to substitute for $Mn^{4+}$ on 2/3 of the monoclinic superlattices [8, 9].

### 1.4.2  Li-Ni-Mn-O Cubic Spinel Single-Phase Region

Prior to the work by McCalla summarized in Figure 1.4, studies regarding spinel materials in the Li-Ni-Mn-O system were mainly focused on the solid solution of $LiNi_xMn_{2-x}O_4$ for $x = 0$ to 0.5 [10, 28, 30, 31]. There was little focus in the literature on mapping the single-phase regions within the Li-Ni-Mn-O system and confusion arose in this composition as a result. In particular, the endpoint spinel composition of $LiNi_{0.5}Mn_{1.5}O_4$ was observed to be a single-phase when heated in oxygen, but found to be multiphase due to a contaminant rocksalt phase when heated in air [31, 32]. This issue was resolved by McCalla who compared the phase diagrams prepared in oxygen as shown in Figure 1.4 with similar diagrams prepared in air [8]. It was found that for samples prepared in air, the spinel boundary shifts such that $LiNi_{0.5}Mn_{1.5}O_4$ is located in the rocksalt-spinel coexistence region and a tie-line connects the composition to a rocksalt phase near the Ni corner [8].

The position of boundaries to the single-phase spinel region can also shift due to the cooling rate, as can be seen by comparing the phase diagrams of Figures 1.4 a and b. The mechanism for the shift due to cooling rate is the presence of oxygen vacancies that can be sustained in spinel materials throughout the Li-Ni-Mn-Co-O system at high temperatures and are subsequently refilled with oxygen during slow cooling [33, 34, 35]. In particular for the spinel composition $LiNi_{0.5}Mn_{1.5}$ discussed above, for temperatures at or above 750°C, compositions of $LiNi_{0.5}Mn_{1.5}O_{4-\delta}$ with $\delta = 0.1$ are able to be synthesized [36]. The result of the oxygen loss of spinel materials during heating can have a dramatic effect on the resulting phase diagram, as will be

demonstrated in Chapter 3 for the spinel region of the Li-Co-Mn-O system and in Chapter 4 for the spinel region throughout the low cobalt region of the Li-Ni-Mn-Co-O system.

### 1.4.3   Li-Ni-Mn-O Layered-Spinel Coexistence Region

Figure 1.5 (a) shows XRD pattern stacks of the four corner compositions found to define two separate three-phase regions within the Li-Ni-Mn-O pseudo-ternary system for samples both quenched (*left stack*) and regular-cooled (*right stack*) as determined by McCalla [8, 9]. The spinel phase marked by 'S' in Figure 1.5 (b) is approximately the composition $LiNi_{0.5}Mn_{1.5}O_4$ and ties to two distinct layered compositions marked by 'M' and 'N' and also to an ordered rocksalt phase marked by 'R'. Samples prepared within the three-phase regions defined by these corner compositions were found to have XRD patterns able to be fit by a linear combination of the corner phases [8, 9]. It is important to note how sensitive the preparation of the spinel sample 'S' has to be in order to ensure no contaminant phase is formed. Any excess nickel would result in a contaminant rocksalt phase and excess lithium would result in a multiphase layered-spinel material.

With regards to the phase diagrams constructed in this thesis for the 10 %, 20 %, and 30 % cobalt metal contents of the Li-Ni-Mn-Co-O system, a similar coexistence region was found to exist, which connected the spinel and layered regions. However, the tie-lines were too difficult to accurately determine in those phase diagrams without carefully surveying the entire Li-Ni-Mn-Co-O pseudo-quaternary system. This is due to the fact that the mathematical method used to calculate the tie-lines shown in Figures 1.4 (a)-(b) for pseudo-ternary systems increases in difficulty by an extra dimension while working inside the Li-Ni-Mn-Co Gibbs pyramid (*i.e.* tie-lines exist in 3-D space inside the Gibbs pyramid instead of only in 2-D space within the ternary systems defining the faces of the Gibbs pyramid). As a result, the coexistence regions of the 10 %, 20 %, and 30 % cobalt metal content phase diagrams were difficult to carefully analyze and explicitly define in a manner similar to those shown in Figure 1.5 (b) for the Li-Ni-Mn-O system. Instead, the boundaries to single-phase regions and the phase content of multiphase regions in these systems were determined from the inspection

**Figure 1.5:** (a) XRD pattern stacks of the four samples found at the corners of the three-phase regions of the the Li-Ni-Mn-O pseudo-ternary phase diagram obtained by quenching (*left stack*) and regular-cooling (*right stack*). The coordinates shown above each scan are (Li, Mn) where Li is the lithium metal fraction and Mn is the manganese metal fraction. (b) The portion of the Li-Ni-Mn-O pseudo-ternary phase diagram relevant to the XRD patterns shown in (a). (Reprinted from [9] with permission from the American Chemical Society)
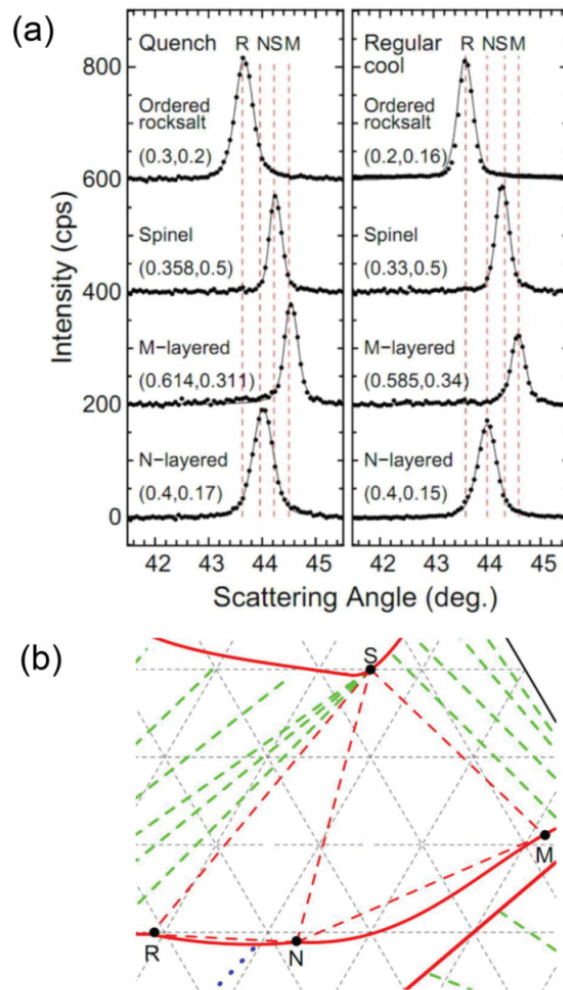
of XRD fitting results for each individual sample throughout the phase diagrams.

## 1.5  Li-Ni-Mn-Co-O Pseudo-Quaternary System

The Li-Ni-Mn-Co-O system (illustrated in Figure 1.1) contains all phase diagrams and compositions discussed in this introduction and the objective of this thesis is to better understand the system by mapping a significant portion of its phase diagram. As discussed previously, much work has been done on compositions existing on the faces of the Li-Ni-Mn-Co-O Gibbs pyramid, but not a substantial amount has been done on compositions existing within that contain all four metals.  Such compositions are typically referred to as 'NMC' materials and the most popular of

which in the literature is the layered compound $LiNi_{1/3}Mn_{1/3}Co_{1/3}O_2$ [37, 38]. The proposed benefits of layered NMC materials compared to the commonly used $LiCoO_2$ are lower cost, lower toxicity, better thermal stability when charged, higher reversible capacity, and better stability when cycling at elevated temperatures [38]. Although the phase regions of NMC materials have not yet been fully understood, there is interest in various single-phase layered NMC compounds [38, 39, 40] as well as spinel-layered core-shell materials with low cobalt content [6, 41]. Therefore, it would be ideal to map the phase diagrams that contain these compounds of interest in order to further understand them and potentially discover better materials.

## 1.6   Content of this Thesis

Chapter 2 will introduce the theory and experimental techniques used throughout this thesis in addition to the techniques that have been developed specifically for this project.   Chapter 3 details the results from the combinatorial study investigating the single-phase cubic spinel region of the Li-Co-Mn-O pseudo-ternary phase system for two distinct sample cooling rates. Chapter 4 presents the results from the combinatorial study investigating the phase diagrams at $10\%$, $20\%$, and $30\%$ cobalt metal contents in the Li-Ni-Mn-Co-O pseudo-quaternary phase system for two different sample cooling rates. Chapter 5 summarizes the work presented in the thesis with concluding remarks and addresses the future work required to expand on the found results. Finally, the results of the XRD fitting for every unique single-phase composition observed in this thesis are listed in Appendix A for reference.

# Chapter 2

# Experiment and Theory

## 2.1  Synthesis of Combinatorial Samples

Combinatorial arrays of milligram-scale samples belonging to the Li-Ni-Mn-Co-O pseudo-quaternary system were produced in this thesis work. Details of the employed high-throughput synthesis method and the previous work that lead to its development will be discussed here. The combinatorial method was originally developed by Carey and Dahn [13] and further optimized by Eric McCalla during his Ph.D work [8].

For the $LiNi_xMn_{2-x}O_4$ system, Carey [13] prepared solutions of approximately 2 M lithium nitrate (Aldrich, 97 %), manganese (II) nitrate tetrahydrate (Fluka, 97 %), and nickel (II) nitrate hexahydrate (Fluka, 97 %). Carey dispensed a combined volume of 10 $\mu$L of these solutions for each sample using the Cartesian Pixsys solution-processing robot partially shown in Figure 2.1 (a). Alumina plates (Pi-Kem, 96 %) coated with stearic acid (Aldrich, 96 %) were used as the substrate for dispensed samples. The stearic acid served as a beading agent for the solutions, which prevented runoff and mixing. Carey then added ammonium bicarbonate (Alfa Aesar, 98 %) in excess to induce co-precipitation of Li, Mn and Ni carbonates. The samples were dried overnight at 55°C and then heated to 800°C in air and held for 3 hours to form the desired oxides.

Silicon (100) wafers were then coated by an adhesive mixture of Trilene-65 (a polymer mixture produced by Lion Copolymer) and cyclohexane. The coated wafer was then inverted over the alumina plate and pressed to transfer the oxide samples onto the adhesive surface of the silicon wafer for x-ray diffraction (XRD) analysis. Carey demonstrated by XRD that the combinatorial samples produced in this manner resulted in the expected spinel oxides for the targeted compositional region [13].

McCalla optimized the combinatorial synthesis process developed by Carey by

18
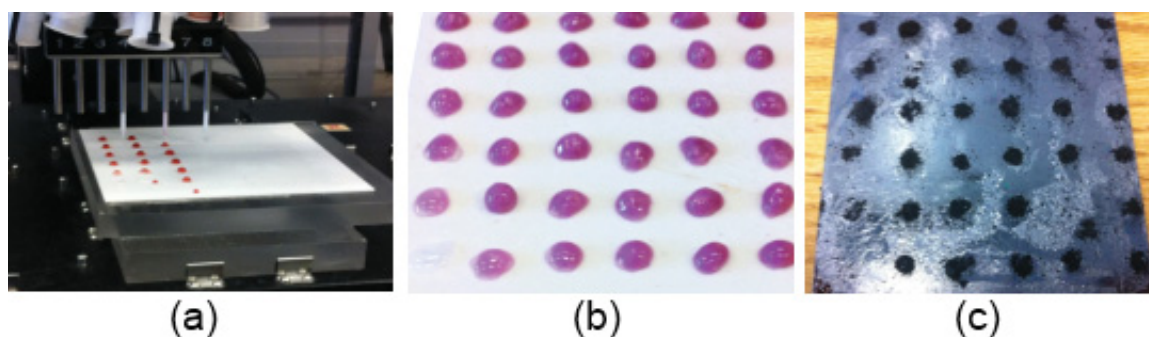
**Figure 2.1:** The major stages of processing for a standard $6 \times 6$ composition array used in this thesis. All the samples in this figure are simply an equal mixture of Li and Co for demonstrative purposes only. The bottom left sample was left blank to mark orientation. (a) The Pixsys solutions-processing robot during a dispensing routine. (b) Freshly dispensed samples after adding 25 $\mu$L of ammonium bicarbonate to each to induce co-precipitation. (c) Resulting oxide materials transferred onto silicon (100) wafer after heating to 800°C. The textured material seen on the silicon wafer between the black powder oxide samples is dried Trilene-65 and cyclohexane mixture.

minimizing lithium loss during heating [8]. The variables controlled by McCalla in his optimization were the choice of substrate (alumina, alumina coated with $LiAlO_2$, and magnesia), the precipitator used (ammonium bicarbonate or ammonium hydroxide), the volume of solution dispensed per sample (10 or 20 $\mu$L), the heating temperature (200, 300 ... 1000°C) and atmosphere while heating (air or $O_2$). For the conditions tested, McCalla found that lithium loss was minimized by using an alumina substrate coated with stearic acid, an ammonium bicarbonate precipitator, a dispensed solution volume of 20 $\mu$L, and heating at 800°C in an $O_2$ atmosphere. This optimized combination was utilized throughout this thesis work except for the Li-Co-Mn-O system, which was heated in air instead of $O_2$.

Figure 2.1 (a)-(c) shows an example combinatorial array at different stages of production by the methods used in this thesis. The Pixsys solutions-processing robot seen in Figure 2.1 (a) uses ceramic composite dispensing tips that have precision to a tenth of a microliter, allowing for highly accurate dispensing during sample production. The combinatorial synthesis procedure used here proceeds directly as follows. Each combinatorial sample, with a mass of approximately 2 mg, was made by dispensing 20 $\mu$L total of 1.90 M solutions with the solutions-processing robot. Prior to dispensing, the solution concentrations were

**Figure 2.2:** The Li-Co-Mn oxide triangle illustrating how samples were synthesized to map out an entire composition range within a Gibbs triangle. The triangular region highlighted in blue contains the repeated samples for the initial survey sample series. Samples were initially produced at every intersection of dashed lines and then over smaller regions of interest.
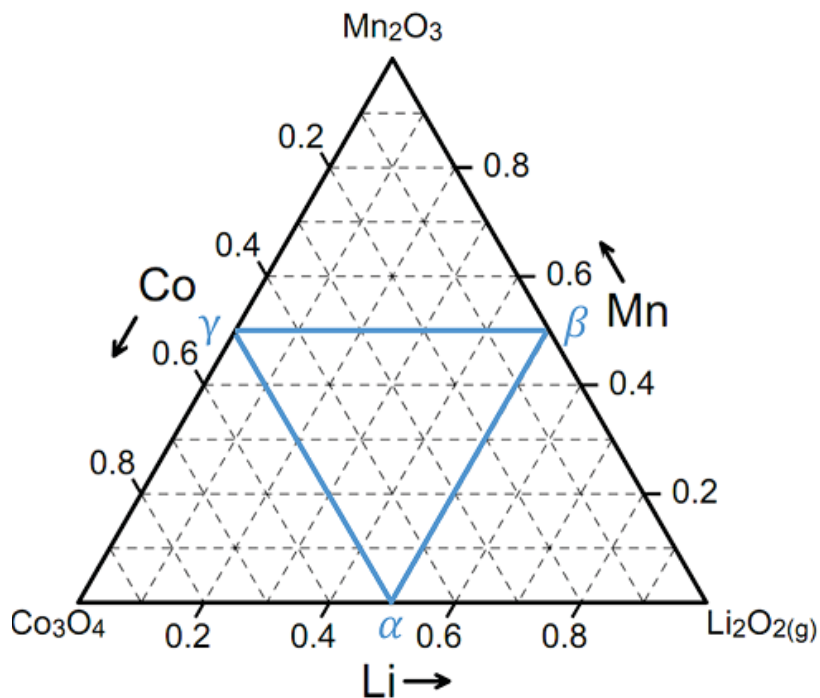


measured to an accuracy of 2 % using atomic absorption methods as described later in this chapter.

For investigating the Li-Ni-Mn-Co-O system, pseudo-ternary oxide samples were synthesized at three discrete cobalt content levels of 10 %, 20 %, and 30 % of overall metal content, resulting in a ternary diagram stack along the cobalt axis. In Chapter 4, this series of ternary diagrams will be referred to as 'cobalt-slices' since each ternary diagram essentially 'slices' the Gibbs pyramid at distinct levels of cobalt content. The samples in the Li-Ni-Mn-Co-O system were produced from three solutions of nickel, manganese, and lithium nitrates, with an amount of cobalt included equally to each in order to achieve the desired cobalt content. A 25 $\mu$L amount of 2 M ammonium bicarbonate solution was added to directly to each sample after dispensing to induce co-precipitation of metal carbonates, which were then dried overnight at 55°C. After drying, the samples were heated in a tube furnace at 800°C for 3 h under an $O_2$ flow of approximately 30 mL/min. Two cooling rates were used. The first involved quenching samples by carefully removing the alumina substrates from the furnace at 800°C and placing them directly on a

flat iron slab at room temperature. The iron slab acted as a heat sink for the heat stored in the substrate and resulted in an average cooling rate on the order of 10°C/sec as determined by infrared temperature sensor measurements [8]. The second cooling rate involved turning off power to the furnace to let samples cool from ambient heat loss and will be referred to as regular-cooling. This cooling method is similar to the process commercial electrode manufacturers prefer to use for large scale production, as quenching bulk materials is far more difficult in comparison. The cooling rate for this method decreases with temperature from a maximum rate of approximately 10°C/min to a rate of approximately 5°C/min at 100°C. When cooled to room temperature, the samples were transferred onto silicon (100) wafers coated with a mixture of Trilene-65 and cyclohexane. The silicon wafer was then mounted onto the translational stage of the Bruker D8 Diffractometer and XRD patterns were measured for each sample. The 20 % and 30 % cobalt levels were synthesized and scanned with XRD by Cody Watson as his summer research project in 2013.

Figure 2.2 illustrates the methodology used to synthesize samples evenly throughout the Gibbs triangles investigated in this thesis. The included ternary grid is that of the Li-Co-Mn-O pseudo-ternary system, which was the first system investigated in this work and will be discussed in Chapter 3. For every new ternary system, samples were made for stoichiometries at every intersecting point of the dashed lines, resulting in 66 unique compositions within the ternary. This was accomplished by producing $6 \times 6$ sample arrays on three separate alumina plates. Each plate was sliced in half to fit within the tube furnace and both halves were heated simultaneously. The three $6 \times 6$ arrays correspond to equidistant samples within the three following parallelograms: $Co_3O_4 \, \alpha \, \beta \, \gamma$, $Li_2O_2 \, \beta \, \gamma \, \alpha$, and $Mn_2O_3 \, \gamma \, \alpha \, \beta$. This sampling method results in 21 repeated compositions on each of the three plates, which serve as reproducibility checks for the synthesis process. A total of 108 samples were made for every 66 unique compositions and this sampling method is the first step in mapping each ternary system of this work. Following this initial series, arrays were produced over more constrained regions in an effort to 'zoom in' on compositions of interest and also increase sampling resolution in those

areas. Regardless of the sampling routine used, each compositional array in this thesis had duplicates produced to ensure reproducibility.

## 2.2 X-Ray Diffraction

### 2.2.1 Crystallography and Miller Indices

The fundamental building block of a crystalline solid is the unit cell. The unit cell is a structural grouping of atoms in 3-dimensions and represents the smallest repeating unit of the entire crystal structure. For a Bravais lattice, the atomic positioning within the lattice is described by the Bravais lattice vector,

$$\boldsymbol{R} = n_1\boldsymbol{a}_1 + n_2\boldsymbol{a}_2 + n_3\boldsymbol{a}_3 \tag{2.1}$$

where the values of the integer coefficients $n_1$, $n_2$, and $n_3$ are determined by the arrangement of lattice points, and the vectors $\boldsymbol{a}_1$, $\boldsymbol{a}_2$, and $\boldsymbol{a}_3$ are the primitive vectors of the lattice. Furthermore, there exists a reciprocal lattice vector $\boldsymbol{G}$ such that,

$$\boldsymbol{G} = h\boldsymbol{b}_1 + k\boldsymbol{b}_2 + l\boldsymbol{b}_3 \tag{2.2}$$

where $\boldsymbol{b}_1$, $\boldsymbol{b}_2$, and $\boldsymbol{b}_3$ are the primitive vectors of the reciprocal lattice that follow the general constraint:

$$\boldsymbol{b}_i \cdot \boldsymbol{a}_j = 2\pi\delta_{ij} \tag{2.3}$$

In three dimensional space, every reciprocal lattice vector $\boldsymbol{b}$ will have two orthogonal normal lattice vectors, $\boldsymbol{a}$. The reciprocal lattice vectors are defined as follows:

$$\boldsymbol{b}_1 = 2\pi\frac{\boldsymbol{a}_2 \times \boldsymbol{a}_3}{\boldsymbol{a}_1 \cdot (\boldsymbol{a}_2 \times \boldsymbol{a}_3)}; \quad \boldsymbol{b}_2 = 2\pi\frac{\boldsymbol{a}_3 \times \boldsymbol{a}_1}{\boldsymbol{a}_1 \cdot (\boldsymbol{a}_2 \times \boldsymbol{a}_3)}; \quad \boldsymbol{b}_3 = 2\pi\frac{\boldsymbol{a}_1 \times \boldsymbol{a}_2}{\boldsymbol{a}_1 \cdot (\boldsymbol{a}_2 \times \boldsymbol{a}_3)} \tag{2.4}$$

The coefficients $h$, $k$, and $l$ in Eq. (2.2) are integer values representing the Miller indices of the lattice that define unique lattice planes. These lattice planes correspond to an individual x-ray diffraction peak and can be referenced using the notation $(hkl)$. Every plane defined by $(hkl)$ has a corresponding reciprocal lattice vector $\boldsymbol{G}(h, k, l)$ that is perpendicular to the lattice plane.

## 2.2.2 Bragg's Law

Bragg's Law describes the angles of incidence required for radiation of a specific wavelength to scatter coherently from a crystal lattice. The mechanism for this effect is the constructive interference of waves scattering from identical $(hkl)$ planes within the lattice. Figure 2.3 (a) illustrates the geometry of a plane wave scattering from two atoms of an arbitrary material. In order for the reflected waves to be coherent (*i.e.* diffraction to occur) they must be in phase after scattering. This gives the condition that the phase difference, $\phi$, must be equal to an integer multiple of $2\pi$. By inspection of Figure 2.3 (a), this phase difference can be represented as:

$$\phi = k_i d \cos\theta - k_f d \cos\theta' \tag{2.5}$$

which can be rewritten as a difference of dot products:

$$\phi = \boldsymbol{k}_i \cdot \boldsymbol{d} - \boldsymbol{k}_f \cdot \boldsymbol{d} \tag{2.6}$$

To determine the explicit conditions for diffraction to occur, the reflected plane waves must be superimposed as follows:

$$\Psi(\boldsymbol{r}, t) = \psi_f(\boldsymbol{r}, t) + \psi_f(\boldsymbol{r}, t)e^{i\phi} \tag{2.7}$$

where $\Psi(\boldsymbol{r}, t)$ is the wave function representing the superposition of the two reflected plane waves of $\psi_f(\boldsymbol{r}, t)$ that are out of phase by angle $\phi$. The waves are functions of a 3-dimensional position vector, $\boldsymbol{r}$, and time parameter, $t$. In order to maximize the amplitude of the superimposed output from Eq. (2.7), the phase difference between the waves must be minimized. Therefore, $\phi$ must be equal to integer multiples of $2\pi$ for fully constructive interference to occur between the reflected waves.

Figure 2.3 (b) shows the same initial plane wave of wave vector $\boldsymbol{k}_i$ scattering from an arrangement of atoms in a Bravais lattice which have positions determined by the vectors $\boldsymbol{r}_1$, $\boldsymbol{r}_2$, and $\boldsymbol{r}_3$. The resulting superposition of the four scattered waves that have identical wave vectors $\boldsymbol{k}_f$ will be of the form:

$$\Psi(\boldsymbol{r}, t) = \psi_f(\boldsymbol{r}, t)\left[1 + e^{i\boldsymbol{q}\cdot\boldsymbol{r}_1} + e^{i\boldsymbol{q}\cdot\boldsymbol{r}_2} + e^{i\boldsymbol{q}\cdot\boldsymbol{r}_3}\right] \tag{2.8}$$
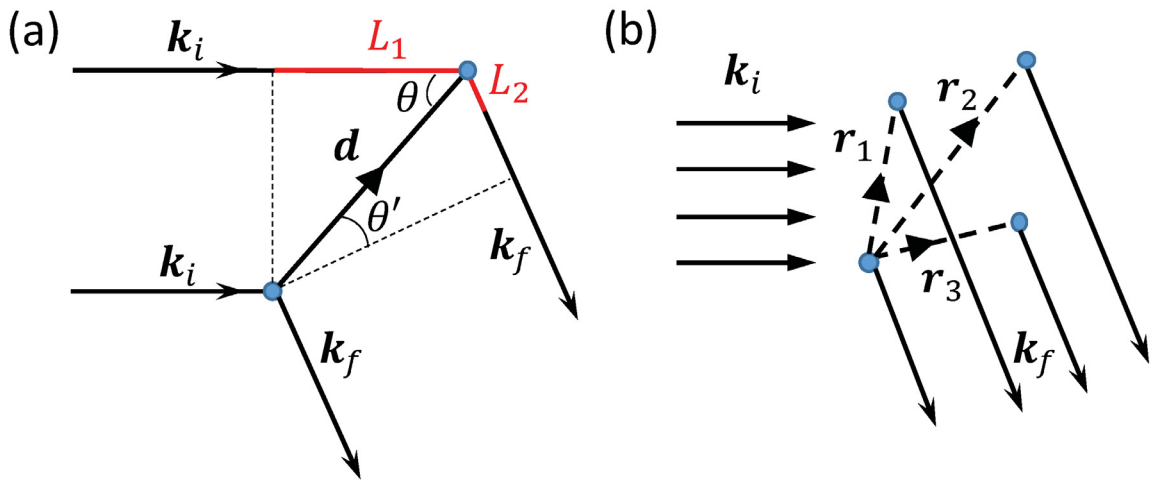
**Figure 2.3:** (a) Illustration of a plane wave with initial wave vector $k_i$ interacting with two atoms separated by displacement vector $d$, which results in two separate plane waves that both have wave vector $k_f$. The reflected waves have an optical path length difference of $L_1 + L_2$ that determines the phase difference. For the reflected waves to be in phase, the optical path length difference must be equal to an integer multiple of wavelength. (b) Illustration of the same initial plane wave with wave vector $k_i$ interacting with atoms of a Bravais lattice whose positions are determined by vectors $r_1$, $r_2$, and $r_3$ as shown. The result is reflected waves of wave vector $k_f$.
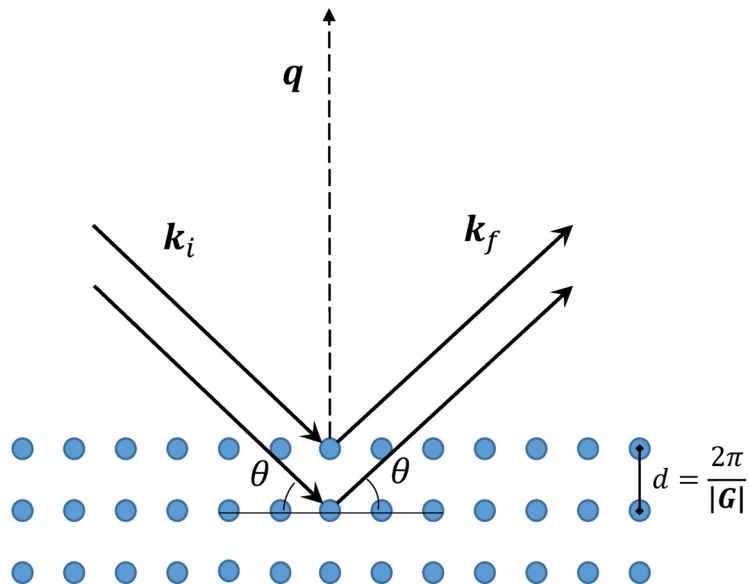


**Figure 2.4:** Illustration of the Bragg condition for coherent scattering from a lattice plane. The scattering vector $q$ is perpendicular to the lattice plane and equal to the corresponding reciprocal lattice vector $G$. The vectors are drawn to scale with respect to one another. The atomic layer spacing, $d$, is labeled between planes perpendicular to reciprocal lattice vector $G$.

where $\boldsymbol{q}$ is defined as the scattering vector:

$$\boldsymbol{q} = \boldsymbol{k}_f - \boldsymbol{k}_i \tag{2.9}$$

For total constructive interference to occur between the reflected waves of Eq. (2.8), the resulting superposition, $\Psi(\boldsymbol{r}, t)$, must be maximized by having:

$$\phi = \boldsymbol{q} \cdot \boldsymbol{R} = 2\pi n \tag{2.10}$$

where $\boldsymbol{R}$ is the Bravais lattice vector and $n$ is an ordering integer. Recalling the constraint of reciprocal lattice vectors in Eq. (2.3), it is apparent that diffraction occurs when $\boldsymbol{q} = \boldsymbol{G}$. That is, when the scattering vector is aligned with the reciprocal lattice vector of a specific $(hkl)$ plane, a coherent diffraction peak will be measured. Figure 2.4 illustrates this condition through a schematic of x-ray scattering due to crystal planes of a lattice. The scattering vector $\boldsymbol{q}$ shown in the figure is perpendicular to the lattice planes and equal to the reciprocal lattice vector $\boldsymbol{G}$. The mathematical definition of Bragg's law can be found by calculating the atomic layer spacing, $d$, in terms of the scattering vector:

$$d = \frac{2\pi n}{|\boldsymbol{q}|} = \frac{2\pi n\lambda}{4\pi\sin\theta} = \frac{n\lambda}{2\sin\theta} \tag{2.11}$$

Rearranging Eq. (2.11) gives the standard form of Bragg's Law:

$$n\lambda = 2d\sin\theta \tag{2.12}$$

### 2.2.3 Calculation of Powder Diffraction Patterns and Rietveld Refinement

X-ray diffraction experiments are typically performed on powder or microcrystalline samples, which provides the benefit of equally representing every possible crystalline orientation of the material. All XRD scans in this thesis work were obtained through powder diffraction. Powder diffraction follows Bragg's law such that each diffraction peak matches to a particular reciprocal lattice vector and corresponding $(hkl)$ plane. It is possible to calculate the powder diffraction pattern of a crystalline material if

properties of the crystal lattice are known. The required lattice properties are: the space group, constituent atoms along with their occupied sites, the lattice parameters of the unit cell, and the radiation source used. Additional considerations have to be made when calculating higher order effects such as the thermal broadening of peaks, strain influences, and fluorescence of elements within the material. One of the most common methods for performing powder diffraction calculations is the Rietveld refinement method [42]. The JCPDS database spectra shown in the XRD pattern stacks throughout Chapters 3 and 4 were originally calculated using similar methods.

The mathematical model that all powder diffraction calculations derive from is the following equation for determining diffraction peak intensity [43]:

$$I(2\theta) = I_0 P(2\theta) L'(2\theta) F^2(h, k, l) M(h, k, l) DW(h, k, l) \tag{2.13}$$

where $P(2\theta)$ is the polarization factor of the radiation, $L'(2\theta)$ is the Lorentz correction factor, $F^2(h, k, l)$ is the geometrical structure factor, $M(h, k, l)$ is the multiplicity of the $(hkl)$ lattice plane, $DW(h, k, l)$ is the Debye-Waller factor, and $I_0$ is a constant. The degree of polarization for a diffraction sample depends upon the diffraction angle, $2\theta_m$, of the monochromator. If the sample, monochromator, and detector exist in the sample plane, then the polarization factor is given by [43]:

$$P(2\theta) = \frac{1 + \cos^2 2\theta \, \cos^2 2\theta_m}{2} \tag{2.14}$$

The Lorentz factor is a correction to the diffractometer geometry. Figure 2.5 shows the scattering geometry of a diffracted beam for a powder diffraction experiment that facilitates the formation of Debye-Scherrer diffraction rings. The beam diffracts in all directions that satisfy the Bragg condition, resulting in rings of constructive interference with an angular separation of $2\theta$ from the dashed red transmission line seen in the figure. The detector window in an XRD experiment views only a portion of the total scattering signal contained in the diffraction ring patterns. The Lorentz factor corrects for this condition by calculating the ratio of measured area over entire diffraction area (*i.e.* an area $d\boldsymbol{q}$ on a sphere with radius defined by scattering vector $\boldsymbol{q}$) to determine the fractional amount of signal actually measured. This quantity is proportional to $\sin 2\theta$ [44].
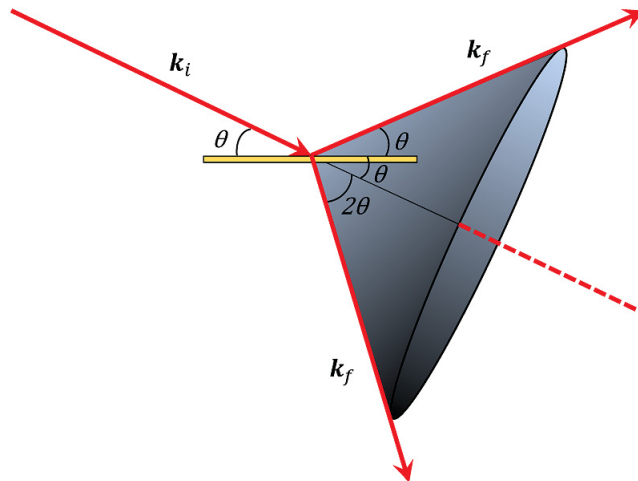
**Figure 2.5:** Illustration of the scattering geometry that gives rise to Debye-Scherrer diffraction ring patterns. The incident beam $\boldsymbol{k}_i$ diffracts in all directions of $2\theta$ surrounding the dashed red transmission line. For every $(hkl)$ diffraction peak there exists a corresponding Debye-Scherrer diffraction ring. Typical XRD measurements observe only the points of these rings along the goniometer axis (*i.e.* the plane parallel to the page). The XRD measurements in this work use an area detector to measure a significant fraction of each diffraction ring existing within the $2\theta$ range observed.

The geometrical structure factor is the key component of Eq. (2.13), as it is the quantity that describes how the atoms within the lattice interfere with incident radiation to produce diffraction peaks. The structure factor of a lattice is mathematically defined as [45]:

$$F(h, k, l) = \sum_{unit\,cell} f_n(\boldsymbol{q}) e^{i\boldsymbol{q} \cdot \boldsymbol{r}'_n} \tag{2.15}$$

where $f_n(\boldsymbol{q})$ is the atomic form factor of atom $n$, $\boldsymbol{r}_n$ is the position vector of atom $n$ within the unit cell, and $\boldsymbol{q}$ is as defined in Eq. (2.9). The atomic form factor is a measure of the scattering amplitude for an incident wave by an isolated atom. Both the type of scattering performed and the incident radiation used modify the atomic form factor. Complete tables of atomic form factors for x-ray diffraction calculations are widely available in reference materials for solid state physics and x-ray diffraction [43, 45]. The geometrical structure factor can be understood intuitively as the superposition of every individual atomic scattering signal from every $(hkl)$ lattice plane in the structure. The multiplicity factor of Eq. (2.13) is an integer value that represents the number of equivalent $(hkl)$ planes that result in diffraction peaks at an

identical angle. Finally, the Debye-Waller factor describes the attenuation of x-ray scattering due to the thermal vibration of atoms within the lattice, resulting in a reduced scattering intensity. The mathematical form of the Debye-Waller factor is denoted by [46]:

$$DW(h, k, l) = e^{-2W} \tag{2.16}$$

and the exponent is of the form $2W = (qu)^2$ where $q$ is the magnitude of the scattering vector defined in Eq. (2.9) and $u$ is the root-mean-square displacement of an atom perpendicular to the $(hkl)$ plane being considered. Alternatively, Eq. (2.16) can be expressed as:

$$DW(h, k, l) = e^{-2B[(\sin\theta)/\lambda]^2} \tag{2.17}$$

in which $B = 8\pi^2 u^2$. The numerical values of these factors for most elemental crystal systems are widely available in crystallographic databases [47].

## 2.3 Combinatorial X-Ray Diffraction

The amount of combinatorial samples produced over the course of this work number in the thousands. As a result, a high-throughput Bruker D8 Discover X-Ray Diffraction system was used to combinatorially characterize all samples. Figure 2.6 is an image of the Bruker XRD machine used. The Bruker uses a Cu-K$\alpha$ radiation source that is collimated into a 0.5 mm wide beam by reflection off of a Göbel mirror. Each XRD scan was constructed from three separate 300 second frames which had 30 % overlap. The three overlapping frames were stitched together by the Bruker software to generate a full 2-dimensional pattern over a $2\theta$ range of 15 to 70°. This scanning procedure was originally created and implemented by McCalla while working on the Li-Ni-Mn-O system [8].

Figure 2.7 (a) shows the output from the Bruker software stitching process and (b) shows the familiar form of a 1-dimensional XRD pattern obtained from integrating the 2-dimensional Bruker plot. The bright fringes seen in Figure 2.7 (a) are sections of the Debye-Scherrer rings for the sample as explained in Section 2.2 and Figure 2.5. A standard XRD machine that lacks an area detector would only measure the small section of these rings that lie along the horizontal axis of Figure 2.7 (a). Every sample was scanned over a $2\theta$ range of 15-70° and a full scan required approximately

**Figure 2.6:** The Bruker D8 Discover unit used for all XRD measurements in this thesis. Both arms are mounted onto the circular goniometer in the center. The x-ray tube on the left emits radiation directly onto a Göbel mirror that collimates the beam toward the sample stage in the center. The Vantec-2000 area detector mounted on the right arm measures portions of the Debye-Scherrer rings between 15 and 70°.
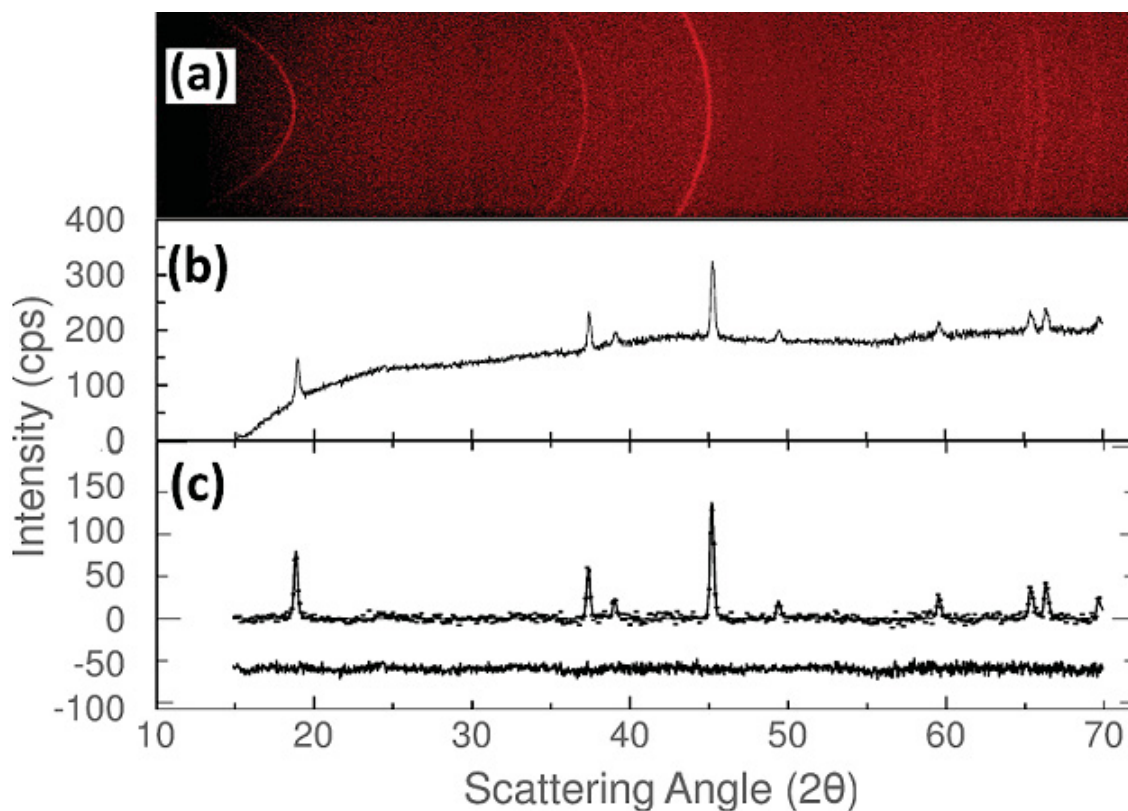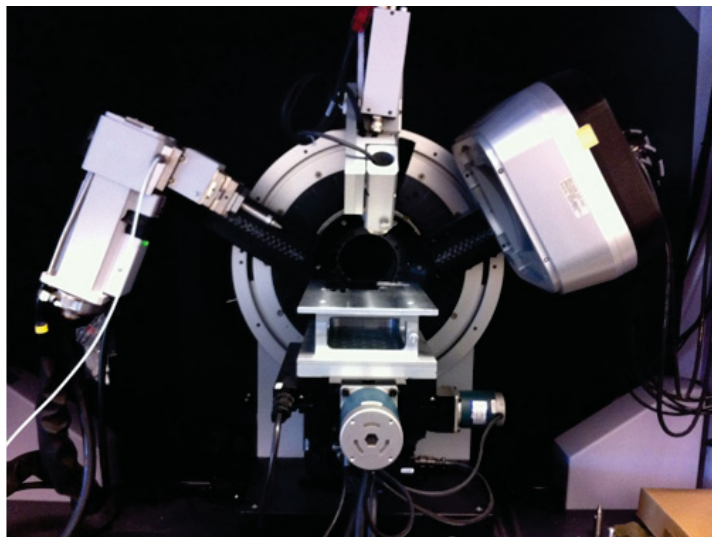




**Figure 2.7:** (a) The Bruker software result from the stitching procedure performed on the three frames taken for a combinatorial sample of $LiCoO_2$. The bright arcs correspond to the Debye-Scherrer rings of the sample. (b) Familiar 1-dimensional form of XRD pattern as a result of integrating the above signal over the 15 to 70° range by the Bruker software. (c) Entire scan profile fit obtained for the XRD pattern above, reflecting the quality of fit typical for all XRD scans measured with the Bruker diffractometer. For clarity, only every fourth data point is included as *closed points* while the fit is a *solid line* and the difference plot is included below.

15 min per sample. The Bruker D8 Discover is equipped with a programmable sample translation stage with full freedom of movement in the $x$, $y$, and $z$ directions, allowing for automated sequential measurement of all samples in a composition array. A silicon (100) single crystal substrate was used as a zero-background sample holder during all XRD scans. The tacky mixture of Trilene-65 and cyclohexane used to adhere the oxides to the surface of the silicon wafer has no diffraction peaks and does not significantly interact with x-rays. The Vantec-2000 area detector of the Bruker allowed for accurate diffraction peak positions to be determined from measuring the Debye-Scherrer rings of samples. However, these measurements come at the cost of distorted peak intensities due to the Bruker software process of frame stitching and integration. Rietveld refinement techniques fail on scans produced in this manner due to the relative peak intensities being different from calculated intensities.

Note the seemingly strange background signal present in the XRD scan of Figure 2.7 (b). This type of background signal is present in all combinatorial XRD patterns of this work is due to the combination of both the software stitching process and the fluorescence of cobalt and manganese. The composition corresponding to the XRD data shown in Figures 2.7 (a)-(c) is $LiCoO_2$, so the background observed in Figure 2.7 (b) is a combination of cobalt flourescence and the effects of the frame stitching process. These background artifacts are unavoidable when using the high-throughput Bruker machine to characterize samples. Figure 2.7 (c) shows the result of the combinatorial XRD fitting that will be detailed in the next section. The troublesome background seen in Figure 2.7 (b) has been removed during the fitting process, which results in the plot shown in Figure 2.7 (c). The quality of data and fit shown here are typical for all samples in this work.

## 2.4   Combinatorial XRD Fitting

As mentioned previously, the high-throughput scan method used with the Bruker XRD machine is ideal for retrieving lattice information from combinatorial samples, but comes at the price of distorting relative peak intensities. This peak distortion renders Rietveld refinement methods inoperable and an alternative method for extracting lattice parameters must be found. Carey [13] alleviated this issue by fitting the profile of individual XRD peaks of single-phase materials with

pseudo-Voigt functions whose positions were characterized by the lattice parameters of the material. However, this method fails with multiphase materials due to peak overlap making it difficult to precisely discern phases and corresponding lattice parameters. This issue was overcome by McCalla, who wrote XRD profile fitting software in the Yorick programming language that fits entire combinatorial XRD scans using a nonlinear least squares fitting algorithm as described by Bevington [8, 48].

To properly fit the background signal in a manner that converged quickly, McCalla utilized a piece-wise cubic polynomial with two broad asymmetric Gaussians centered near 20° and 45°. The positioning of the Gaussians, their shape, and the parameters of the cubic polynomial were allowed to vary and be optimized individually for each scan using the least squares method. The procedure worked well for all samples studied, including spinel samples where the high manganese content creates large amounts of fluorescence that exacerbates the complicated background observed after stitching the Bruker frames together as seen in Figure 2.7 (b).

McCalla's software described each XRD peak by the convolution of the sample scattering signal with the machine broadening function as outlined by Warren [49]:

$$I_k(2\theta) = \int F_k(2\theta - z)M(z)dz \tag{2.18}$$

where $2\theta$ is the scattering angle, $F_k$ is the sample scattering due to the $k^{\text{th}}$ peak, and $M(z)$ is the machine broadening function normalized to have unity area. This integration was performed numerically over the scattering angle, $z$, of the machine broadening within the program for each diffraction peak. The sample scattering signal was described by a pseudo-Voigt function:

$$F_k(2\theta) = I_k'\big[\eta L(2\theta, 2\theta_k, H_k) + (1 - \eta)G(2\theta, 2\theta_k, H_k)\big] \tag{2.19}$$

where $I_k'$ is the integrated peak intensity of the $k^{\text{th}}$ peak, $\eta$ is the Lorentz component where $0 \leq \eta \leq 1$ and it controls the fractional contribution of the Lorentzian and Gaussian components to the resulting peak profile, $2\theta_k$ is the position of the center of the peak, $H_k$ is the full width at half maximum (FWHM),

and $L$ and $G$ are the Lorentzian and Gaussian functions that are normalized to have unity area. The peak intensities were treated as fitting parameters within the program, which served to alleviate any issue with distortion due to the stitching of frames. Due to the majority of compositions studied in this thesis work not having published lattice parameters, the $(hkl)$ values and initial lattice parameters used in the fitting procedure were those of nearby relevant compositions published in the Joint Committee on Powder Diffraction (JCPDS) database (*e.g.* single-phase spinel compositions near $LiMn_2O_4$ used published $LiMn_2O_4$ lattice parameters to calculate initial peak positions that were then refined and adjusted during the fitting procedure). The Cu-K$\alpha_1$ and Cu-K$\alpha_2$ peaks were included in a 2:1 ratio during the calculation to help fit higher angle peaks more accurately.

McCalla determined the machine broadening function, $M$, by measuring the scattering profile from corundum (NIST standard 1976a), which has an expected diffraction pattern given in JCPDS #46-1212 [8]. McCalla fit the corundum scan using pseudo-Voigt functions with $\eta = 0.5$ and letting the FWHM of each peak be a fitting parameter. The results of these calibration fits also determined an optimal frame overlap of 30 % to minimize the effect of background artifacts from the frame stitching process.

Figure 2.7 (c) shows a typical fitting result for a scan obtained for a combinatorial $LiCoO_2$ sample measured with the Bruker machine. The in-house software fitted the experimental data extremely well and resulted in lattice parameter measurements accurate to the order of $\pm$ 0.001 Å. For clarity, all XRD patterns presented throughout the rest of this thesis have fitted backgrounds subtracted in order to clearly compare results. To fit multiphase samples, the calculated pattern became a linear combination of the functions representing each single-phase. The multiphase fits performed were able to generate similarly accurate lattice parameters and integrated peak areas for each fitted phase as compared to the single-phase fits. The phase composition of a multiphase sample could be determined by comparing the peak areas of the fitted phases, as will be described in the next section. All combinatorial samples within this thesis work were measured with XRD and fitted for lattice parameters and peak area using the described fitting method methods.

## 2.5   Construction of Phase Diagrams

The phase diagrams of the Li-Ni-Mn-Co-O system presented in this thesis were constructed from the information extracted from fitting the XRD scans of samples. These extracted parameters include phase type (cubic spinel, tetragonal spinel, layered, or rocksalt), lattice parameters, and the peak areas of each peak for all phases present. Using these results, it is possible to map out the location of single-phase samples throughout the Li-Ni-Mn-Co-O Gibbs pyramid and then figure out the boundaries to the phase region they define. The general procedure for constructing a Gibbs triangle from scratch with a series of newly fitted scans is to first observe the phase content of a sample (*e.g.* single-phase spinel, multiphase layered-spinel, . . . ) and then indicate it accordingly on the Gibbs triangle. After completing this task for a series of samples that span the Gibbs triangle, it is typically apparent the location, size, and general shape of the single-phase regions from inspection. The lever rule was used to quantitatively determine the boundaries of single-phase regions where there were only three elements present (*i.e.* the faces of the Gibbs pyramid).

Figure 2.8 is a schematic of the lever rule being applied to an arbitrary multiphase sample 'X' located at the midpoint of a tie-line connecting phases A and B. The mathematical form of lever rule states that the fraction of phase A in sample 'X' is equal to d(X,B)/d(A,B). Similarily, the fraction of phase B in sample 'X' is equal to d(A,X)/d(A,B). The ratio of peak areas for either phase A or B in sample 'X' to that of their respective endpoint phase can be used to extrapolate the position where the phase is no longer present, which results a point on the single-phase boundary for the other phase. Repeating this process over multiple tie-lines results a series of points which define a single-phase boundary line.

This lever rule method can, in principle, be performed away from the faces of the Gibbs pyramid, but the added fourth element in such regions makes the task considerably more difficult due to the extra spatial dimension within the calculation. As it will be discussed in Chapter 4, tie-lines extending through the multiphase regions of the cobalt slice ternary phase diagrams are able to connect to phases existing out of plane from the ternary at a higher or lower cobalt contents. A careful mapping of the entire Gibbs pyramid would be required to precisely discern
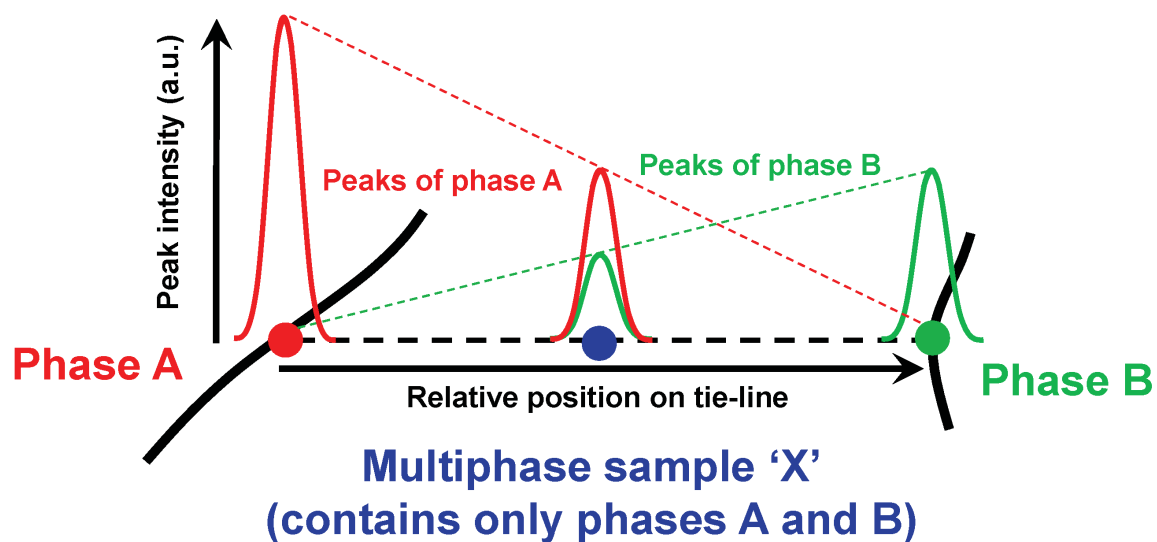
**Figure 2.8:** Schematic of the lever rule method used to determine the lower boundary of the single-phase cubic spinel region in the quenched Li-Co-Mn-O pseudo-ternary system. The solid black lines represent arbitrary boundaries to single-phase regions that are able to be determined by this method. The vertical axis compares the XRD peaks between arbitrary phases A and B, which are drawn in red and green respectively, and the horizontal axis indicates relative position along the tie-line connecting them. Sample 'X' is located at the midpoint between phases A and B and therefore contains equal parts of phase A and B. The dotted lines connecting the top of each peak illustrate the decrease in content of the phase within samples when moving along the tie-line toward the opposite phase.

the direction and length of these tie-lines. In lieu of this, the boundaries were drawn by inspection between the single-phase and multiphase compositions on the diagram. The high sampling density in the single-phase regions also provided many lattice parameters over a wide range of compositions that were used to generate lattice parameter contour plots in Chapters 3 and 4. These contour plots should prove useful for researchers synthesizing materials within these systems. The fitted lattice parameters from observed single-phase samples within the 10 %, 20 % and 30 % cobalt slice ternary phase diagrams determined in this work are summarized in Appendix A.

## 2.6 Elemental Analysis

Samples synthesized near the lithium corner of the Li-Ni-Mn-Co-O Gibbs pyramid lose lithium during heating through the formation of $Li_2O_2$, which causes the composition of the sample to shift away from what was targeted [8]. In order to further investigate this effect and to also obtain supporting evidence for the precision of the dispensing

method, inductively coupled plasma (ICP) atomic absorption measurements were performed on a series of samples synthesized with high Li content. The results of this study will be shown in Chapter 4. In order to perform these measurements on combinatorial samples, each sample had to be carefully transferred into individual 2 mL vials using a stainless steel scapula that was cleaned with isopropyl alcohol between each transfer to prevent mixing. Approximately 0.5 mL of a prepared aqua regia solution (75 % hydrochloric acid and 25 % nitric acid) was added to each vial in order to dissociate the metals of the oxide compounds. The solutions were then analyzed by Dan Chevalier (Minerals Engineering Center, Dalhousie University) to obtain the concentrations of lithium, nickel, manganese and cobalt in the samples to a 5 % accuracy. For the starting solutions used to dispense the samples with the solution-processing robot, ICP measurements were repeated three separate times to obtain an uncertainty of 3 %.

## 2.7 Considerations Regarding the Formula Units of Cubic Spinel and Hexagonal Layered Materials

Since the crystal structures of cubic spinel and hexagonal layered materials are different as was shown in Figure 1.2, a method will need to be developed in order to directly compare the lattice parameters obtained for single-phase samples of both structures. The method explained here will calculate the unit cell volume for two oxygen atoms and associated metals in each structure (*i.e.* comparing the cubic spinel and hexagonal layered structures by considering a unit cell of a basis $MO_2$ unit).

In the unit cell of layered $LiMO_2$, three 'M' atoms are located in octahedral sites and three 'Li' atoms fit in interstitial octahedral sites. In the unit cell of cubic spinel $M_3O_4$, there are 24 'M' atoms total, 16 of which are located in octahedral sites and the remaining 8 atoms are in tetrahedral sites. The oxygen content in the unit cell of these materials is determined by the formula unit of their composition. The hexagonal layered materials have a 1 : 1 metal-to-oxygen ratio and cubic spinel materials have a 3 : 4 metal-to-oxygen ratio in their unit cells. This results 6 oxygen atoms in the unit cell of the layered structure $LiMO_2$ and 32 oxygen atoms in the unit cell of spinel structure $M_3O_4$. Thus, the volumes of unit cells for cubic spinel

and hexagonal layered materials can be directly compared if their unit cell volumes are scaled by their respective oxygen contents (*i.e.* comparing the volume of a $MO_2$ unit for cubic spinel and layered structures). This results in a ratio of 3/16 for the unit cell oxygen content of layered materials to that of spinel materials. This ratio is also the same as the ratio for metal atoms in octahedral sites in layered and spinel structures. This calculation will be used in Section 4.4 to compare the lattice parameters of cubic spinel and hexagonal layered single-phase materials within the regular-cooled 10 % cobalt slice ternary system.

# Chapter 3

# Combinatorial Analysis of the Cubic Spinel Region of the Li-Co-Mn-O Pseudo-Ternary System

## 3.1 Experimental Details

Figure 3.1 shows the results of the project investigating the Li-Co-Mn-O pseudo-ternary system for samples heated in air at 800°C for 3 h and (a) quenched or (b) regular-cooled. As is true throughout the entire Li-Ni-Mn-Co-O system, two single-phase regions exist in this system that are of interest for lithium-ion battery researchers: the spinel and layered regions. The two solid solution lines existing on the Co-Mn binary of both cooling rates are of a tetragonal spinel phase (containing $CoMn_2O_4$) and a bixbyite phase (containing $Mn_2O_3$). The single-phase layered region of the Li-Co-Mn-O pseudo-ternary system is restricted to a solid solution line extending from $LiCoO_2$ to $Li_2MnO_3$ and it can phase separate into layered-layered multiphase materials through lower cooling rates as observed by McCalla [18]. The work presented in this chapter focuses on the spinel region, which in the quenched system (Figure 3.1 (a)) spans the triangular region with vertices at $Co_3O_4$, $Co_2MnO_4$, and $LiMn_2O_4$ on the ternary phase diagram. For the regular-cooled system shown in Figure 3.1 (b), the single-phase spinel region extends from $Co_3O_4$ to $LiMn_2O_4$ and is smaller than the quenched region. The work on the layered solid solution line and determination of tie-lines in this system for both quenched and regular-cooled samples was done by McCalla [8, 9, 18].

Every sample was prepared combinatorially following the synthesis method described in Section 2.1. The entire Li-Mn-Co oxide Gibbs triangle was initially mapped out with 66 unique samples equally spaced throughout the entire system. A complete Gibbs triangle was constructed for both quenched and regular-cooled samples during this study. The broad initial survey of the whole Li-Mn-Co-O pseudo-ternary system revealed a large single-phase cubic spinel region existing for
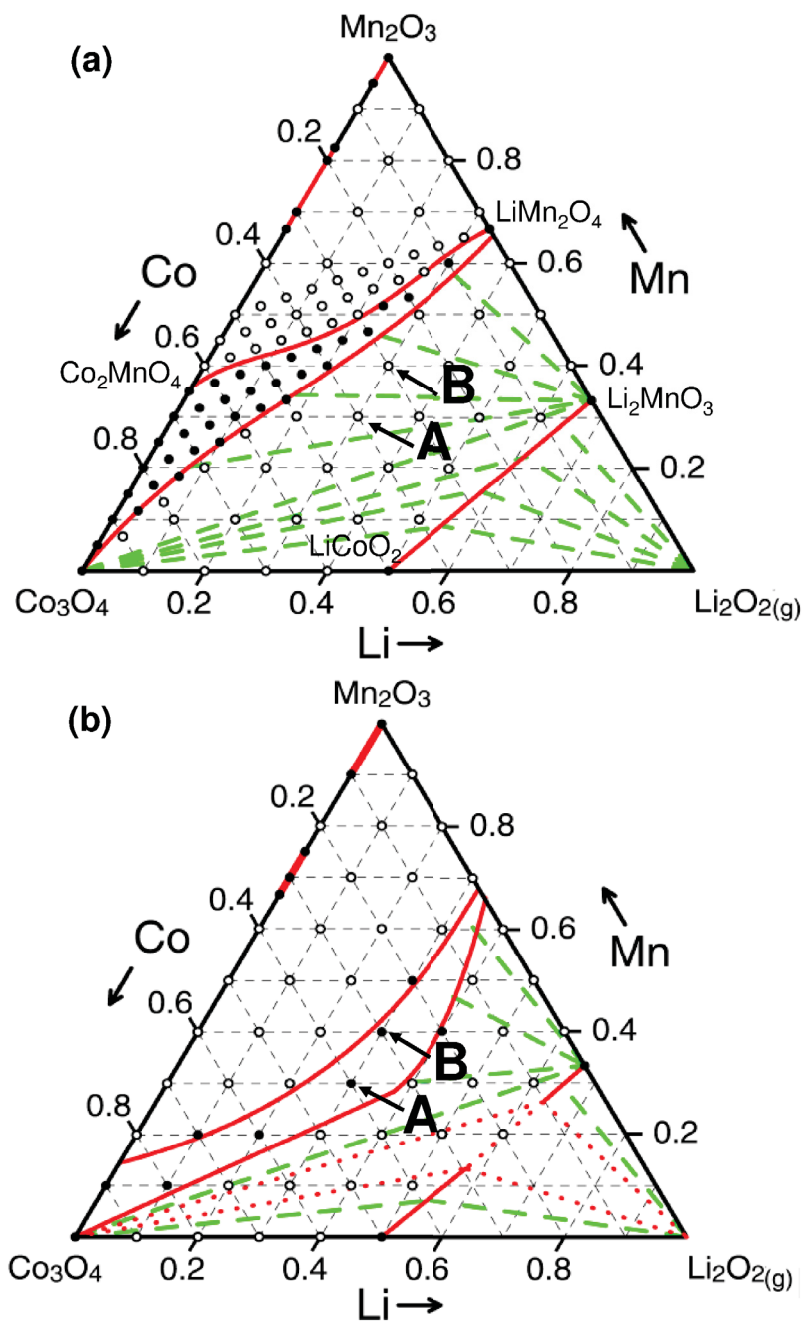
**Figure 3.1:** The entire Gibbs triangles for samples heated to 800°C for 3 h in air and (a) quenched or (b) regular-cooled. As with all ternaries presented in this work, single and two-phase samples are indicated by black filled and empty circles respectively. Green dashed lines are tie-lines, solid red lines are boundaries to single-phase regions and red dotted lines are boundaries to 3-phase regions. The two solid-solution lines on the Co-Mn binary are of a tetragonal spinel (including $CoMn_2O_4$) and a bixbyite (including $Mn_2O_3$) phase. The samples labeled A [0.4 Co, 0.3 Mn] and B [0.3 Co, 0.4 Mn] will be discussed later. (Reprinted from [24] with permission from Elsevier)

**Figure 3.2:** Fitted XRD data of samples quenched from 800°C with compositions spanning the cubic spinel region from $Co_3O_4$ to $LiMn_2O_4$. The red arrow matches the XRD data to their position on the phase diagram. The vertical lines in the XRD stack indicate peaks from the JCPDS database, reference #74-1656 for $Co_3O_4$ and #89-6541 for $LiMn_2O_4$. The filled and empty black circles in the phase diagram indicate single and two phase samples respectively. The green dashed lines are tie-lines between cubic spinel and layered phases. (Reprinted from [24] with permission from Elsevier)
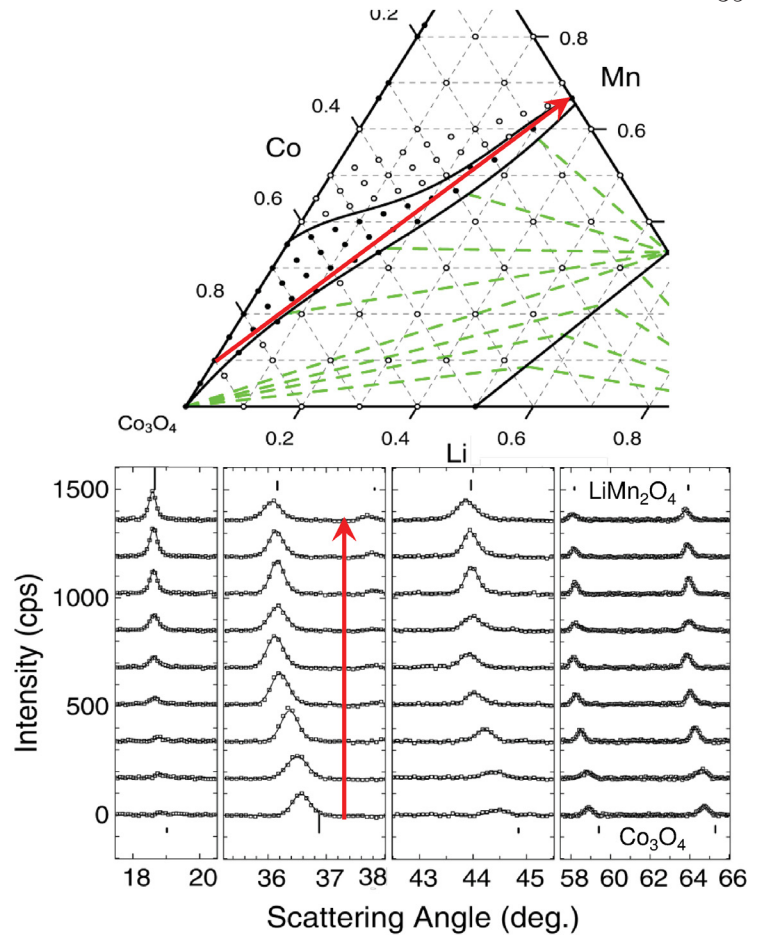
both cooling rates studied. To study the spinel region further, a triangular 'zoom-in' composition series was prepared in the quenched Li-Co-Mn-O pseudo-ternary system with vertices at [1 Co, 0 Mn], [0.5 Co, 0.5 Mn], and [0 Co, 0.66 Mn]. The 'zoom-in' series followed the same dispensing procedure as explained in Section 2.1, the only modification being the different starting solution compositions. The resulting 66 unique compositions of the 'zoom-in' series can be seen in Figures 3.1 (a), 3.2, and 3.3 (a) as the triangular region with higher sample density that spans the single-phase spinel region. After heating, samples were transferred onto a silicon (100) substrate and characterized using a Bruker D8 Discover X-ray Diffractometer using the methods described in Section 2.3. In-house written software was used to fit entire XRD patterns in order to extract lattice parameters and phase compositions as described in Section 2.4.

## 3.2   Cubic Spinel Single-Phase Region

Figure 3.2 shows a stack of XRD scans obtained from quenched samples belonging to the cubic spinel region of Figure 3.1 (a). On close inspection of the XRD stack, it is apparent that every sample is part of a solid solution that extends across the entire single-phase spinel region. The cubic lattice constant, $a$, of the spinel phase increases as the compositions vary from $Co_3O_4$ to $LiMn_2O_4$, resulting in the observed shift of XRD peaks to lower angles. This result is consistent with the random substitution of cobalt atoms at $8a$ and $16d$ sites in the spinel structure for lithium and manganese atoms that results in a larger lattice. The sample of $Co_3O_4$ prepared by quenching from 800°C had a measured cubic lattice constant of $8.083 \pm 0.003$ Å and the corresponding $LiMn_2O_4$ sample had $a_{cub} = 8.243 \pm 0.001$ Å. For the same composition of samples that were regular-cooled from 800°C, the cubic lattice constants were $8.084 \pm 0.004$ Å for $Co_3O_4$ and $8.243 \pm 0.001$ Å for $LiMn_2O_4$. Thus, there was little noticeable difference in cubic lattice constant between samples that were quenched and those that were regular-cooled at the endpoints of the spinel boundary. Both sets of lattice parameters are in close agreement with the literature values of $8.084$ Å (JCPDS #74-2120) and $8.243$ Å (JCPDS #89-6541) for $Co_3O_4$ and $LiMn_2O_4$ respectively.

Figure 3.3 (a) shows the contour plot of the cubic lattice parameter for the 800°C quenched Li-Co-Mn oxide cubic spinel region. The approximately triangular spinel region contains the compositions $Co_3O_4$, $Co_2MnO_4$, and $LiMn_2O_4$ at its corners. The boundaries to the single-phase region were determined using the lever rule as described in Section 2.5. The cubic spinel boundary located along the Co-Mn binary was found to extend from $x = 1.92$ to 3 for $Co_xMn_{3-x}O_4$, which is a much smaller region than the one expected to extended from $x = 1.1$ to 3 for $Co_xMn_{3-x}O_4$ by Aukrust and Muan [23]. The key difference between the two sets of data is that the Aukrust and Muan samples were synthesized in bulk and as a result were much larger than the combinatorial samples prepared during this study. Oxygen uptake is more difficult for bulk samples due to a lower surface area to volume ratio than that of combinatorial samples. A decrease in oxygen uptake would allow for the higher $(3:4)$ metal to oxygen ratio spinel phase to be energetically favored over the lower $(2:3)$ metal to oxygen ratio bixbyite phase. Furthermore, the reliability of the

**Figure 3.3:** Contour plots of the cubic lattice parameter in the spinel region for samples (a) quenched and (b) regular-cooled from 800°C. The lattice parameters were obtained through XRD peak fitting of the single-phase samples prepared in this region. The contour lines are drawn in red with corresponding labels. Dashed green lines indicate tie-lines and single and two-phase samples are indicated by black filled and empty circles respectively. The dotted black lines in (b) are boundaries to 3-phase regions. The light blue dots in (a) indicate points determined from the lever rule that were used to define the lower spinel boundary. The blue line in (b) corresponds to the $LiCo_xMn_{2-x}O_4$ $(0 \leq x \leq 0.66)$ spinel solid solution line measured by Amarilla et. al. [20] at 600°C with regular-cooling. (Reprinted from [24] with permission from Elsevier)
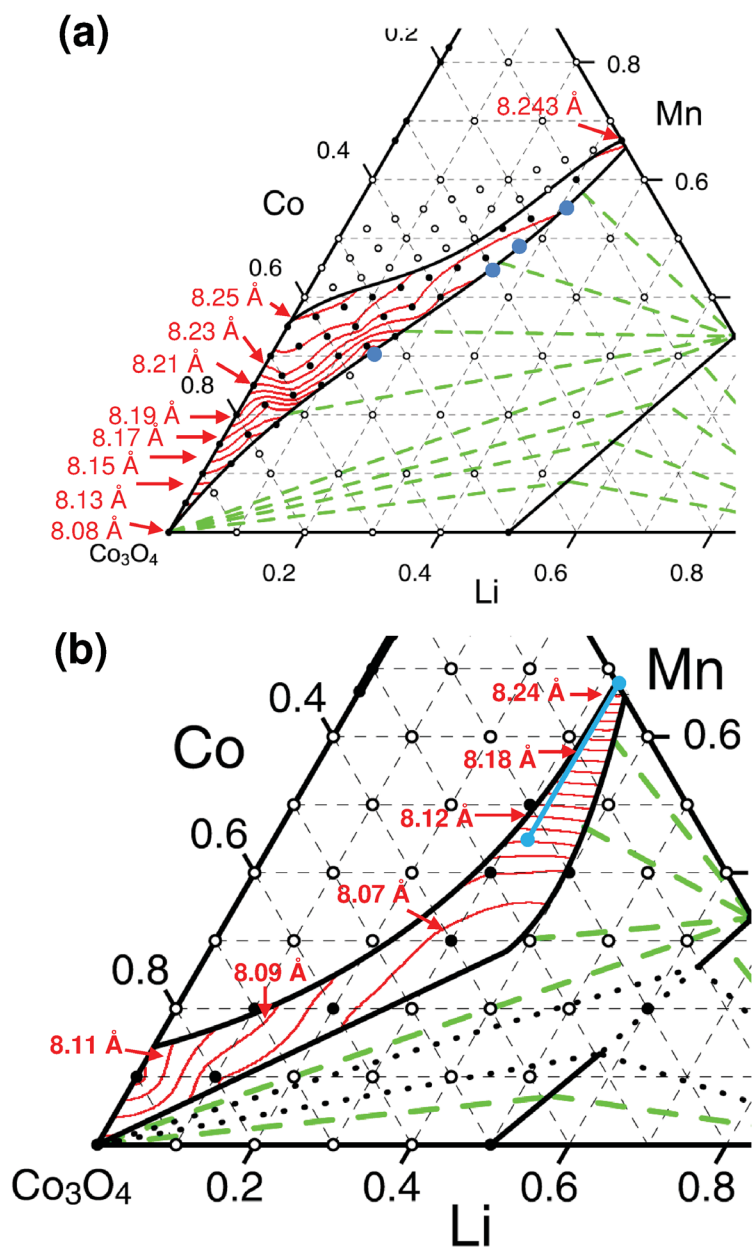
Aukrust and Muan binary for this temperature is suspect since it was extrapolated from a few data points in the surrounding region. Due to the lack of Co-Mn oxide binary data existing in the literature at 800°C, the Aukrust and Muan results were all that could be found to compare. The spinel boundary existing along the Li-Mn binary was set to match the boundary determined by Paulsen and Dahn which runs from $x = 1$ to 1.07 for $Li_{1+x}Mn_{2-x}O_4$ when heated in air at 800°C [12]. The contour lines of Figure 3.3 (a) were calculated from the fitting results of 20 unique and evenly spaced single-phase compositions existing within the spinel region.

Figure 3.3 (b) shows the contour plot for the cubic lattice parameter of the 800°C regular-cooled Li-Co-Mn oxide cubic spinel region. There were fewer samples synthesized in the regular-cooled spinel region than in the corresponding quenched system due only having performed the initial survey series of 66 samples for the entire Gibbs triangle as described in Section 2.1. This resulted in the contour plots of this system being generated from only 10 fitted lattice parameter values, which is half the amount used for the contour plot of the quenched spinel region shown in Figure 3.3 (a). The blue line in Figure 3.3 (b) illustrates the $LiCo_xMn_{2-x}O_4$ $(0 \leq x \leq 0.66)$ spinel solid solution measured by Amarilla et al. at 600°C with regular-cooling and lies entirely within the spinel region determined here [20]. The lattice constants for the solid solution measured by Amarilla et al. ranged from $8.21\,\text{Å}$ at $LiMn_2O_4$ to $8.07\,\text{Å}$ at $LiCo_{0.66}Mn_{1.34}O_4$, whereas those found in this study ranged from $8.24\,\text{Å}$ to $8.10\,\text{Å}$ for the same compositions. The larger lattice constants from this experiment are hypothesized to be the result of a higher synthesis temperature causing more oxygen vacancies to be present in the samples. A minimum lattice constant of $8.065\,\text{Å}$ is located near the center of the regular-cooled spinel region as seen in the contour plot of Figure 3.3 (b).

The phase boundaries for the quenched cubic spinel region were determined using the lever rule as described in Section 2.5. The lower boundary to the spinel region was extrapolated from lever points (shown in light blue in Figure 3.3 (a)) that were determined from the ratio of fitted XRD peak areas of the cubic and layered phases present in samples located along the corresponding tie-lines. The calculated spinel boundary in the quenched system was in good agreement with the result expected by visual inspection of the XRD samples whereby all single-phase samples are contained by the boundary line and all multiphase samples are excluded. Due to the sample density of the regular-cooled system being too low to use lever rule method, the regular-cooled spinel boundary was estimated by a best fit line running through the bounding single-phase cubic spinel points. A similar procedure was performed on the upper boundary, except the additional phase fitted for in the co-existence region to distinguish between single-phase and multiphase samples was tetragonal spinel instead of layered.

Figure 3.4 shows XRD scans for samples A and B labeled in the phase diagrams
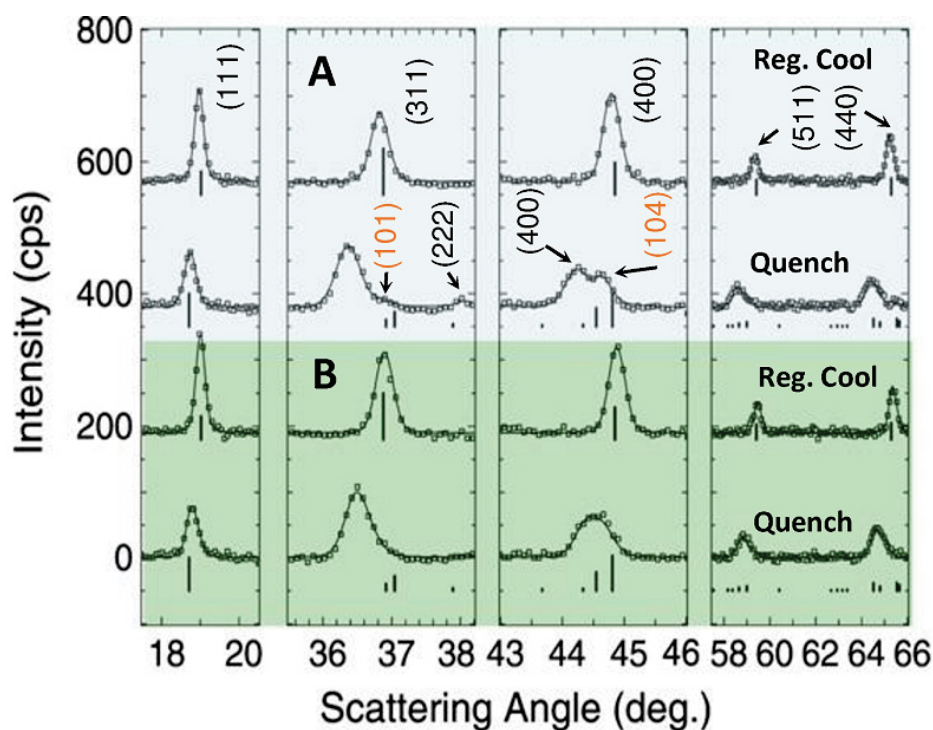
**Figure 3.4:** XRD data stack reinforcing the phase boundary shift observed between quenched and regular-cooled samples. The solid lines through the points are fits to the data. The scans included are of samples A and B, which are defined in Figure 3.1. Each XRD pattern has its cooling rate indicated. The solid vertical lines under the regular-cooled and quenched peaks are the database spectra for $Co_3O_4$ (JCPDS #74-1656) and $LiMn_2O_4$ (JCPDS #89-6541) respectively. The $(hkl)$ of each peak is labeled in black for spinel and orange for layered. The background color is to help distinguish between the two samples. (Reprinted from [24] with permission from Elsevier)

of Figure 3.1. Both quenched samples are distinctly two-phase layered and spinel while the regular-cooled samples are single-phase cubic spinel. These two samples were chosen simply to reinforce the claim that the spinel boundary shifts due to cooling rate. The same result is found when comparing the XRD fits of any sample that exists as a multiphase layered-spinel when quenched and single-phase spinel when regular-cooled (compare Figures 3.1 (a) and 3.1 (b)). When regular-cooled, the single-phase spinel region of the Li-Co-Mn oxide system shifts toward lower oxygen content regions. During heating, oxygen has been shown to be evolved from oxide samples [10]. Regular-cooling allows time for the reuptake of oxygen into the crystal structure of the sample. Quenched samples are not able to experience as much oxygen reuptake because the structure is locked into the high temperature oxygen-deprived state as a result of the quenching process. Regular-cooled samples therefore should have a higher fractional oxygen content, which favors the formation
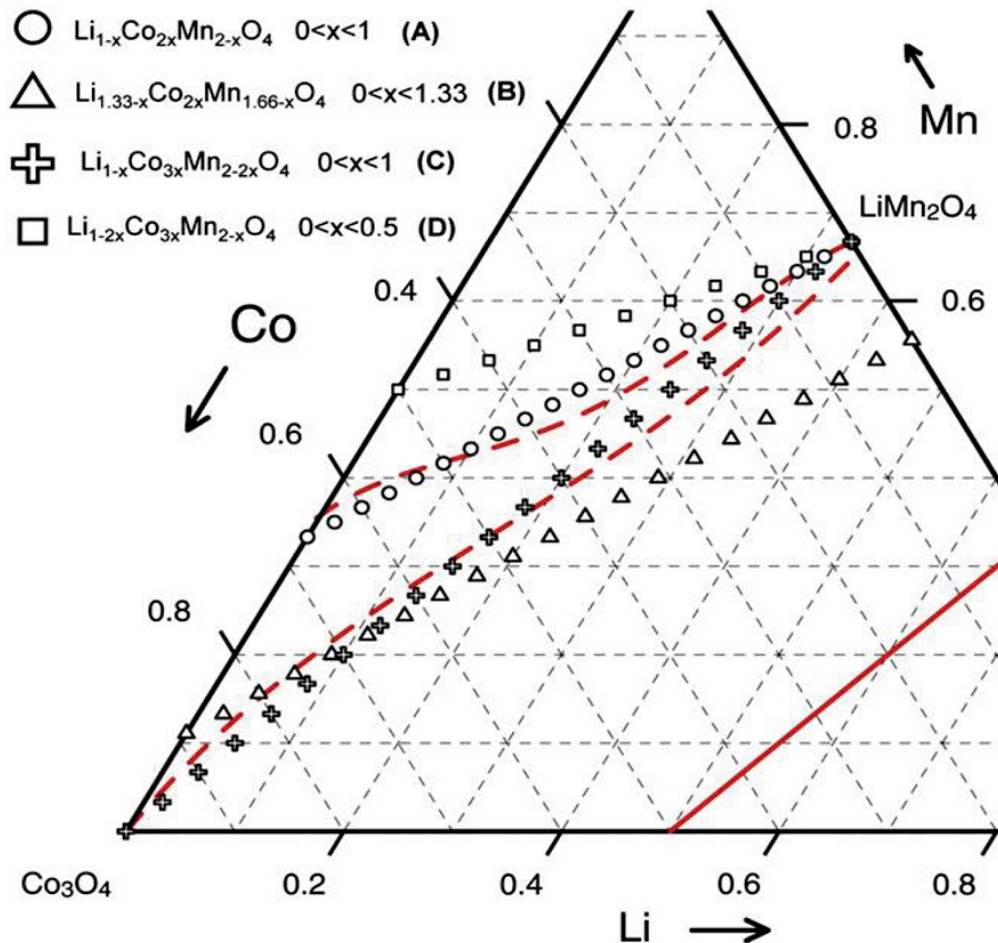
**Figure 3.5:** Possible boundaries of the quenched 800°C Li-Co-Mn oxide cubic spinel region determined from oxidation state considerations alone. Labeled composition lines, A through D, illustrate various possible solid solution series on the ternary diagram. Red dashed lines outline the single-phase cubic spinel region determined experimentally for the quenched samples in this system and the solid red line represents the layered solid solution. (Reprinted from [24] with permission from Elsevier)

of oxygen-rich structures. The four types of phases present in the Li-Co-Mn-O system in order of increasing oxygen to metal ratio are: layered $(1:1)$, cubic and tetragonal spinel $(4:3)$, and bixbyite $(3:2)$. Since the spinel phases have higher oxygen content than the layered phases they are favored during regular-cooling [25]. This effect results in the shift toward the layered region seen in the lower boundary of the spinel region between quench and regular-cooling. An identical argument can be applied to understand the downward shift of the top boundary of the spinel region where $Mn_2O_3$ has the largest oxygen to metal ratio in the entire system and is therefore favored during regular-cooling. This hypothesis also helps explain the

enlarged co-existence region observed above the regular-cooled spinel region in Figure 3.3 (b). This co-existence region involves two distinct spinel phases (cubic and tetragonal) and a third bixbyite phase. The combined result is a rather complicated multiphase region that has the potential to be either 2 or 3 phase regardless of cooling rate. Due to the difficulty and lack of interesting battery materials in this coexistence region, the tie-lines and locations of any possible 3-phase regions were not determined above the spinel region for either cooling method studied.

Figure 3.5 shows the theoretically allowed composition lines for the cubic spinel structure determined from oxidation state considerations alone. The included ternary is of the Li-Co-Mn-O pseudo-ternary system quenched from 800°C as seen in Figures 3.1 (a), 3.2 and 3.3 (a). The dashed red lines on the plot indicate boundary lines to the single-phase spinel region and the solid red line represents the layered solid solution line. The four labeled composition lines represent the swapping of atom combinations that have equal net oxidation states. The allowed oxidation states of metals in the Li-Co-Mn-O cubic spinel structure are: $Li^+$, $Co^{2+}$, $Co^{3+}$, $Mn^{3+}$ and $Mn^{4+}$. In $LiMn_2O_4$, the manganese atoms are allocated evenly to the oxidation states of $Mn^{3+}$ and $Mn^{4+}$. From $x = 0$ to $x = 0.5$ in $Li_{1-2x}Co_{3x}Mn_{2-x}O_4$ (curve D in Figure 3.5), $Li^+$ and $Mn^{4+}$ are being substituted with $Co^{2+}$, resulting in $Co_{1.5}Mn_{1.5}O_4$ as the limiting composition when $x = 0.5$. From $x = 0$ to $x = 1$ in $Li_{1-x}Co_{2x}Mn_{2-x}O_4$ (curve A in Figure 3.5), $Li^+$ and $Mn^{3+}$ are being substituted with $Co^{2+}$, resulting in $Co_2MnO_4$ as the limiting composition when $x = 1$. The resulting composition line closely follows the upper boundary of the single-phase cubic spinel region. From $x = 0$ to $x = 1$ in $Li_{1-x}Co_{3x}Mn_{2-2x}O_4$ (curve C in Figure 3.5), $Li^+$, $Mn^{3+}$, and $Mn^{4+}$ are being substituted with $Co^{2+}$ and $Co^{3+}$, resulting in $Co_3O_4$. This composition line closely follows the lower cubic spinel boundary. The presence of $Co^{2+}$ is more prevalent in quenched samples than in regular-cooled samples due to $Co^{2+}$ oxidizing to $Co^{3+}$ while cooling in air. Having more $Co^{2+}$ available in addition to $Co^{3+}$ allows for a wider range of single-phase compositions to exist in the spinel region, which helps explain the difference in size of the quenched cubic spinel region compared to the regular-cooled spinel region. The quenched system is able to have a wider amount of spinel compositions than in

the regular-cooled system due to the higher available $Co^{2+}$ content in the quenched system. For instance, the composition $Co_2MnO_4$ that has entirely $Co^{2+}$ is present as a single-phase in the quench system but not in the regular-cooled system.

At lower synthesis temperatures, $Li_{4/3}Mn_{5/3}O_4$, where all Mn has an oxidation state of +4, can be synthesized [12]. This composition does not exist in samples quenched from high temperatures, but could be present in slowly cooled samples (*i.e.* samples cooled at rates below roughly 1°C/min). From $x = 0$ to $x = 4/3$ in $Li_{4/3-x}Co_{2x}Mn_{5/3-x}O_4$ (curve B in Figure 3.5), the $Li^+$ and $Mn^{4+}$ are substituted with equal parts of $Co^{2+}$ and $Co^{3+}$. The resulting composition line is separate from the experimentally determined quenched cubic spinel region, but much of it falls within the spinel region of the regular-cooled phase diagram (compare Figure 3.5 to Figure 3.1 (b) or Figure 3.3 (b)).

## 3.3 Conclusions Regarding the Single-Phase Cubic Spinel Region of the Li-Co-Mn-O Pseudo-Ternary System

The cubic spinel single-phase region in the Li-Co-Mn-O pseudo-ternary system was explored by a solution-based combinatorial approach for two separate cooling rates. The results showed that the single-phase cubic spinel region in the quenched Li-Co-Mn oxide system extends diagonally from $Co_3O_4$ to $LiMn_2O_4$ and over to $Co_2MnO_4$. Cooling rate was shown to have a major influence on the shape and position of the single-phase cubic spinel region. The cubic spinel region for samples regular-cooled from 800°C in air experienced an overall shift toward the lithium corner when compared to the spinel region of samples quenched from 800°C in air. The boundary shift can be attributed to the higher oxygen uptake available to regular-cooled samples during synthesis such that structures with higher oxygen content (*i.e.* bixbyite $Mn_2O_3$) are favored.

Contour plots were constructed for the lattice constant of the cubic spinel region for both quenched and regular-cooled Li-Co-Mn-O pseudo-ternary phase diagrams. From the lattice constant contour plots, it was determined that the lattice grows in size as cobalt is replaced by a combination of lithium and manganese atoms from a minimum cubic lattice constant of $8.083 \pm 0.003$ Å for $Co_3O_4$ to a maximum of $8.243 \pm 0.001$ Å for $LiMn_2O_4$. There was no measureable difference between the two

cooling rates studied with regards to the measured lattice parameters of the $Co_3O_4$ and $LiMn_2O_4$ compositions.

Possible theoretical boundary lines to single-phase spinel region were determined from oxidation state considerations alone. The composition line from $x = 0$ to 1 in $Li_{1-x}Co_{2x}Mn_{2-x}O_4$ whereby $Li^+$ and $Mn^{3+}$ are being substituted with $Co^{2+}$ matched well with the top boundary of the quenched single-phase spinel region, but extended far above the corresponding regular-cooled data series. This result suggests that $Co^{2+}$ is more readily available in quenched samples than in regular-cooled samples, which allows for more diverse spinel compositions to exist as single-phase in the quenched system. Furthermore, the composition line from $x = 0$ to 1 in $Li_{1-x}Co_{3x}Mn_{2-2x}O_4$ whereby $Li^+$, $Mn^{3+}$, and $Mn^{4+}$ are being substituted with $Co^{2+}$ and $Co^{3+}$ matches well with the bottom boundary to the quenched spinel region.

# Chapter 4

# Combinatorial Studies of the Li-Ni-Mn-Co-O Pseudo-Quaternary System

## 4.1 Experimental Design

Figure 4.1 summarizes the regions of the Li-Ni-Mn-Co-O pseudo-quaternary phase system targeted by the current work. The red triangles highlight pseudo-ternary planes defined at the cobalt fractional metal contents of 10 %, 20 % and 30 % within the pseudo-quaternary system. These ternary planes will be referred to as 'cobalt slices' throughout this chapter. Additional factors have to be considered when investigating compositions within these cobalt slice systems compared to the pseudo-ternary systems defining the faces of the pseudo-quaternary system. Namely, tie-lines through the coexistence regions of the cobalt slices are able to extend out of the slice to higher or lower cobalt content phases, which makes the tie-lines difficult to visualize without 3-D plotting software. The main focus of the current work is to determine the single-phase regions existing within these cobalt slice systems since they are believed to contain interesting compositions for positive electrode materials research. The identity of the phases present in multiphase samples of these cobalt slice systems were not investigated in detail.

Figure 4.2 shows all targeted compositions within the cobalt slices of the Li-Ni-Mn-Co-O pseudo-quaternary system for both quenched and regular-cooled samples. Nearly 800 unique compositions were synthesized to map the phase regions of the 10 %, 20 %, and 30 % cobalt slice ternary phase diagrams within the Li-Ni-Mn-Co-O system using the methods described in Section 2.1. The cobalt slices shown in Figure 4.2 were initially mapped by 66 unique compositions spaced evenly across each ternary diagram and were subsequently mapped by a 'zoom-in' region that consisted of 66 compositions spaced evenly through a triangular region defined by vertices at relative (Ni, Mn) coordinates of (0.00, 0.70), (0.50, 0.20), and

**Figure 4.1:** Illustration of the cobalt slice ternary phase diagrams existing within the Li-Ni-Mn-Co-O pseudo-quaternary phase system that are discussed in this chapter. The pseudo-ternary planes of the phase diagram defined at 10 %, 20 % and 30 % cobalt content were mapped out using the described methods. The Li-Co edge and the non-Mn-containing axis of each pseudo-ternary plane are labeled in *red* and *blue* respectively and will be referenced later.
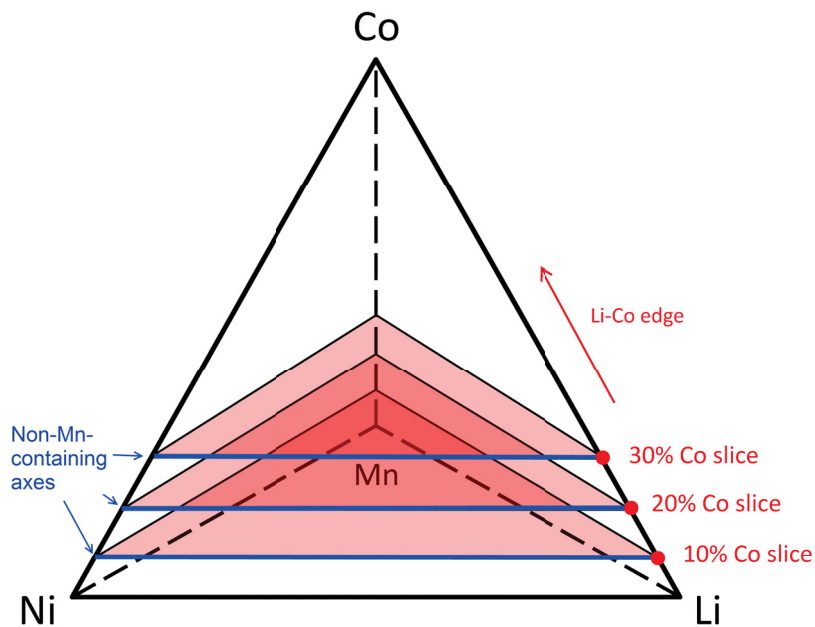
(0.00, 0.20) within each cobalt slice (*i.e.* the zoom-in regions were located at the same relative position in each cobalt slice, regardless of its cobalt content). Furthermore, the regular-cooled 10 % cobalt slice (shown in Figure 4.2 f) had two additional 'zoom-in' series prepared in order to closely investigate the single-phase cubic spinel and layered regions observed there.

Figure 4.3 shows the resulting series of cobalt slice phase diagrams corresponding to quenched samples and Figure 4.4 shows the resulting series of cobalt slice phase diagrams corresponding to regular-cooled samples in the Li-Ni-Mn-Co-O pseudo-quaternary system. It is not trivial to locate popular compositions in these diagrams. Figures 4.3 and 4.4 show the positions of the well-known industrial compositions $Li[Ni_{0.4}Mn_{0.4}Co_{0.2}]O_2$, $Li[Ni_{0.5}Mn_{0.3}Co_{0.2}]O_2$, $Li[Ni_{0.6}Mn_{0.2}Co_{0.2}]O_2$, and $Li[Ni_{0.2}Mn_{0.2}Co_{0.6}]O_2$ to provide context for the single-phase regions investigated. It is reassuring that these known single-phase samples fall within or very near the boundaries of the single-phase regions determined here. Evidence for the main features observed in the series of cobalt slice phase diagrams of Figures 4.3 and 4.4 will be presented in this chapter. Furthermore, the fitted lattice parameters for every observed single-phase material

within the cobalt slices have been cataloged by their dispensed fractional metal contents in Appendix A for reference.

## 4.2 Results of Elemental Analysis

Figure 4.5 shows ICP elemental analysis results for samples located near the Li-Co edge of the regular-cooled 10 % cobalt slice ternary phase diagram. The blue and green arrows in Figure 4.5 point from the initial compositions targeted during dispensing to the compositions measured after synthesis by ICP elemental analysis. These arrows tended to radiate away from the Li-Co edge and their magnitudes tended to decrease with lower initial lithium content. These observations support the results by McCalla who determined that lithium loss due to the formation of $Li_2O_2$ was a major factor that needed to be taken into consideration when synthesizing combinatorial samples in the lithium-rich region of the Li-Ni-Mn-Co-O system [8, 25]. The removal of lithium from a sample forces its composition away from the lithium corner of the pseudo-quaternary system (*e.g.* a sample initially dispensed at $Li_{0.70}Ni_{0.10}Mn_{0.10}Co_{0.10}$ that experiences 9 % lithium loss will have a resulting composition of $Li_{0.61}Ni_{0.13}Mn_{0.13}Co_{0.13}$). Thus, the final compositions of samples shown in Figure 4.5 have cobalt fractional metal contents higher than 10 % as shown. The highest measured cobalt fractional metal content in Figure 4.5 was $Co = 0.151 \pm 0.008$ for the sample dispensed at ($Ni = 0.081$, $Mn = 0.036$) and the average measured cobalt fractional metal content for samples dispensed inside or above the single-phase layered region was $Co = 0.104 \pm 0.001$. To be able to plot all compositions on the same ternary diagram, the measured compositions had their cobalt contents set to 10 % and the remaining 90 % was composed of Li, Ni, and Mn in the same ratio as was measured. As a result, the measured compositions are located at the same relative positions in the cobalt slice of Figure 4.5 as in their respective cobalt slice ternary phase diagrams.

The high cost per-sample of ICP elemental analysis prevented being able to measure the compositions of the majority of combinatorial samples prepared in the series outlined in Figure 4.2. However, the metal concentrations of all solutions used in sample dispensing were measured three separate times to obtain an error of 3 %,

**Figure 4.2:** Plots showing the compositions synthesized to map out the 10 %, 20 %, and 30 % cobalt slice ternary phase diagrams within the Li-Ni-Mn-Co-O pseudo-quaternary system. The targeted compositions for quenched samples are indicated by *blue dots* in (a), (c), and (e) and the targeted compositions for regular-cooled samples are indicated by *red dots* in (b), (d), (f). All samples were heated to 800°C for 3 h in oxygen before being cooled by the indicated cooling rate. The axes are labeled by their respective elements and their range of fractional metal content. The cobalt content of each pair of cobalt slices are: (a)-(b) 30 % cobalt content, (c)-(d) 20 % cobalt content, and (e)-(f) 10 % cobalt content. All synthesized samples were subsequently scanned by XRD and had their resulting patterns fitted using the methods explained in Section 2.4.

**Figure 4.3:** Stack of cobalt slice ternary phase diagrams in the Li-Ni-Mn-Co-O pseudo-quaternary system at cobalt contents of 0 %, 10 %, 20 %, and 30 % for samples quenched after heating to 800°C for 3 h in oxygen. The included Li-Ni-Mn-O pseudo-ternary phase diagram was determined by McCalla [9] and reprinted with permission from the American Chemical Society. The *red dots* in each phase diagram indicate compositions determined to be single-phase, *open blue dots* indicate samples containing two phases and *filled blue dots* indicate samples containing at least three distinct phases. The *solid red lines* define the boundaries to the single-phase regions as determined by dividing regions containing single-phase compositions with those containing multiphase. Common industrial compositions are labeled on the phase diagrams as follows: (A) Li[Ni$_{0.4}$Mn$_{0.4}$Co$_{0.2}$]O$_2$ in *black*, (B) Li[Ni$_{0.5}$Mn$_{0.3}$Co$_{0.2}$]O$_2$ in *green*, (C) Li[Ni$_{0.6}$Mn$_{0.2}$Co$_{0.2}$]O$_2$ in *purple*, and (D) Li[Ni$_{0.2}$Mn$_{0.2}$Co$_{0.6}$]O$_2$ in *orange*.

except for the solutions used to make the samples of Figure 4.5 that were only measured once to obtain an error of 5 %. Due to the high precision of the solutions-processing robot used to dispense every combinatorial sample, the 3 % error in metal concentration of the dispensing solutions is assumed to be the main source of error in the final compositions. Furthermore, since samples at higher initial lithium contents experience more lithium loss during heating [8, 25], samples
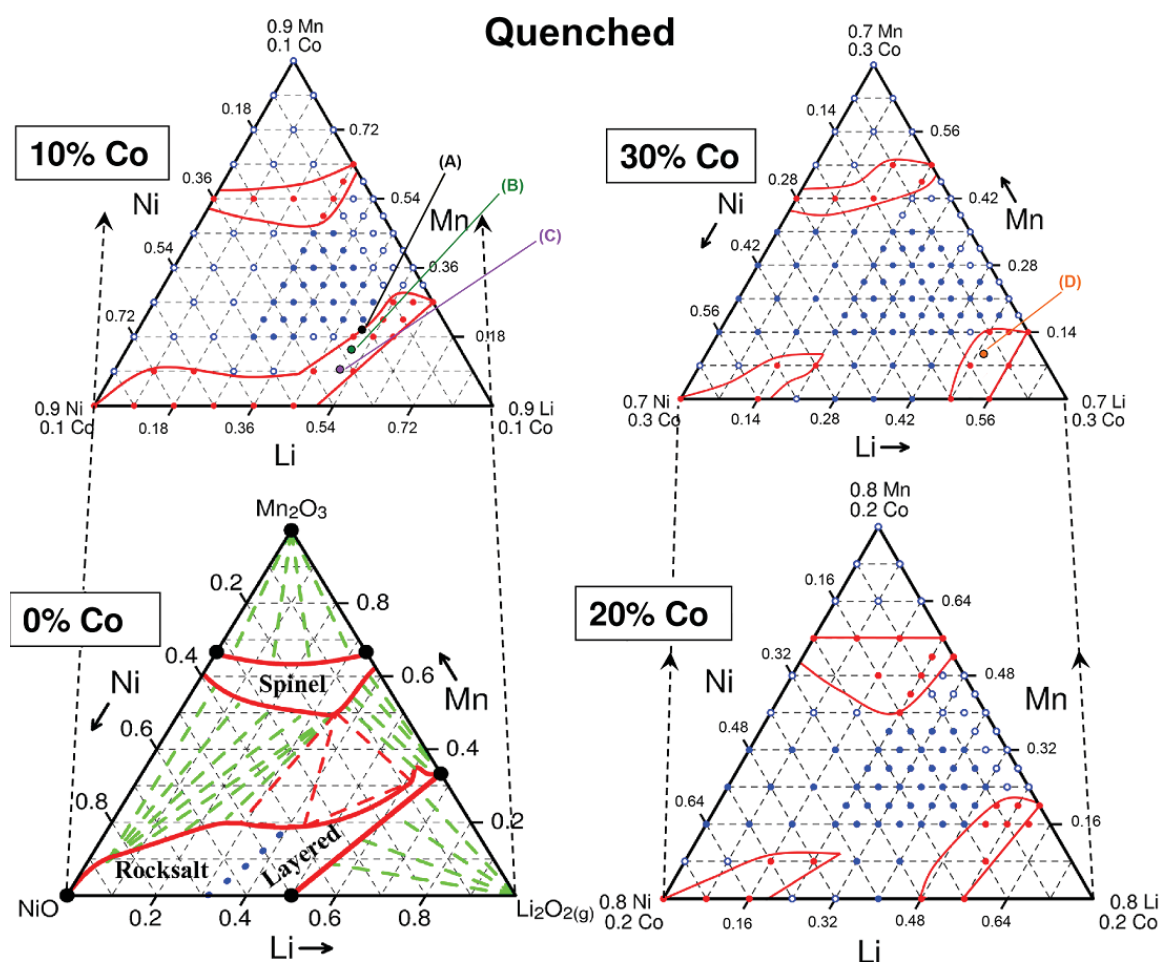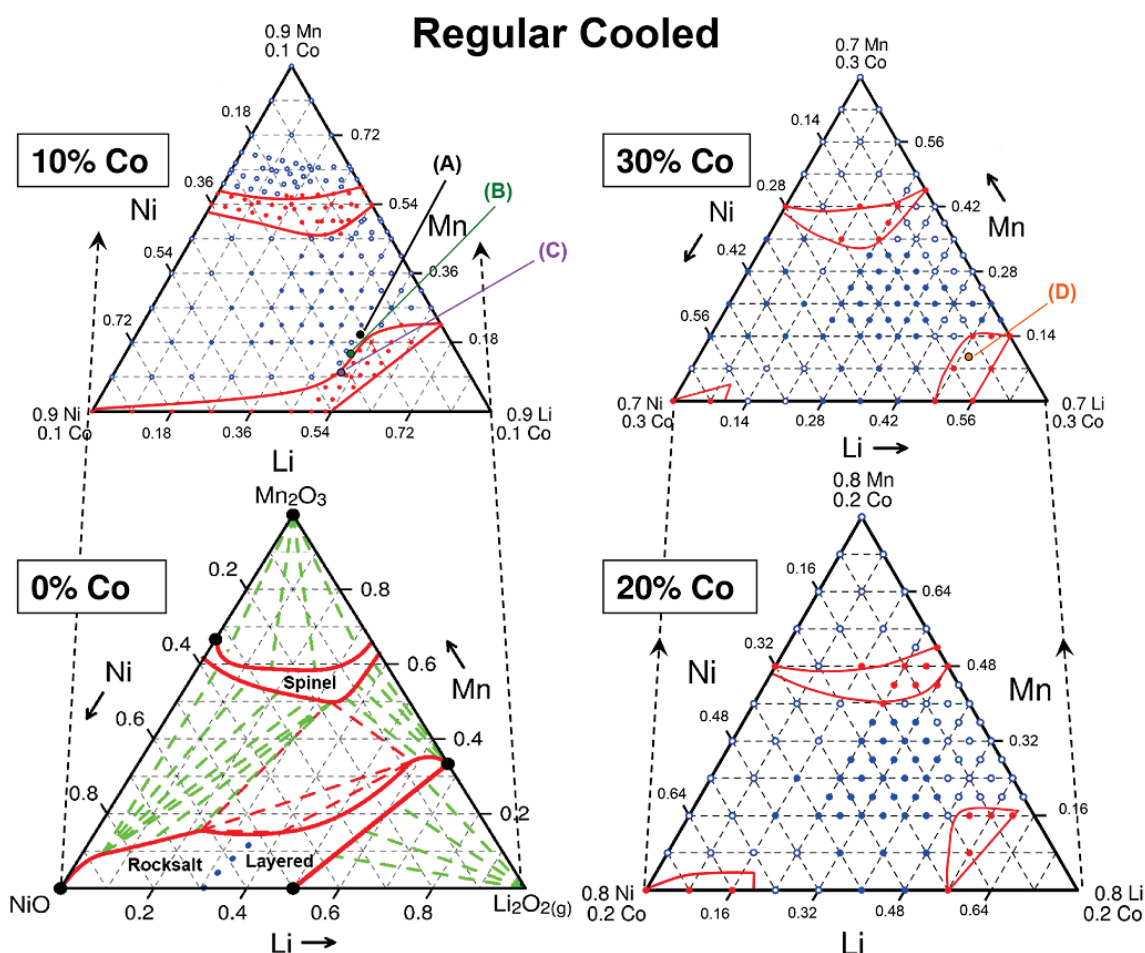
**Figure 4.4:** Stack of cobalt slice ternary phase diagrams in the Li-Ni-Mn-Co-O pseudo-quaternary system at cobalt contents of 0 %, 10 %, 20 %, and 30 % for samples regular-cooled after heating to 800°C for 3 h in oxygen. The included Li-Ni-Mn-O pseudo-ternary phase diagram was determined by McCalla [9] and reprinted with permission from the American Chemical Society. The *red dots* in each phase diagram indicate compositions determined to be single-phase, *open blue dots* indicate samples containing two phases and *filled blue dots* indicate samples containing at least three distinct phases. The *solid red lines* define the boundaries to the single-phase regions. Common industrial compositions are labeled on the phase diagrams as follows: (A) Li[Ni$_{0.4}$Mn$_{0.4}$Co$_{0.2}$]O$_2$ in *black*, (B) Li[Ni$_{0.5}$Mn$_{0.3}$Co$_{0.2}$]O$_2$ in *green*, (C) Li[Ni$_{0.6}$Mn$_{0.2}$Co$_{0.2}$]O$_2$ in *purple*, and (D) Li[Ni$_{0.2}$Mn$_{0.2}$Co$_{0.6}$]O$_2$ in *orange*.

dispensed at lower initial lithium contents than those shown in Figure 4.5 are expected to experience less amounts of lithium loss and, as a result, have more accurate final compositions. Thus, all compositions presented in this chapter, apart from those shown in Figure 4.5 and those that experience significant lithium loss in the region between the single-phase layered region and the Li-Co edge, are assumed to have final compositions accurate to approximately 3 % of their targeted compositions.
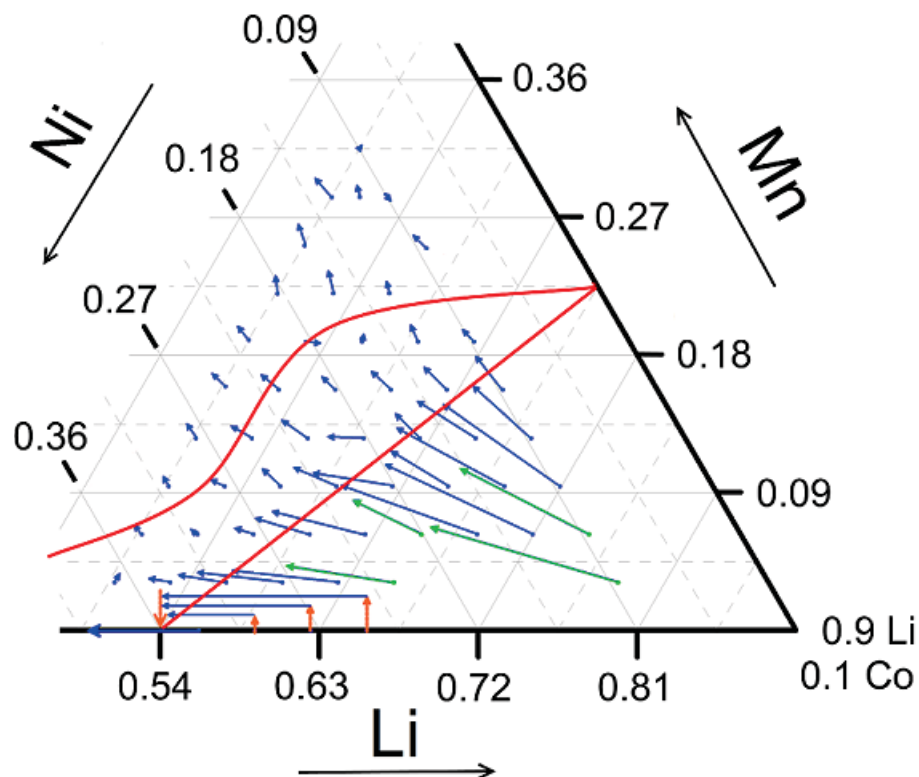
**Figure 4.5:** Plot of the elemental analysis results for samples with compositions located near the Li-Co edge of the 10 % cobalt slice ternary phase diagram within the Li-Ni-Mn-Co-O system. The samples shown were all heated to 800°C in oxygen before undergoing regular-cooling. The *blue* and *green arrows* point from the targeted compositions of samples to their final compositions after synthesis as measured by ICP elemental analysis. The samples represented by the green arrows will be referred to in the text. The ternary axes are labeled by their respective element. The *orange arrows* help distinguish the composition shifts occurring along the bottom axis. The *red lines* define the boundaries to the single-phase layered region as determined by the current study.

The effect of experimental error on compositional accuracy can be observed in the series shown in Figure 4.5 by the direction of the plotted arrows. If lithium loss were the only effect creating the observed difference in composition, the arrows in Figure 4.5 would be expected to diverge from the Li-Co edge. Although the majority of arrows in Figure 4.5 follow this ideal pattern fairly well, there are some that point in directions that indicate loss of metals other than lithium due to heating (*e.g.* the arrow representing the sample dispensed with the metal content $Li_{0.525}Ni_{0.185}Mn_{0.190}Co_{0.100}$ points away from the Ni corner, indicating a lower fractional nickel content in the final composition). As there are no mechanisms for such an effect to occur, this result is attributed to the error deriving from the ICP measurements and the concentrations of the dispensing solutions.
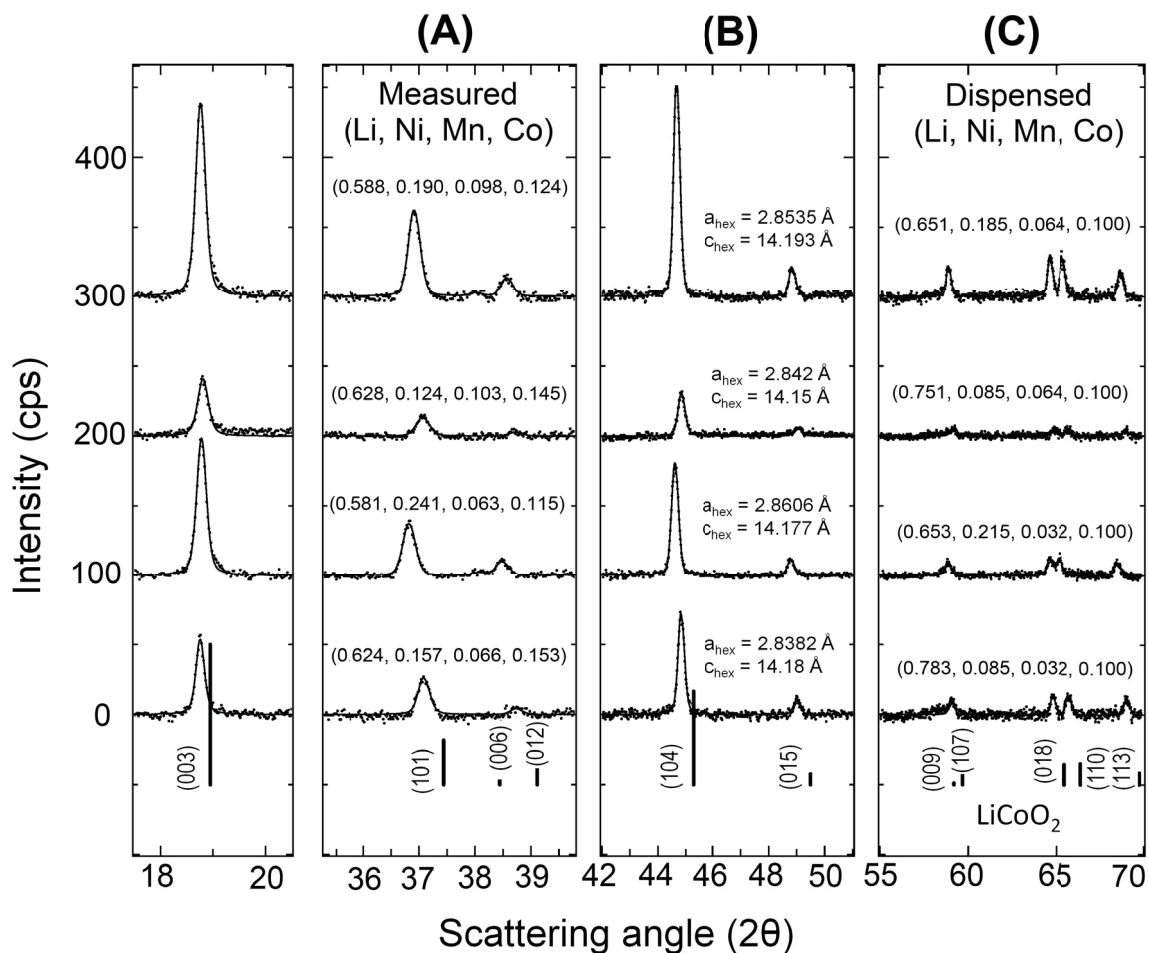
**Figure 4.6:** Stack of fitted XRD patterns for compositions dispensed near the Li-Co edge of the 10 % cobalt slice ternary phase diagram (green arrows in Figure 4.5). The measured compositions of each sample are provided in column (A) and the initial compositions are labeled in column (C). The fitted lattice parameters are reported in column (B). The XRD patterns are plotted as *black dots* and the resulting fits are drawn as *solid lines*. The *vertical lines* represent the database spectra for $LiCoO_2$ (JCPDS #77-1370) and each peak is labeled with its corresponding (hkl) index. The fits conclude that these samples single-phase layered materials.

Figure 4.6 shows the fitted XRD patterns for samples represented by green arrows in Figure 4.5. All XRD patterns shown in Figure 4.6 were fit as single-phase layered structures and the quality of the resulting fits indicate that the samples are single-phase layered materials. This result, in combination with the observations of Figure 4.5, suggests that the initial compositions of samples dispensed between the single-phase layered region and the Li-Co edge shift due to lithium loss such that the resulting compositions are within the single-phase layered region. The corresponding green arrows for these samples in Figure 4.5 do not extend to the single-phase layered region as drawn, however these samples were measured to have

cobalt fractional metal contents ranging from $0.130 \pm 0.007$ to $0.151 \pm 0.008$, which means their final compositions exist on a ternary between the 10 % and 20 % cobalt slice phase diagrams shown in Figure 4.4. As it will be demonstrated in the following section, the addition of cobalt forces the single-phase layered region to approach closer to the Li-Co edge and is expected to extend to the Li-Co edge of the 50 % cobalt ternary where $LiCoO_2$ is defined.

## 4.3 Layered and Rocksalt Single-phase Regions

Figure 4.3 shows the 10 %, 20 % and 30 % cobalt slice ternary phase diagrams for samples heated to 800°C under oxygen flow before being quenched to room temperature. Figure 4.4 shows an identical series of cobalt slice phase diagrams obtained for regular-cooled samples instead of quenched. As was true for the Li-Ni-Mn-O pseudo-ternary system, a large single-phase layered-rocksalt region was found to exist at compositions with low Mn content within the 10 % cobalt slice ternary systems for both quenched and regular-cooled samples. In the 20 % and 30 % cobalt slice ternary systems for both cooling rates, the single-phase layered-rocksalt region phase separated into distinct cubic rocksalt and hexagonal layered single-phase regions with a coexistence region existing between them.

Figure 4.7 shows XRD patterns for compositions extending across the lithium-rich portion of the single-phase layered region of the regular-cooled 10 % cobalt slice ternary phase diagram. The gradual shift in diffraction peak positions to higher angles between the XRD patterns of samples (A)-(G) in Figure 4.7 indicates the existence of a solid solution extending across the corresponding composition region. The samples corresponding to the endpoint XRD patterns of (A) and (G) in Figure 4.7 had structures resembling $LiNiO_2$ (JCPDS #89-3601) and $Li_2MnO_3$ (JCPDS #84-1634) respectively, with minor peak shifts to higher angles due to lower lattice parameters. The XRD pattern of sample 'A' in Figure 4.7, corresponding to a sample with measured fractional metal contents of $Li_{0.445}Ni_{0.450}Mn_{0.000}Co_{0.105}$, had fitted lattice parameters of $a_{hex} = 2.8719 \pm 0.0007$ Å and $c_{hex} = 14.194 \pm 0.008$ Å, which compared well with database values of $a_{hex} = 2.8762$ Å and $c_{hex} = 14.190$ Å for the nearby composition $LiNiO_2$. Sample 'G'
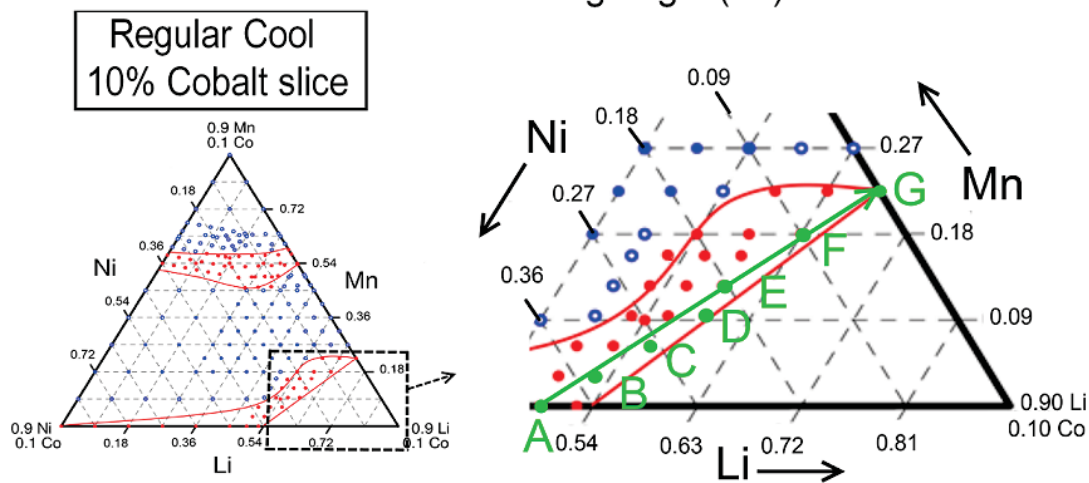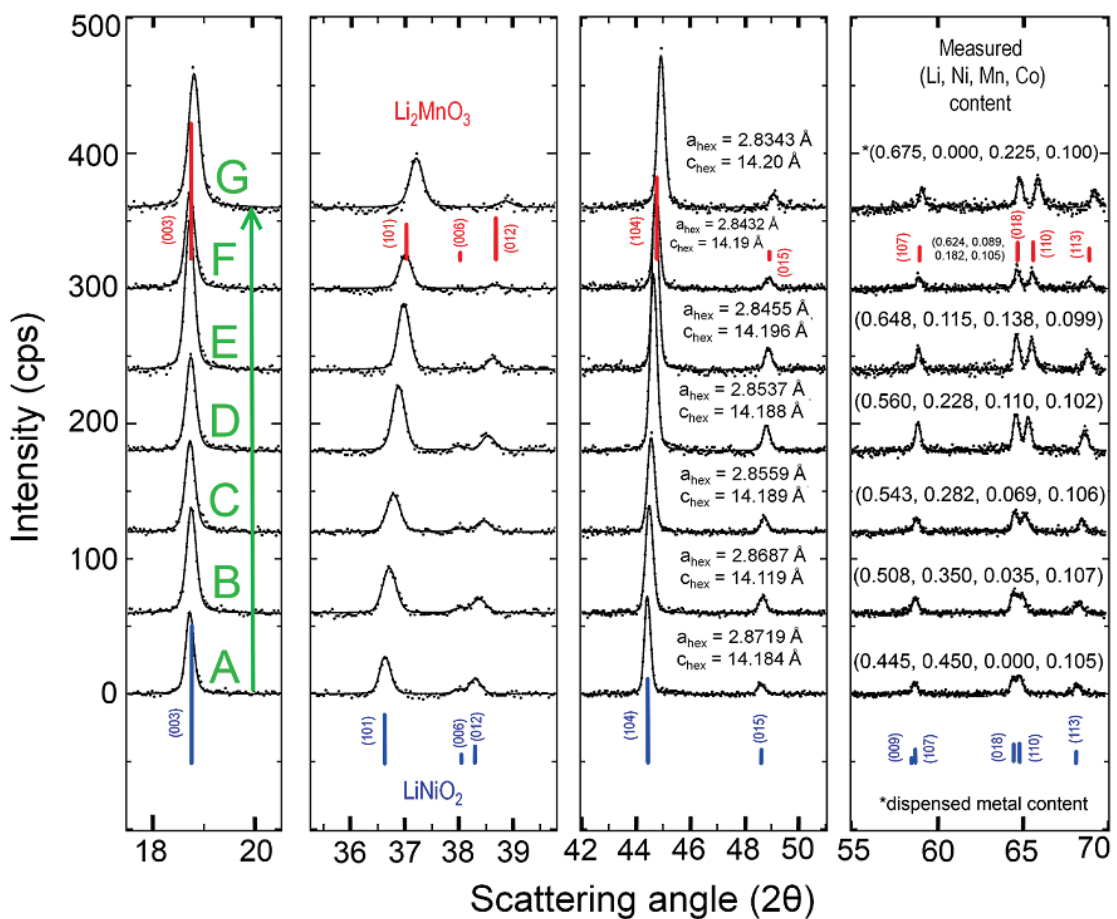
**Figure 4.7:** Stack of fitted XRD patterns for samples of the regular-cooled 10 % cobalt slice ternary system indicating the existence of a solid solution line through the single-phase layered region. Only every second data point is plotted within the XRD patterns in order to improve the clarity of their fits. The *blue* and *red vertical lines* represent the database spectra for LiNiO$_2$ (JCPDS #89-3601) and Li$_2$MnO$_3$ (JCPDS #84-1634) respectively and the corresponding (hkl) indices for each peak are labeled. The samples are labeled A through G and have their positions indicated on the included phase diagram. The (Li, Ni, Mn, Co) fractional metal contents for every sample as measured by ICP analysis are provided, except for sample 'G' which was not measured and instead has its dispensed composition reported. The lattice parameters retrieved from the fitted XRD patterns are reported in the third column of the XRD stack.

in Figure 4.7 did not have its final composition measured and was thus referred to by its dispensed fractional metal contents of $Li_{0.625}Ni_{0.000}Mn_{0.225}Co_{0.100}$. This sample had fitted lattice parameters of $a_{hex} = 2.8343 \pm 0.0004\,\text{Å}$ and $c_{hex} = 14.20 \pm 0.01\,\text{Å}$, which were slightly lower than the database values of $a_{hex} = 2.845\,\text{Å}$ and $c_{hex} = 14.2004\,\text{Å}$ for the nearby composition $Li_2MnO_3$.

The lower lattice parameters of samples A and G when compared to the database structures included in Figure 4.7 are likely the result of added cobalt content within their crystal structures. The Li-Co-Mn-O pseudo-ternary phase diagrams of the previous chapter suggest that the layered structure with the highest cobalt content is $LiCoO_2$, which has database lattice parameters of $a_{hex} = 2.815\,\text{Å}$ and $c_{hex} = 14.05\,\text{Å}$. Assuming that $LiCoO_2$ is the cobalt-rich endpoint composition of the single-phase layered region within the Li-Ni-Mn-Co-O pseudo-quaternary system, it is understandable that the lattice parameters of single-phase layered materials tend towards those of $LiCoO_2$ by decreasing when Ni and Mn atoms are replaced by Co atoms in the TM layers.

It is important to note the minor amount of peak broadening occurring in the XRD pattern of sample 'G' in Figure 4.7 that could be indicative of phase separation between two distinct layered phases beginning to occur [8, 18]. The results by McCalla on the layered solid solution line in the Li-Co-Mn-O pseudo-ternary system determined that samples prepared there with Co fractional metal contents ranging from 0.12 to 0.28 (see Figure 3.1 b) phase separated to have two distinct hexagonal layered phases when regular-cooled [8, 18]. As the composition of sample 'G' was not measured, the final cobalt content can only be extrapolated from the results of the previous section which observed an average cobalt content of $Co = 0.104 \pm 0.001$ for regular-cooled samples dispensed within the single-phase layered region. Thus, unless the cobalt content of sample 'G' was artificially higher due to experimental error, it is expected that the observed broadening effects were due to a smaller crystallite size and not a layered-layered phase separation.

Figure 4.8 shows three stacks of XRD patterns corresponding to samples synthesized along the non-Mn-containing axis of each cobalt slice ternary phase diagram (*i.e.* the portions of cobalt slices existing on the Li-Ni-Co face of the
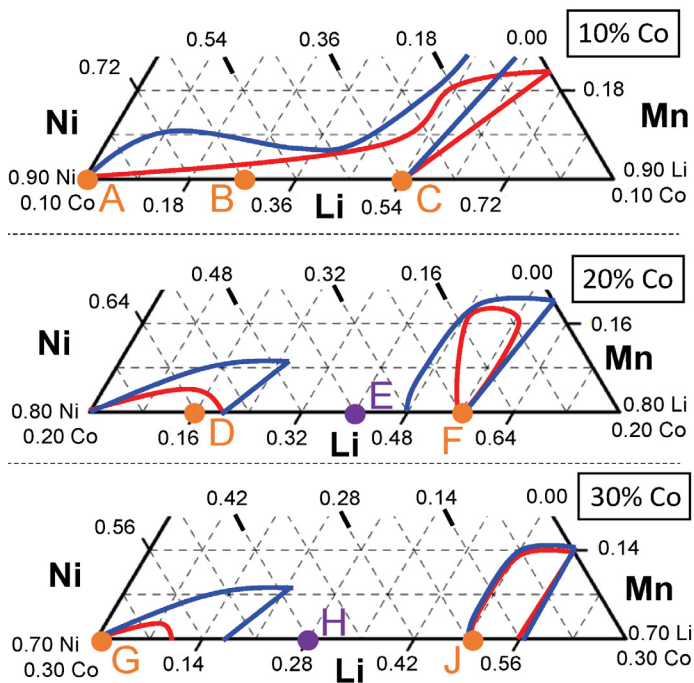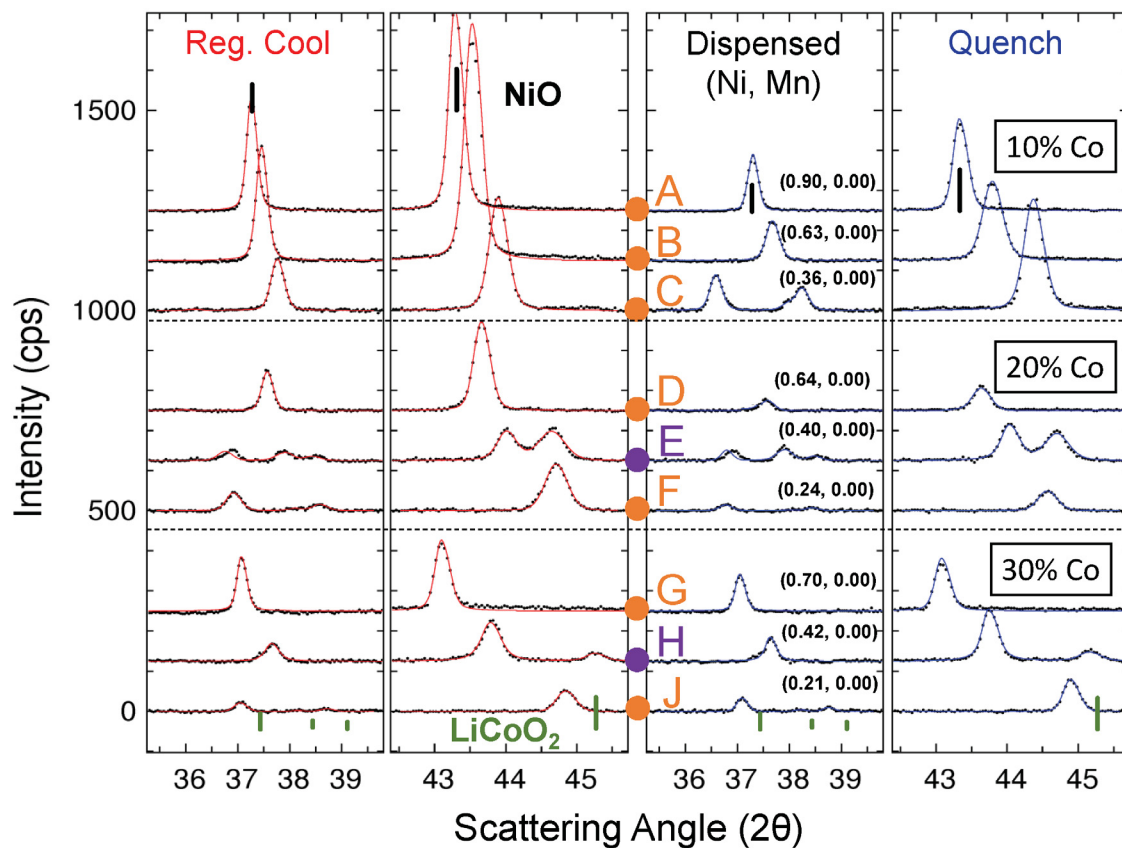
**Figure 4.8:** Stacks of fitted XRD patterns for samples synthesized along the non-Mn-containing axis of each cobalt slice ternary phase diagram. Regular-cooled XRD patterns and single-phase boundary lines are drawn in *red* and quenched in *blue*. Dispensed (Ni, Mn) contents of samples are provided and corresponding locations on the phase diagram are indicated by *orange* and *purple dots* for single-phase and multiphase respectively. All fitted peaks were indexed by the R-3m spacegroup for hexagonal structures and multiphase fits had two sets of peaks indexed. The *black* and *green vertical lines* correspond to the database spectra for NiO (JCPDS #44-1159) and LiCoO₂ (JCPDS #77-1370).

pseudo-quaternary system as shown in Figure 4.1). The relevant regions of the cobalt slice ternary phase diagrams are included in Figure 4.8 with the single-phase boundaries drawn for both cooling rates as determined by separating single-phase compositions from multiphase. The cubic rocksalt single-phase region was observed to be smaller for regular-cooled samples than for quenched samples, which is to be expected since the rocksalt structure is more stable at high temperatures. The quenching process essentially freezes the high temperature structure of the sample to room temperature, which allows for a wider range of single-phase rocksalt compositions to exist in quenched samples. Regular-cooled samples allow for a longer period of time for their structures to relax and atoms to rearrange during cooling, which favors the formation of extra phases. These comparisons help explain the observation of the single-phase cubic rocksalt region being larger for quenched samples than for regular-cooled samples within each cobalt slice ternary system, as seen in Figure 4.8.

The hexagonal layered single-phase region had similar observed size differences between quenched and regular-cooled samples in the 10 %, 20 % and 30 % cobalt slice ternary systems. As is shown in Figure 4.8, the hexagonal layered region of the regular-cooled 20 % cobalt slice ternary system did not fully extend to the Li-Co-Mn face of the pseudo-quaternary phase system. The regular-cooled sample dispensed at the composition $Li_{0.60}Ni_{0.00}Mn_{0.20}Co_{0.20}$ on the non-Ni-containing axis of the 20 % cobalt slice was determined to be a layered-layered phase separated material. This observation corroborates the results by McCalla regarding layered-layered phase separation occurring in regular-cooled layered materials of the Li-Co-Mn-O pseudo-ternary system with Co fractional metal contents ranging from 0.12 to 0.28 [8, 18].

Although the samples corresponding to XRD patterns plotted in Figure 4.8 are labeled by their dispensed fractional metal contents and not measured contents, the effects of lithium loss on the XRD patterns can be observed by comparing the data between the two cooling rates. A dramatic example of this is observed in the pair of XRD scans corresponding to a quenched and a regular-cooled sample dispensed with fractional metal contents of $Li_{0.45}Ni_{0.45}Mn_{0.00}Co_{0.100}$ (label C in Figure 4.8). The structure of the quenched sample at this composition was determined to be a

single-phase hexagonal layered, while the corresponding regular-cooled sample had its structure determined to be single-phase cubic rocksalt due to having a $c/a$ ratio of $4.91 \pm 0.02$, which is within error of the value $\sqrt{24}$ expected for cubic rocksalt structures.

The different phases observed in samples of composition 'C' of Figure 4.8 between different cooling rates implies that either the regular-cooled sample contained a higher nickel fractional metal content following synthesis than the quenched sample, which would allow for the formation of a rocksalt phase during cooling, or that the rocksalt phase is preferred at this composition for samples cooled more slowly. The difference in nickel content from the first implication may be the result of the different lithium losses experienced between regular-cooled and quenched samples. Since regular-cooled samples are heated for a longer period of time than quenched samples (albeit at an average lower temperature due to the slower cooling rate), the lithium within regular-cooled samples is given more time to 'evaporate' via the formation of $Li_2O_2$. Thus, a regular-cooled sample should be expected to experience slightly more lithium loss than a corresponding quenched sample. Furthermore, the uncertainty of metal concentrations in the different dispensing solutions used to make these samples may have resulted in excess nickel being present in the regular-cooled sample of composition 'C' compared to the corresponding quenched sample. The second implication is difficult to prove without measuring and comparing the final metal contents of the quenched and regular-cooled samples following their synthesis. If they were found to have identical values, then it would be likely that the phase difference observed between the regular-cooled and quenched samples of composition 'C' was the result of the rocksalt structure being favored for slower cooling rates.

Samples made at compositions 'E' and 'H' labeled in Figure 4.8 had their XRD patterns calculated with two sets of diffraction peaks indexed by the R-3m spacegroup for hexagonal layered structures. The resulting fitted XRD patterns determined that these compositions phase separated into distinct layered and rocksalt phases, and sample 'E' had an additional third phase that was not identified. The unfitted data seen within the XRD patterns of the regular-cooled and quenched samples of composition 'E' in Figure 4.8 is indicative of the unfitted

third phase present in these samples. It is difficult to conclude the identity of the third phase without performing a three-phase fit, which was not done as it is beyond the scope of the current work. Interestingly, the fitted multiphase XRD patterns shown in Figure 4.8 had little variation between quenched and regular-cooled samples of the same composition, which is contrasted by the significant differences observed between the XRD patterns of quenched and regular-cooled single-phase samples. This suggests that these multiphase compositions are composed of very similar phases regardless of cooling rate. As there was no Mn present in any of the samples shown in Figure 4.8, these samples exist on the Li-Ni-Co face of the pseudo-quaternary system. Therefore, there must exist a three-phase region within the Li-Ni-Co-O pseudo-ternary system. It would be interesting to further investigate the Li-Ni-Co-O pseudo-ternary system in the future in order to understand the structure of the single-phase and coexistence regions existing there.

## 4.4   Single-phase Cubic Spinel Region

Figure 4.9 shows stacks of XRD patterns corresponding to samples (A)-(I) of compositions with constant manganese content across the single-phase cubic spinel region of the 10 %, 20 %, and 30 % cobalt slice ternary phase diagrams. The relevant region of the corresponding phase diagrams are included in Figure 4.9 with the single-phase boundaries drawn for both cooling rates as determined by separating single-phase compositions from multiphase. The fitted XRD patterns in Figure 4.9 were determined by having diffraction peaks indexed by the Fd-3m spacegroup for cubic structures. Multiphase samples in Figure 4.9 are identified by the presence of unfitted diffraction peaks remaining in the fitted XRD patterns. A separate two-phase fitting was performed on such samples to confirm the identity of the extra phase. For example, the XRD pattern labeled 'F' in Figure 4.9 corresponding to the quenched sample of dispensed fractional metal contents $Li_{0.12}Ni_{0.00}Mn_{0.48}Co_{0.20}$ had an unfitted peak near $2\theta = 44.8°$, which was determined to be the (104) peak of a hexagonal layered phase through two-phase fitting.

It is important to note that Figure 4.9 is not a complete survey of all the single-phase compositions found to exist within the single-phase cubic spinel regions
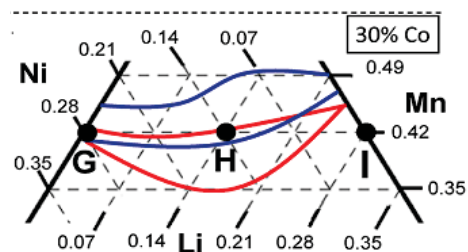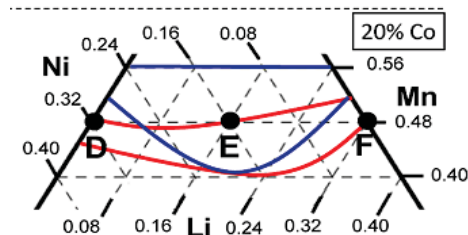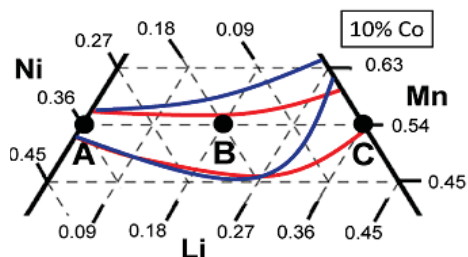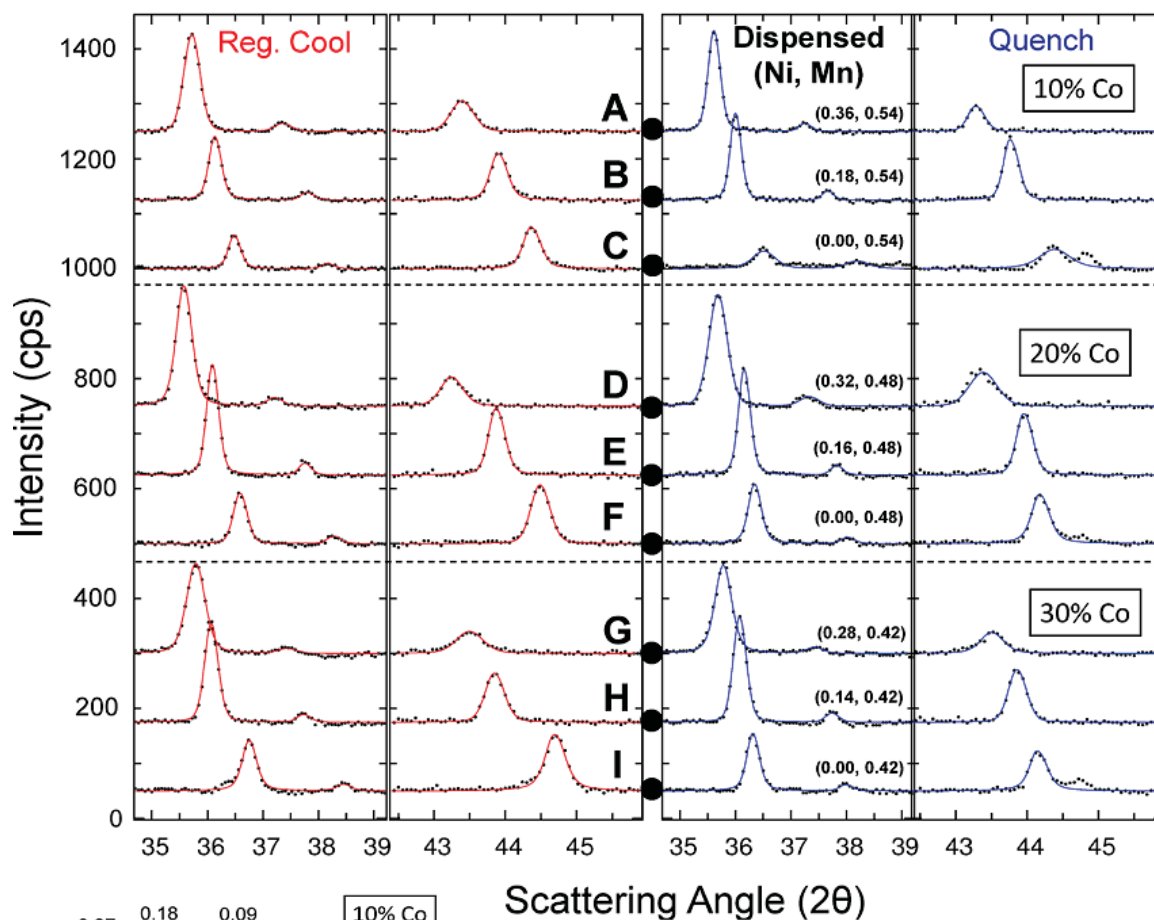
**Figure 4.9:** Stacks of fitted XRD patterns for samples synthesized at constant manganese content through the single-phase cubic spinel region of each cobalt slice ternary phase diagram. Regular-cooled XRD patterns and single-phase boundary lines are drawn in *red* and quenched in *blue*. Dispensed (Ni, Mn) contents of samples are provided and their corresponding locations on the phase diagram are highlighted by the labels (A)-(I). All fitted peaks were indexed by the Fd-3m spacegroup for cubic structures.

of the cobalt slice ternary phase diagrams. The intended purposes of Figure 4.9 are to demonstrate how the single-phase cubic spinel boundaries presented in Figures 4.3 and 4.4 were determined and also to demonstrate the effect of cooling rate on the position of the single-phase boundaries. All single-phase compositions used to determine the boundaries to the single-phase regions in the cobalt slice ternary systems have been cataloged in Appendix A along with their corresponding fitted lattice parameters.

The portions of the cobalt slice ternary phase diagrams included in Figure 4.9 show the determined single-phase spinel regions for both quenched and regular-cooled samples. The upper and lower boundaries of the regular-cooled single-phase spinel regions were found to exist at compositions of lower Mn content compared to the corresponding quenched regions. This result is consistent with observations in the Li-Co-Mn-O pseudo-ternary system from the previous chapter and also the work by McCalla on the Li-Ni-Mn-O pseudo-ternary system [8, 9]. The reasoning for the observed shift resulting from different cooling rates is likely related to the differences in oxygen content between quenched and regular-cooled samples. Phases with high manganese content, such as bixbyite (including $Mn_2O_3$) and tetragonal spinel (including $Mn_3O_4$), form more easily in materials with higher available oxygen content. Since combinatorial samples lose significant amounts of oxygen during heating due to a high surface-area-to-volume ratio, their structure will be oxygen deficient unless they are cooled slowly to allow for oxygen uptake. Regular-cooled samples should thus have a higher oxygen content than quenched samples. With more oxygen available to form the oxide structures in regular-cooled samples, it would be more likely that they contain tetragonal spinel or bixbyite phases at dispensed Mn fractional contents where corresponding quenched samples were determined to be single-phase. This would explain the observation where the multiphase regions located above the regular-cooled single-phase spinel regions were larger than in the corresponding quenched systems, as can be seen by comparing the cobalt slices of Figure 4.3 with those of Figure 4.4.

The diffraction peaks of samples shown in Figure 4.9 all shifted to lower values of $2\theta$ when replacing Li with Ni in their compositions (*i.e.* samples from right to left across each phase diagram in Figure 4.9). The observed peak shifts corresponded to

an increase in lattice parameter due to the replacement of Li atoms by Ni atoms at octahedral sites within the spinel structure. In the regular-cooled $10\%$ cobalt slice ternary system, the observed spinel solid solution extending from the fractional metal contents of $Li_{0.36}Ni_{0.00}Mn_{0.54}Co_{0.10}$ (composition 'C' in Figure 4.9) to $Li_{0.00}Ni_{0.36}Mn_{0.54}Co_{0.10}$ (composition 'A' in Figure 4.9) had measured lattice parameters of $a_{cub} = 8.153 \pm 0.002$ Å and $a_{cub} = 8.354 \pm 0.002$ Å respectively at these endpoint compositions. For the corresponding quenched samples, the lattice parameters of the spinel phase were measured to be $a_{cub} = 8.164 \pm 0.007$ Å and $a_{cub} = 8.356 \pm 0.002$ Å respectively. However, the quenched sample of composition 'C' in Figure 4.9 was not single-phase as determined by the unfitted (104) hexagonal layered peak remaining near $2\theta = 44.8°$ in the fitted XRD pattern of the sample. The lattice parameters for samples of the Ni-rich endpoint composition $Li_{0.00}Ni_{0.36}Mn_{0.54}Co_{0.10}$ (composition 'A' in Figure 4.9) are lower than the lattice parameter of $a_{cub} = 8.4028$ Å for the nearby composition $NiMn_2O_4$ for both cooling rates, which is to be expected since the addition of cobalt tends to decrease lattice parameter.

At $20\%$ and $30\%$ cobalt fractional metal content, the lattice parameters of the spinel phase in the compositions of Figure 4.9 tended to decrease until reaching a minimum value of $a_{cub} = 8.099 \pm 0.002$ Å in the regular-cooled sample of composition 'I' dispensed at fraction metal content $Li_{0.08}Ni_{0.00}Mn_{0.42}Co_{0.30}$. This composition exists within the spinel-layered coexistence region of the Li-Co-Mn-O pseudo-ternary system and is expected to tie to a cobalt-rich spinel phase in the vicinity of the cobalt corner. The $Co_3O_4$ spinel phase is the endpoint cobalt composition within the single-phase spinel region of the Li-Ni-Mn-Co-O pseudo-quaternary system and it has a lattice parameter of $a_{cub} = 8.084 \pm 0.004$ Å as reported in the previous chapter. Since the lattice parameter of the spinel phase in the regular-cooled sample of composition 'I' was close to the value of $Co_3O_4$, it matches the results predicted by the phase diagrams of the previous chapter.

It is expected that increasing the cobalt content of cubic spinel materials will decrease their lattice parameter. The fitted lattice parameters reported in Figure 4.9 followed this expected pattern, as the lowest lattice parameters were measured for samples dispensed at the highest Co fraction metal content of 0.30. This result
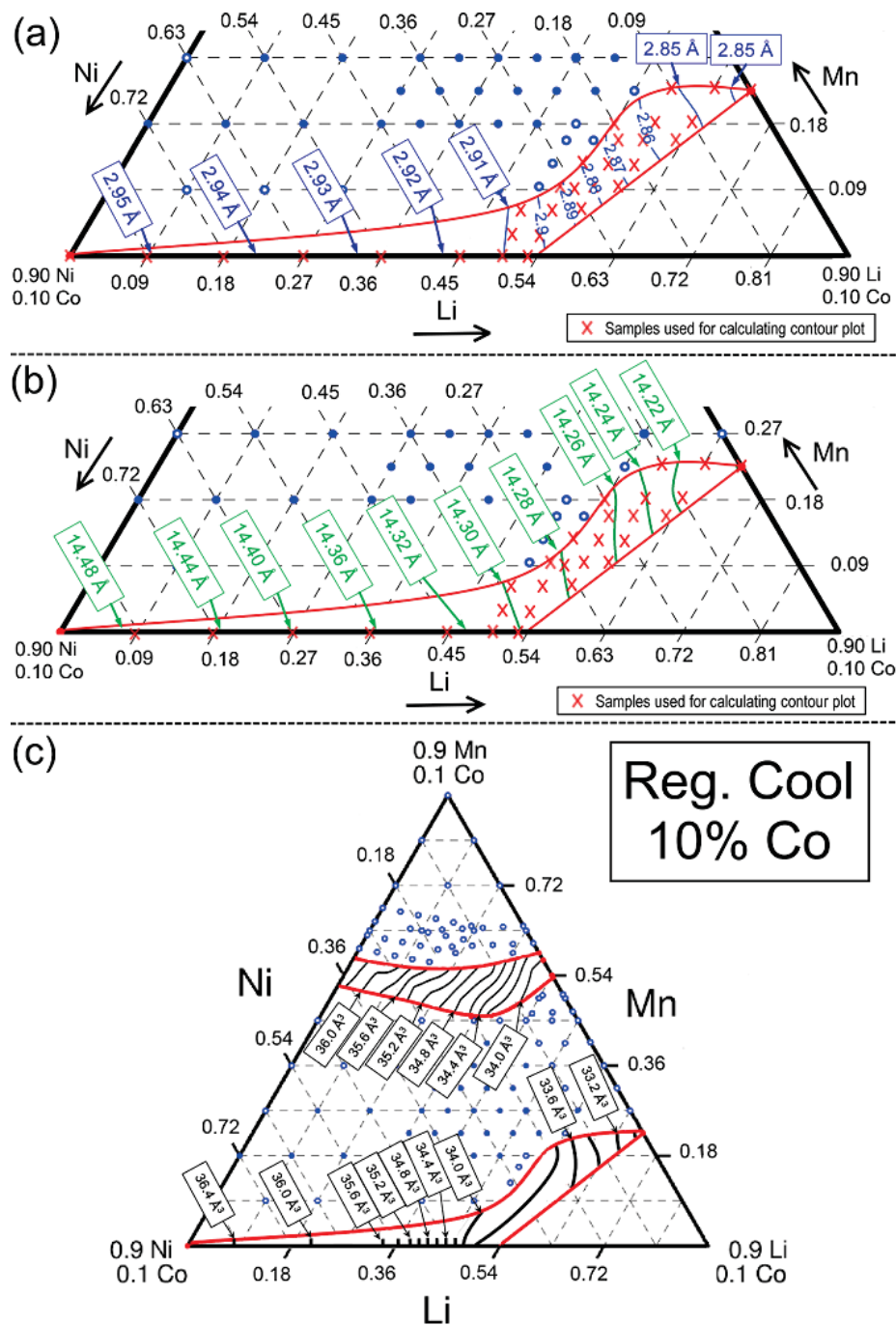
**Figure 4.10:** Contour plots of the (a) fitted $a_{hex}$ lattice parameters, (b) fitted $c_{hex}$ lattice parameters of the single-phase layered region in the regular-cooled 10 % cobalt slice ternary phase diagram and (c) contour plots of unit cell volume per $MO_2$ basis unit for both the cubic spinel and layered single-phase regions within the regular-cooled 10 % cobalt slice. To determine the contour plots in (c), unit cell volumes determined for both single-phase regions from fitted lattice parameters were divided by the number of metal atoms in octahedral sites for each structure. The number divided by was 16 for the cubic spinel structure ($M_3O_4$ in Fd-3m spacegroup) and 3 for the hexagonal layered structure ($LiMO_2$ in R-3m spacegroup).

suggests that the cobalt content of a spinel phase in a multiphase sample within the Li-Ni-Mn-Co-O pseudo-ternary system could potentially be characterized by its lattice parameter (*e.g.* a lower cubic lattice parameter means higher cobalt content and vice versa). A full survey of the pseudo-quaternary system would be required in order to accurately determine the structure of tie-lines and describe how the single-phase spinel and layered regions connect through their coexistence regions.

Figure 4.10 shows contour plots of the fitted lattice parameters for compositions within the single-phase layered region of the regular-cooled 10 % cobalt slice ternary system, in addition to a contour plot of unit cell volume per $MO_2$ basis unit for both the cubic spinel and hexagonal layered regions of the same system. The contour plots of $MO_2$ unit volume were determined using the fitted lattice parameters of each individual composition, which were then divided by either 16 for spinel structures or 3 for layered structures, as was determined in Section 2.7 from crystal structure considerations. Two major observations can be obtained from Figure 4.10 (c), the first of which is the influence of Li on the $MO_2$ unit volume, and the second is the large change in $MO_2$ volume occurring in the vicinity of the expected rocksalt-layered phase transition.

Both the spinel and layered regions of Figure 4.10 (c) experienced a decrease in $MO_2$ unit volume as lithium replaced either Ni or Mn within either structure. Furthermore, it appeared that there was little effect on the volume from replacing Ni with Mn or vice versa, as indicated by the tendency of the contour lines in Figure 4.10 to run parallel with grid lines of constant Li content. The layered contour plots in Figure 4.10 (a)-(c) had no single-phase samples dispensed above the Li-Ni-Co edge from Li = 0.00 to Li = 0.50. Thus, the contour lines in Figure 4.10 along the Li-Ni-Co edge are expected to only be accurate along the edge as drawn and should not be extrapolated to areas where no samples were prepared.

The location of the phase transition between the rocksalt and layered phases was not determined for either the quenched or regular-cooled 10 % cobalt slice ternary. However, the existence of such a phase transition is highly likely as there were no rocksalt-layered multiphase samples observed along the Li-Ni-Co edge of this system. Since the structures must change from one to the other at some composition, there must be either a phase transition line or a small coexistence

region existing between the compositions observed. Along the bottom axis of the contour plot shown in Figure 4.10 (c) between the values of Li$=0.36$ to Li$=0.50$, there was a higher density of contour lines that corresponded to a large change in the MO$_2$ unit volume. This change in volume is likely related to the phase transition occurring between the rocksalt and layered phases due to the rocksalt phase having a larger unit cell than the hexagonal layered phase. Thus, the phase transition line between the rocksalt and layered phases in the regular-cooled 10 % cobalt slice is expected to exist somewhere between Li$=0.36$ and Li$=0.50$ on the Li-Ni-Co edge.

## 4.5 Layered-Spinel Coexistence Region

The focus of the current work on the Li-Ni-Mn-Co-O pseudo-quaternary system was to investigate the structure of single-phase regions in order to better understand the compositions available to potentially discover new cathode materials. It would also be useful to understand of the coexistence regions existing between the spinel and layered-rocksalt single-phase regions of the system for research on composite positive electrode materials, but a careful understanding of this is beyond the scope of the current work. The spinel-layered coexistence regions of the Li-Ni-Mn-Co-O pseudo-ternary system are represented in Figures 4.3 and 4.4 by the empty and filled blue circles between the spinel and layered regions of each cobalt slice ternary which correspond to samples containing either two or at least three separate phases respectively. The multiphase samples of this work were all fit by a two-phase fitting routine with peaks indexed by either a combination of one cubic spinel and one hexagonal layered structure or two hexagonal layered structures. Many of the multiphase samples found in these regions contained more than two phases as was indicated by unfitted XRD data remaining in their fitted patterns. Determining the tie-lines within the coexistence regions of the Li-Ni-Mn-Co-O pseudo-quaternary system is a highly complicated task which requires a full survey of the system and thus requires more work. This section will discuss results which demonstrate the difficulty of determining tie-lines in these multiphase regions. Furthermore, results found to corroborate observations by McCalla in the coexistence regions of the Li-Ni-Mn-O pseudo-ternary system [8, 9] will be discussed. Specifically, evidence for

the existence of separate spinel-layered and spinel-rocksalt coexistence regions within the quenched 20 % cobalt slice of the Li-Ni-Mn-Co-O pseudo-quaternary system will be shown.

Figure 4.11 shows a stack of fitted XRD patterns corresponding to quenched samples in the 20 % cobalt slice ternary system with compositions highlighted on the included phase diagram. The XRD pattern labeled '2' was fit as single-phase cubic spinel, while the patterns labeled '1' and '3' were fit as a combination of cubic spinel and hexagonal layered structures. The $c/a$ ratio of the hexagonal layered fitted parameters of sample '3' was calculated to be $4.90 \pm 0.01$, which is within error of the value $\sqrt{24}$ expected for parameters corresponding to a cubic rocksalt structure. The fitted XRD pattern of sample '1' was found to contain a hexagonal layered phase in combination with a cubic spinel phase. These results suggest that there are at least two separate coexistence regions existing within the multiphase region of the Li-Ni-Mn-Co-O pseudo-quaternary system: a spinel-rocksalt coexistence region and a spinel-layered coexistence region. This result is very similar to the results found by McCalla regarding the coexistence region of the Li-Ni-Mn-O pseudo-ternary system wherein tie-lines were defined by 'RSNM' phase materials. However, determining the tie-lines for multiphase materials within the cobalt slices is a far more difficult task due to the possibility for the constituent phases of multiphase samples to have different cobalt contents. This means that the constituent phases of a sample may exist out of plane from the original cobalt slice ternary in which it was dispensed, which adds considerable difficulty to the task of determining the tie-lines.

The cubic spinel phase of the multiphase samples in Figure 4.11 were found to have lattice parameters of $a_{cub} = 8.194 \pm 0.002\,\text{Å}$ and $a_{cub} = 8.237 \pm 0.002\,\text{Å}$ for compositions labeled '1' and '3' respectively, while the single-phase composition labeled '2' had a lattice parameter of $a_{cub} = 8.206 \pm 0.002\,\text{Å}$. The results of the previous section showed that the lattice parameter of single-phase spinel materials increased with nickel content, but also decreased with increased cobalt content. This makes it is difficult to determine the compositions of the spinel phases in samples '1' and '3' from their cubic lattice parameters alone, since there are two variables influencing the value of the measured lattice parameters. However, since the fitted lattice parameters of the spinel phases in samples '1' and '3' were

**Figure 4.11:** Stack of fitted XRD patterns corresponding to quenched samples of compositions near the lower boundary to the single-phase spinel region in the 20 % cobalt slice. The dispensed (Ni, Mn) fractional metal contents of each sample are given and their corresponding locations are highlighted on the phase diagram in *orange*. Samples '1' and '3' had their XRD patterns calculated using two sets of peaks indexed by cubic spinel and hexagonal layered structures, while the XRD pattern of sample '2' was calculated using peaks only indexed as cubic spinel. The *green* and *red vertical lines* represent the database (104) peak of NiO (JCPDS #44-1159) and $Li_2MnO_3$ (JCPDS #84-1634) respectively. The difference between the calculated XRD pattern and the measured data are represented by the *solid black line* under each fit.
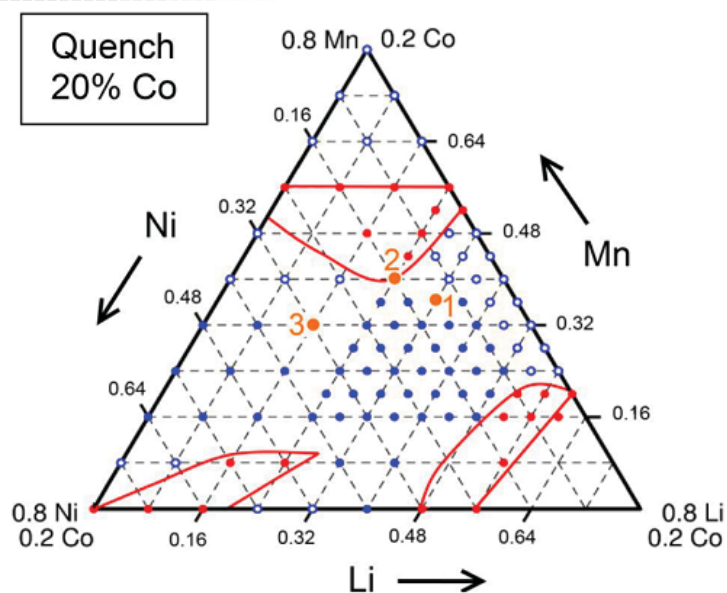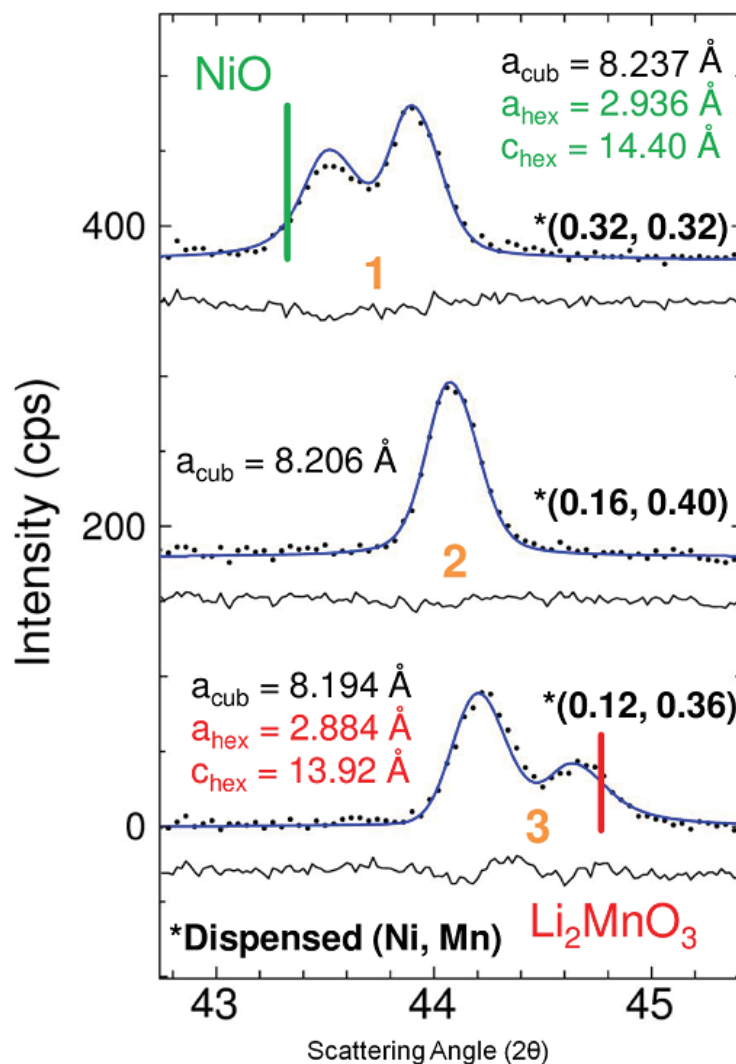
reasonably close to the single-phase material '2', it is likely that their compositions were in close proximity with one another. To accurately determine compositions of these constituent phases, the remainder of the Li-Ni-Mn-Co-O pseudo-quaternary system would have to be mapped in order to obtain a full survey of the lattice parameters of single-phase compositions available to form in the multiphase materials of this system.

## 4.6   Conclusions Regarding Combinatorial Studies of Li-Ni-Mn-Co-O Materials

The cubic spinel and layered-rocksalt single-phase regions of the 10 %, 20 %, and 30 % cobalt slice ternaries of the Li-Ni-Mn-Co-O pseudo-quaternary system were determined for quenched and regular-cooled samples. The fitted lattice parameters of the single-phase materials observed in these systems have been cataloged in Appendix A for future reference. The effects of lithium loss during heating were studied through a series of ICP elemental analysis measurements on samples synthesized within the lithium-rich region of the regular-cooled 10 % cobalt slice ternary. Samples dispensed within the single-phase layered region experienced an average lithium loss of roughly 1 %. Lithium loss was found to be most severe in samples dispensed in the region between the single-phase layered region and the Li-Co edge of the pseudo-quaternary system. The lithium loss experienced by such samples caused their final composition to exist within the single-phase layered region.

The rocksalt-layered single-phase region of the pseudo-quaternary system was found to phase separate at some cobalt fractional metal content between 10 % and 20 % for both quenched and regular-cooled samples. The addition of 10 % cobalt content to the Li-Ni-Mn-O pseudo-ternary system caused the layered-rocksalt single-phase region to decrease in size for both cooling rates. For all compositions investigated, the single-phase layered and rocksalt regions remained significantly larger for quenched samples than corresponding regular-cooled samples. At 20 % cobalt content, the hexagonal layered single-phase region for regular-cooled samples did not extend to the Mn axis as it was found to contain layered-layered phase

separation, which corroborates the results determined by McCalla [8, 18].

The single-phase cubic spinel region for regular-cooled samples was found to exist at lower Mn contents in every cobalt slice ternary when compared to the corresponding quenched single-phase region. This difference was attributed to the oxygen deficiency of quenched samples that favors the formation of lower oxygen content structures. Within the relevant region of Li-Ni-Mn-Co-O pseudo-quaternary system, the spinel structure ($M_3O_4$) would be favored to form over tetragonal spinel and bixbyite for quenched materials. This effect caused the quenched spinel region to extend to higher Mn contents than the corresponding regular-cooled regions.

Contour plots of layered lattice parameters and calculated unit cell volume per $MO_2$ basis unit were constructed for the cubic spinel and layered-rocksalt single-phase regions of the regular-cooled 10 % cobalt slice ternary. These contour plots indicated a strong negative relationship between lithium content and the resulting unit cell volume of a given single-phase material, regardless if the material is spinel, layered, or rocksalt. There was no discernible effect on the $MO_2$ cell volume when replacing Ni with Mn or vice versa in spinel or layered single-phase structures. A large change in $MO_2$ cell volume was observed in the vicinity of the expected rocksalt-layered phase transition boundary that likely corresponds to the phase transition occurring between the rocksalt and layered structures.

The complex coexistence region existing within the Li-Ni-Mn-Co-O pseudo-quaternary system was briefly investigated by observing the fitted XRD patterns of quenched samples located in the coexistence region near the lower boundary to the spinel region of the 20 % cobalt slice system. The fitted XRD patterns of the multiphase samples indicate the existence of separate spinel-layered and spinel-rocksalt coexistence regions that extend in a currently unknown direction through the pseudo-quaternary system. The existence of such coexistence regions agree with the results found by McCalla in the Li-Ni-Mn-O pseudo-ternary system [8, 9] where separate spinel-rocksalt and spinel-layered coexistence regions were observed.

# Chapter 5

# Conclusion

## 5.1   The Li-Ni-Mn-Co-O Pseudo-Quaternary System

One of the main findings of this work was the determination of the single-phase
spinel and layered compositions existing throughout the 10 %, 20 % and 30 % cobalt
slice ternaries of the Li-Ni-Mn-Co-O pseudo-quaternary system. These single-phase
regions are expected to contain compositions that warrant further study through
electrochemical cycling for interest in finding improved positive electrode materials.
The regions of the Li-Ni-Mn-Co-O pseudo-quaternary system that have currently
been determined consist of the Li-Ni-Mn-O pseudo-ternary system determined by
McCalla [8, 9], the Li-Co-Mn-O pseudo-ternary system determined through the
combination of work by McCalla and the current work [8, 24], and finally the 10 %,
20 % and 30 % cobalt slice ternaries determined by this thesis work. Thus, there still
remains a wide range of unstudied compositions within the Li-Ni-Mn-Co-O
pseudo-quaternary system. Although the regions investigated are believed to have
the most commercially interesting materials due to their low cobalt content, the
higher cobalt slice ternaries would be useful to survey in order to clear some
uncertainties regarding the multiphase regions of the current results. Namely, the
lattice parameters of single-phase compositions in those systems could be used to
characterize the composition of phases in multiphase samples that are currently
unknown. This information might allow for the construction of tie-lines through the
coexistence regions existing within the Li-Ni-Mn-Co-O pseudo-quaternary system.

Cooling rate was shown to have a significant effect on the boundaries to the
single-phase regions in all the ternary systems investigated.   The single-phase
regions corresponding to regular-cooled samples were smaller than samples which
were quenched after heating.   Furthermore, the positions of the regular-cooled
single-phase spinel boundaries were found to shift to lower Mn contents when
compared to the corresponding quenched regions in every ternary system studied.

The same effect was observed in the Li-Co-Mn-O and Li-Ni-Mn-O pseudo-ternary systems [8, 9, 24], which suggests that this is a general effect that cooling rate has on the size and position of single-phase boundaries throughout the Li-Ni-Mn-Co-O pseudo-quaternary system.

## 5.2   Future Work

Besides investigating the uncharted composition regions remaining within the Li-Ni-Mn-Co-O pseudo-quaternary system, there are a wide variety of studies that can be performed using the Pixsys solution-processing robot to synthesize combinatorial samples.    An interesting application would be to perform electrochemical studies on positive electrode materials produced combinatorially. Negative electrode materials have already been studied combinatorially through atomic sputtering methods such as the method used by Fleischauer [50].   The primary challenge for adapting this method to positive electrode materials is that positive electrode materials are difficult to prepare by sputtering. A project seeking to develop 64 channel cycling capabilities for combinatorial positive electrode half cells is currently in the early stages of development.   In order to adopt the 64 channel combinatorial electrochemical method for powders made by the PixSys solutions-processing robot, a reliable transferring method will have to be developed that is able to bind the synthesized powders onto their respective current collectors in a way that facilitates reliable charge and discharge cycling. It is currently difficult to obtain reliable electrochemical cycling data from the positive electrode 64 channel combinatorial cells, but the potential benefits of being able to combinatorially characterize both the structure and electrochemistry of positive electrode materials motivates the research to continue.

Outside of the Li-Ni-Mn-Co-O system, the robot method can be used to study the phase structures of any number of systems. Recent improvements in sodium-ion battery technology, such as sodium layered oxide materials with iron and manganese on the TM layer [51, 52], have increased interest in sodium-ion technology as a potential alternative to lithium-ion batteries.    However, the main issue of combinatorially analyzing the phase regions of these materials are that they

experience more severe sodium loss during synthesis than the lithium loss of lithium-based layered materials. If sodium loss could be reduced or eliminated during synthesis, it would be highly useful to apply combinatorial methods to map out the single-phase regions of the Na-Fe-Mn-O pseudo-ternary system. The results of such a study could lead to finding new materials that enable sodium-ion batteries become an alternative to lithium-ion batteries.

# Bibliography

[1] T. Kim, J. Park, S. K. Change, S. Choi, J. H. Ryu, and H. Song, "The current move of lithium ion batteries toward the next phase," *Advanced Energy Materials*, vol. 2, no. 7, pp. 860–872, 2012.

[2] K. Kang, Y. S. Meng, J. Breger, C. P. Grey, and G. Ceder, "Electrodes with high power and high capacity for rechargeable lithium batteries," *Science*, vol. 311, pp. 977–980, 2006.

[3] J. R. Dahn and G. M. Ehrlich, *Handbook of Batteries, chapter 35.* New York: McGraw-Hill, $3^{rd}$ ed., 2002.

[4] Z. Lu, L. Y. Beaulieu, R. A. Donaberger, C. L. Thomas, and J. R. Dahn, "Synthesis, structure, and electrochemical behaviour of $Li[Ni_xLi_{1/3-2x/3}Mn_{2x/3-x/3}]O_2$," *Journal of the Electrochemical Society*, vol. 149, no. 6, pp. A778–A791, 2002.

[5] Z. Chen and J. R. Dahn, "Improving the capacity retention of $LiCoO_2$ cycled to 4.5 V by heat-treatment," *Electrochemical and Solid-State Letters*, vol. 7, no. 1, pp. A11–A14, 2004.

[6] B. Xu, D. Qian, Z. Wang, and Y. S. Meng, "Recent progress in cathode materials research for advanced lithium ion batteries," *Materials Science and Engineering Review*, vol. 73, pp. 51–65, 2012.

[7] H. Koga, L. Croguennec, P. Mannessiez, M. Ménétrier, F. Weill, L. Bourgeois, M. Duttine, E. Suard, and C. Delmas, "$Li_{1.20}Mn_{0.54}Co_{0.13}Ni_{0.13}O_2$ with different particle sizes as attractive positive electrode materials for lithium-ion batteries: insights into their structure," *The Journal of Physical Chemistry C*, vol. 116, no. 25, pp. 13497–13506, 2012.

[8] E. McCalla, *Consequences of Combinatorial Studies of Positive Electrodes for Li-ion Batteries.* Switzerland: Springer International Publishing, 2014.

[9] E. McCalla, A. W. Rowe, R. Shunmugasundaram, and J. R. Dahn, "Structural study of the Li-Mn-Ni oxide pseudoternary system of interest for positive electrodes of Li-ion batteries," *Chemistry of Materials*, vol. 25, pp. 989–999, 2013.

[10] Y. Gao and J. R. Dahn, "The high temperature phase diagram of $Li_{1+x}Mn_{2-x}O_4$ and its implications," *Journal of the Electrochemical Society*, vol. 143, pp. 1783–1788, 1996.

[11] T. Takada, H. Hayakawa, E. Akiba, F. Izumi, and B. C. Chakoumakos, "Novel synthesis process and structure refinements of $Li_4Mn_5O_{12}$ for rechargeable lithium batteries," *Journal of Power Sources*, vol. 11, no. 2, pp. 613–617, 1997.

[12] J. M. Paulsen and J. R. Dahn, "Phase diagram of Li-Mn-O spinel in air," *Chemistry of Materials*, vol. 11, pp. 3065–3079, 1999.

[13] G. H. Carey and J. R. Dahn, "Combinatorial synthesis of mixed transition metal oxides for lithium ion batteries," *ACS Combinatorial Science*, vol. 13, pp. 186–189, 2011.

[14] S. H. Park, S. H. Kang, C. S. Johnson, K. Amine, and M. M. Thackeray, "Lithium-manganese-nickel-oxide electrodes with integrated layered-spinel structures for lithium batteries," *Electrochemistry Communications*, vol. 9, no. 2, pp. 262–268, 2007.

[15] J. Cababa, S. H. Kang, C. S. Johnson, M. M. Thackeray, and C. P. Grey, "Structural and electrochemical characterization of composite layered-spinel electrodes containing Ni and Mn for Li-ion batteries," *Journal of the Electrochemical Society*, vol. 159, no. 9, pp. A730–A736, 2009.

[16] A. S. Wills, N. P. Raju, and J. E. Greedan, "Low-temperature structure and magnetic properties of the spinel $LiMn_2O_4$: a frustrated antiferromagnet and cathode material," *Chemistry of Materials*, vol. 11, pp. 1510–1518, 1999.

[17] G. B. Jensen and O. V. Nielsen, "The magnetic structure of $Mn_3O_4$ (Hausmannite) between 4.7K and the Néel point, 41K," *Journal of Physics C: Solid State Phys.*, vol. 7, pp. 409–424, 1974.

[18] E. McCalla, C. M. Lowartz, C. R. Brown, and J. R. Dahn, "Formation of layered-layered composites in the Li-Co-Mn oxide pseudoternary system during slow cooling," *Chemistry of Materials*, vol. 25, pp. 912–918, 2013.

[19] B. R. Long, J. R. Croy, F. Dogan, M. R. Suchomel, B. Key, J. Wen, D. J. Miller, M. M. Thackeray, and M. Balasumbramanian, "Effect of cooling rates on phase separation in $0.5Li_2MnO_3 \cdot 0.5LiCoO_2$ electrode materials for Li-ion batteries," *Chemistry of Materials*, vol. 26, pp. 3565–3572, 2014.

[20] J. M. Amarilla, J. L. Martin de Vidales, and R. M. Rojas, "Electrochemical characteristics of cobalt-doped $LiCo_yMn_{2-y}O_4$ ($0 \leq y \leq 0.66$) spinels synthesized at low temperature from $Co_xMn_{3-x}O_4$ precursors," *Solid State Ionics*, vol. 127, pp. 73–81, 2000.

[21] L. Guohua, H. Ikuta, T. Uchida, and M. Wakihara, "The spinel phases $LiM_yMn_{2-y}O_4$ (M=Co, Cr, Ni) as the cathode for rechargeable lithium batteries," *Journal of the Electrochemical Society*, vol. 143, no. 1, pp. 178–182, 1996.

[22] H. Kawai, M. Nagata, H. Kageyama, H. Tukamoto, and A. R. West, "5 V lithium cathodes based on spinel solid solutions $Li_2Co_{1+x}Mn_{3-x}O_8$: $-1 \leq x \leq 1$," *Electrochemica Acta*, vol. 45, no. 1, pp. 315–327, 1999.

[23] E. Aukrust and A. Muan, "Thermodynamic properties of solid solutions with spine-type structure. The system $Co_3O_4 - Mn_3O_4$," *Transactions of the Metallurgical Society of AIME*, vol. 230, pp. 378–382, 1964.

[24] C. R. Brown, E. McCalla, and J. R. Dahn, "Analysis of the cubic spinel region of the Li-Co-Mn oxide pseudo-ternary system," *Solid State Ionics*, vol. 253, pp. 234–238, 2013.

[25] E. McCalla, G. H. Carey, and J. R. Dahn, "Lithium loss mechanisms during synthesis of layered $Li_xNi_{2-x}O_2$ for lithium ion batteries," *Solid State Ionics*, vol. 219, pp. 11–19, 2012.

[26] J. R. Dahn, U. V. Sacken, and C. A. Michal, "Structure and electrochemistry of $Li_{1+y}NiO_2$ and a new $Li_2NiO_2$ phase with the $Ni(OH)_2$ structure," *Solid State Ionics*, vol. 44, no. 1, pp. 87–97, 1990.

[27] R. Moshtev, P. Zlatilova, V. Manev, and K. Tagawa, "Synthesis of $LiNiO_2$ in air atmosphere: x-ray diffraction characterization and electrochemical investigation," *Journal of Power Sources*, vol. 62, no. 1, pp. 59–66, 1996.

[28] W. Li, J. N. Reimers, and J. R. Dahn, "Crystal structure of $Li_xNi_{2-x}O_2$ and a lattice-gas model for the order-disorder transition," *Physical Review B*, vol. 46, no. 6, pp. 3236–3246, 1992.

[29] E. McCalla, A. W. Rowe, J. Camardese, and J. R. Dahn, "The role of metal site vacancies in promoting Li-Mn-Ni-O layered solid solutions," *Chemistry of Materials*, vol. 25, no. 13, pp. 2716–2721, 2013.

[30] G. Q. Liu, L. Wen, and Y. M. Liu, "Spinel $LiNi_{0.5}Mn_{1.5}O_4$ and its derivatives as cathodes for high-voltage Li-ion batteries," *Journal of Solid State Electrochemistry*, vol. 14, pp. 2191–2202, 2010.

[31] Q. Zhong, A. Bonakdarpour, M. Zhang, Y. Gao, and J. R. Dahn, "Synthesis and electrochemistry of $LiNi_xMn_{2-x}O_4$," *Journal of The Electrochemical Society*, vol. 144, no. 1, pp. 205–213, 1997.

[32] J. Cabana, M. C. Cabanas, F. O. Omenya, N. A. Chernova, D. Zeng, M. S. Whittingham, and C. P. Grey, "Composition-structure relationships in the Li-ion battery electrode material $LiNi_{0.5}Mn_{1.5}O_4$," *Chemistry of Materials*, vol. 24, no. 15, pp. 2952–2964, 2012.

[33] Y. Idemotot, H. Narai, and N. Koura, "Crystal structure and cathode performance dependence on oxygen content of $LiMn_{1.5}Ni_{0.5}O_4$ as a cathode material for secondary lithium batteries," *Journal of Power Sources*, vol. 119, pp. 125–129, 2003.

[34] S. H. Park, S. W. Oh, S. H. Kang, I. Belharouak, K. Amine, and Y. K. Sun, "Comparative study of different crystallographic structure of $LiNi_{0.5}Mn_{1.5}O_{4-\delta}$ cathodes with wide operation voltage (2.0-5.0 V)," *Electrochemica Acta*, vol. 52, no. 25, pp. 7226–7230, 2007.

[35] J. M. Tarascon, W. R. McKinnon, F. Coowar, T. N. Bowmer, G. Amatucci, and D. Guyomard, "Synthesis conditions and oxygen stoichiometry effects on Li insertion into the spinel $LiMn_2O_4$," *Journal of The Electrochemical Society*, vol. 141, no. 6, pp. 1421–1431, 1994.

[36] S. T. Myung, S. Komaba, N. Kumagai, H. Yashiro, H. T. Chung, and T. H. Cho, "Nano-crystalline $LiNi_{0.5}Mn_{1.5}O_4$ synthesized by emulsion drying method," *Electrochemica Acta*, vol. 47, no. 15, pp. 2543–2549, 2002.

[37] T. Ohzuku and Y. Makumura, "Layered lithium insertion material of $LiCo_{1/3}Ni_{1/3}mn_{1/3}O_2$ for lithium-ion batteries," *Chemistry Letters*, vol. 30, no. 7, pp. 642–643, 2001.

[38] X. Zhang, W. J. Jiang, A. Mauger, L. Qi, F. Gendron, and C. M. Julien, "Minimization of the cation mixing in $Li_{1+x}(NMC)_{1-x}O_2$ as cathode material," *Journal of Power Sources*, vol. 195, no. 5, pp. 1292–1301, 2010.

[39] N. V. Kosova, E. T. Devyatkina, and V. V. Kaichev, "Optimization of $Ni^{2+}/Ni^{3+}$ ratio in layered $Li(Ni, Mn, Co)O_2$ cathodes for better electrochemistry," *Journal of Power Sources*, vol. 174, no. 2, pp. 965–969, 2007.

[40] P. He, H. Wang, L. Qi, and T. Osaka, "Electrochemical characteristics of layered $LiNi_{1/3}Co_{1/3}Mn_{1/3}O_2$ and with different synthesis conditions," *Journal of Power Sources*, vol. 160, no. 1, pp. 627–632, 2006.

[41] Y. Cho, S. Lee, Y. Lee, T. Hong, and J. Cho, "Spinel-layered core-shell cathode materials for Li-ion batteries," *Advanced Energy Materials*, vol. 1, no. 5, pp. 821–828, 2011.

[42] S. J. Chipera and D. L. Bish, "Fitting full x-ray diffraction patterns for quantitative analysis: a method for readily quantifying crystalline and disordered phases," *Advances in Material Physics and Chemistry*, vol. 3, pp. 47–53, 2013.

[43] B. D. Cullity and S. R. Stock, *Elements of x-ray diffraction*. Upper Saddle River, NJ: Prentice Hall, $2^{nd}$ ed., 2005.

[44] F. Cser, "About the Lorentz correction used in the interpretation of small angle x-ray scattering data of semicrystalline polymers," *Applied Polymer Science*, vol. 80, pp. 2300–2308, 2000.

[45] C. Kittel, *Introduction to Solid State Physics*. Hoboken, NJ: Wiley, $8^{th}$ ed., 2005.

[46] V. F. Sears and S. A. Shelley, "Debye-waller factor for elemental crystals," *Acta Crystallographica*, vol. A47, pp. 441–446, 1991.

[47] L. M. Peng, G. Ren, S. L. Dudarev, and M. J. Whelan, "Debye-Waller factors and absorptive scattering factors of elemental crystals," *Acta Crystallographica*, vol. A52, pp. 456–470, 1996.

[48] P. R. Bevington, *Data reduction and error analysis for the physical sciences*. New York: McGraw Hill, 1969.

[49] B. E. Warren, *X-Ray Diffraction*. New York: Dover Publications, 1990.

[50] M. Fleischauer and J. R. Dahn, "Combinatorial investigations of the Si-Al-Mn system for Li-ion battery applications," *Journal of The Electrochemical Society*, vol. 151, no. 8, pp. A1216–A1221, 2004.

[51] M. D. Slater, D. Kim, E. Lee, and C. S. Johnson, "Sodium-ion batteries," *Advanced Functional Materials*, vol. 23, no. 8, pp. 947–958, 2013.

[52] J. Thorne, R. Dunlap, and M. Obrovac, "Structure and electrochemistry of $Na_xFe_xMn_{1-x}O_2$ $(1.0 \leq x \leq 0.5)$ for Na-ion battery positive electrodes," *Journal of The Electrochemical Society*, vol. 160, no. 2, pp. A361–A367, 2013.

# Appendix A

**Table A.1:** List of hexagonal lattice parameters retrieved from the XRD fits for all single-phase layered compositions in this thesis. The list provides both the $a_{hex}$ and $c_{hex}$ parameters along with their calculated errors $\delta a_{hex}$ and $\delta c_{hex}$. The compositions are written in the format (Li, Ni, Mn, Co), where each atomic symbol is the metallic fraction of the element dispensed in the sample and their values have been rounded to three decimal places. As the initial compositions of these materials lie within the single-phase layered region of this system, the loss of lithium during synthesis is noticeable but not severe and the final compositions are expected to be within 4 % of the reported dispensed compositions. Sample cooling rate is indicated by 'Q' for quenching and 'RC' for regular-cooling.

| Single-Phase Hexagonal Layered | | | | | |
|---|---|---|---|---|---|
| Dispensed Composition | $a_{hex}$ | $\delta a_{hex}$ | $c_{hex}$ | $\delta c_{hex}$ | Cooling Rate |
| (Li, Ni, Mn, Co) | (Å) | (Å) | (Å) | (Å) | (Q or RC) |
| (0.590, 0.311, 0.000, 0.100) | 2.864 | 0.001 | 14.171 | 0.009 | RC |
| (0.558, 0.342, 0.000, 0.100) | 2.879 | 0.001 | 14.207 | 0.022 | RC |
| (0.527, 0.374, 0.000, 0.100) | 2.868 | 0.001 | 14.189 | 0.014 | RC |
| (0.495, 0.405, 0.000, 0.100) | 2.872 | 0.001 | 14.194 | 0.008 | RC |
| (0.450, 0.450, 0.000, 0.100) | 2.926 | 0.003 | 14.364 | 0.027 | RC |
| (0.360, 0.540, 0.000, 0.100) | 2.927 | 0.009 | 14.363 | 0.052 | RC |
| (0.270, 0.630, 0.000, 0.100) | 2.937 | 0.002 | 14.398 | 0.005 | RC |
| (0.180, 0.720, 0.000, 0.100) | 2.942 | 0.007 | 14.443 | 0.039 | RC |
| (0.090, 0.810, 0.000, 0.100) | 2.951 | 0.006 | 14.476 | 0.020 | RC |
| (0.000, 0.900, 0.000, 0.100) | 2.955 | 0.001 | 14.496 | 0.001 | RC |
| (0.590, 0.279, 0.032, 0.100) | 2.860 | 0.001 | 14.176 | 0.012 | RC |
| (0.558, 0.311, 0.032, 0.100) | 2.864 | 0.001 | 14.194 | 0.007 | RC |
| (0.527, 0.342, 0.032, 0.100) | 2.869 | 0.001 | 14.199 | 0.008 | RC |
| (0.495, 0.374, 0.032, 0.100) | 2.873 | 0.001 | 14.203 | 0.010 | RC |
| (0.590, 0.248, 0.063, 0.100) | 2.861 | 0.001 | 14.192 | 0.013 | RC |
| (0.558, 0.279, 0.063, 0.100) | 2.860 | 0.001 | 14.189 | 0.009 | RC |
| (0.527, 0.311, 0.063, 0.100) | 2.869 | 0.001 | 14.208 | 0.013 | RC |
| (0.495, 0.342, 0.063, 0.100) | 2.872 | 0.001 | 14.207 | 0.010 | RC |

**Continued on next page**

81

**Table A.1 – continued from previous page**

| Dispensed Composition (Li, Ni, Mn, Co) | $a_{hex}$ (Å) | $\delta a_{hex}$ (Å) | $c_{hex}$ (Å) | $\delta c_{hex}$ (Å) | Cooling Rate (Q or RC) |
|---|---|---|---|---|---|
| (0.450, 0.360, 0.090, 0.100) | 2.914 | 0.002 | 14.302 | 0.027 | RC |
| (0.180, 0.630, 0.090, 0.100) | 2.946 | 0.003 | 14.483 | 0.017 | RC |
| (0.090, 0.720, 0.090, 0.100) | 2.949 | 0.003 | 14.466 | 0.020 | RC |
| (0.590, 0.216, 0.095, 0.100) | 2.854 | 0.001 | 14.188 | 0.007 | RC |
| (0.558, 0.248, 0.095, 0.100) | 2.860 | 0.001 | 14.207 | 0.002 | RC |
| (0.527, 0.279, 0.095, 0.100) | 2.865 | 0.001 | 14.215 | 0.006 | RC |
| (0.495, 0.311, 0.095, 0.100) | 2.871 | 0.001 | 14.221 | 0.007 | RC |
| (0.653, 0.122, 0.126, 0.100) | 2.845 | 0.001 | 14.196 | 0.008 | RC |
| (0.621, 0.153, 0.126, 0.100) | 2.865 | 0.001 | 14.230 | 0.008 | RC |
| (0.590, 0.185, 0.126, 0.100) | 2.878 | 0.001 | 14.293 | 0.009 | RC |
| (0.558, 0.216, 0.126, 0.100) | 2.861 | 0.001 | 14.212 | 0.005 | RC |
| (0.527, 0.248, 0.126, 0.100) | 2.885 | 0.002 | 14.312 | 0.014 | RC |
| (0.495, 0.279, 0.126, 0.100) | 2.875 | 0.001 | 14.240 | 0.013 | RC |
| (0.653, 0.090, 0.158, 0.100) | 2.843 | 0.001 | 14.193 | 0.011 | RC |
| (0.621, 0.122, 0.158, 0.100) | 2.863 | 0.001 | 14.246 | 0.008 | RC |
| (0.590, 0.153, 0.158, 0.100) | 2.870 | 0.001 | 14.261 | 0.008 | RC |
| (0.558, 0.185, 0.158, 0.100) | 2.864 | 0.001 | 14.226 | 0.008 | RC |
| (0.527, 0.216, 0.158, 0.100) | 2.883 | 0.001 | 14.303 | 0.009 | RC |
| (0.495, 0.248, 0.158, 0.100) | 2.877 | 0.001 | 14.252 | 0.009 | RC |
| (0.630, 0.090, 0.180, 0.100) | 2.852 | 0.002 | 14.213 | 0.014 | RC |
| (0.585, 0.135, 0.180, 0.100) | 2.861 | 0.001 | 14.242 | 0.009 | RC |
| (0.540, 0.180, 0.180, 0.100) | 2.869 | 0.001 | 14.267 | 0.007 | RC |
| (0.495, 0.225, 0.180, 0.100) | 2.869 | 0.001 | 14.249 | 0.007 | RC |
| (0.675, 0.000, 0.225, 0.100) | 2.834 | 0.001 | 14.198 | 0.011 | RC |
| (0.630, 0.045, 0.225, 0.100) | 2.846 | 0.001 | 14.216 | 0.010 | RC |
| (0.585, 0.090, 0.225, 0.100) | 2.851 | 0.001 | 14.225 | 0.007 | RC |
| (0.540, 0.135, 0.225, 0.100) | 2.859 | 0.001 | 14.247 | 0.008 | RC |

**Continued on next page**

Table A.1 – continued from previous page

| Dispensed Composition (Li, Ni, Mn, Co) | $a_{hex}$ (Å) | $\delta a_{hex}$ (Å) | $c_{hex}$ (Å) | $\delta c_{hex}$ (Å) | Cooling Rate (Q or RC) |
|---|---|---|---|---|---|
| (0.450, 0.450, 0.000, 0.100) | 2.879 | 0.001 | 14.212 | 0.005 | Q |
| (0.360, 0.540, 0.000, 0.100) | 2.904 | 0.003 | 14.236 | 0.023 | Q |
| (0.270, 0.630, 0.000, 0.100) | 2.919 | 0.019 | 14.311 | 0.051 | Q |
| (0.180, 0.720, 0.000, 0.100) | 2.942 | 0.003 | 14.424 | 0.015 | Q |
| (0.090, 0.810, 0.000, 0.100) | 2.943 | 0.001 | 14.368 | 0.005 | Q |
| (0.000, 0.900, 0.000, 0.100) | 2.947 | 0.002 | 14.478 | 0.006 | Q |
| (0.540, 0.270, 0.090, 0.100) | 2.855 | 0.001 | 14.174 | 0.005 | Q |
| (0.450, 0.360, 0.090, 0.100) | 2.871 | 0.001 | 14.204 | 0.005 | Q |
| (0.180, 0.630, 0.090, 0.100) | 2.940 | 0.006 | 14.438 | 0.027 | Q |
| (0.090, 0.720, 0.090, 0.100) | 2.943 | 0.001 | 14.364 | 0.005 | Q |
| (0.585, 0.135, 0.180, 0.100) | 2.847 | 0.001 | 14.197 | 0.006 | Q |
| (0.540, 0.180, 0.180, 0.100) | 2.861 | 0.001 | 14.214 | 0.009 | Q |
| (0.495, 0.225, 0.180, 0.100) | 2.868 | 0.001 | 14.256 | 0.009 | Q |
| (0.630, 0.045, 0.225, 0.100) | 2.837 | 0.001 | 14.193 | 0.007 | Q |
| (0.585, 0.090, 0.225, 0.100) | 2.844 | 0.001 | 14.201 | 0.008 | Q |
| (0.540, 0.135, 0.225, 0.100) | 2.859 | 0.001 | 14.231 | 0.009 | Q |
| (0.630, 0.000, 0.270, 0.100) | 2.834 | 0.001 | 14.191 | 0.008 | Q |
| (0.585, 0.045, 0.270, 0.100) | 2.843 | 0.001 | 14.205 | 0.010 | Q |
| (0.540, 0.090, 0.270, 0.100) | 2.850 | 0.002 | 14.228 | 0.012 | Q |
| (0.560, 0.240, 0.000, 0.200) | 2.851 | 0.001 | 14.157 | 0.009 | RC |
| (0.160, 0.640, 0.000, 0.200) | 2.932 | 0.005 | 14.391 | 0.045 | RC |
| (0.080, 0.720, 0.000, 0.200) | 2.947 | 0.011 | 14.447 | 0.104 | RC |
| (0.000, 0.800, 0.000, 0.200) | 2.964 | 0.003 | 14.521 | 0.009 | RC |
| (0.560, 0.160, 0.080, 0.200) | 2.849 | 0.001 | 14.172 | 0.010 | RC |
| (0.480, 0.240, 0.080, 0.200) | 2.863 | 0.001 | 14.216 | 0.012 | RC |
| (0.160, 0.560, 0.080, 0.200) | 2.929 | 0.003 | 14.370 | 0.051 | RC |
| (0.600, 0.040, 0.160, 0.200) | 2.837 | 0.001 | 14.171 | 0.011 | RC |

**Table A.1 – continued from previous page**

| Dispensed Composition (Li, Ni, Mn, Co) | $a_{hex}$ (Å) | $\delta a_{hex}$ (Å) | $c_{hex}$ (Å) | $\delta c_{hex}$ (Å) | Cooling Rate (Q or RC) |
|---|---|---|---|---|---|
| (0.560, 0.080, 0.160, 0.200) | 2.846 | 0.001 | 14.197 | 0.009 | RC |
| (0.520, 0.120, 0.160, 0.200) | 2.854 | 0.001 | 14.232 | 0.007 | RC |
| (0.600, 0.000, 0.200, 0.200) | 2.830 | 0.001 | 14.178 | 0.013 | RC |
| (0.480, 0.320, 0.000, 0.200) | 2.859 | 0.001 | 14.168 | 0.013 | Q |
| (0.160, 0.640, 0.000, 0.200) | 2.844 | 0.010 | 14.238 | 0.013 | Q |
| (0.080, 0.720, 0.000, 0.200) | 2.940 | 0.011 | 14.429 | 0.032 | Q |
| (0.000, 0.800, 0.000, 0.200) | 2.965 | 0.001 | 14.529 | 0.004 | Q |
| (0.560, 0.160, 0.080, 0.200) | 2.841 | 0.001 | 14.150 | 0.012 | Q |
| (0.240, 0.480, 0.080, 0.200) | 2.935 | 0.004 | 14.350 | 0.021 | Q |
| (0.160, 0.560, 0.080, 0.200) | 2.946 | 0.004 | 14.437 | 0.017 | Q |
| (0.600, 0.040, 0.160, 0.200) | 2.838 | 0.001 | 14.173 | 0.010 | Q |
| (0.560, 0.080, 0.160, 0.200) | 2.846 | 0.001 | 14.182 | 0.013 | Q |
| (0.520, 0.120, 0.160, 0.200) | 2.852 | 0.002 | 14.189 | 0.026 | Q |
| (0.600, 0.000, 0.200, 0.200) | 2.827 | 0.002 | 14.125 | 0.026 | Q |
| (0.560, 0.040, 0.200, 0.200) | 2.836 | 0.001 | 14.189 | 0.007 | Q |
| (0.520, 0.080, 0.200, 0.200) | 2.846 | 0.001 | 14.230 | 0.005 | Q |
| (0.560, 0.140, 0.000, 0.300) | 2.832 | 0.001 | 14.108 | 0.010 | RC |
| (0.490, 0.210, 0.000, 0.300) | 2.840 | 0.001 | 14.134 | 0.014 | RC |
| (0.070, 0.630, 0.000, 0.300) | 2.953 | 0.030 | 14.468 | 0.101 | RC |
| (0.000, 0.700, 0.000, 0.300) | 2.967 | 0.008 | 14.558 | 0.044 | RC |
| (0.560, 0.070, 0.070, 0.300) | 2.828 | 0.001 | 14.130 | 0.008 | RC |
| (0.490, 0.140, 0.070, 0.300) | 2.846 | 0.001 | 14.170 | 0.010 | RC |
| (0.560, 0.000, 0.140, 0.300) | 2.825 | 0.001 | 14.147 | 0.017 | RC |
| (0.525, 0.035, 0.140, 0.300) | 2.831 | 0.001 | 14.171 | 0.012 | RC |
| (0.490, 0.070, 0.140, 0.300) | 2.837 | 0.001 | 14.194 | 0.010 | RC |
| (0.490, 0.210, 0.000, 0.300) | 2.838 | 0.001 | 14.118 | 0.009 | Q |
| (0.140, 0.560, 0.000, 0.300) | 2.931 | 0.005 | 14.362 | 0.027 | Q |

**Table A.1 – continued from previous page**

| Dispensed Composition (Li, Ni, Mn, Co) | $a_{hex}$ (Å) | $\delta a_{hex}$ (Å) | $c_{hex}$ (Å) | $\delta c_{hex}$ (Å) | Cooling Rate (Q or RC) |
|---|---|---|---|---|---|
| (0.000, 0.700, 0.000, 0.300) | 2.968 | 0.008 | 14.568 | 0.043 | Q |
| (0.560, 0.070, 0.070, 0.300) | 2.829 | 0.001 | 14.128 | 0.010 | Q |
| (0.490, 0.140, 0.070, 0.300) | 2.839 | 0.001 | 14.145 | 0.007 | Q |
| (0.210, 0.420, 0.070, 0.300) | 2.937 | 0.008 | 14.417 | 0.069 | Q |
| (0.560, 0.000, 0.140, 0.300) | 2.828 | 0.001 | 14.156 | 0.018 | Q |
| (0.490, 0.070, 0.140, 0.300) | 2.837 | 0.001 | 14.196 | 0.008 | Q |
| (0.525, 0.035, 0.140, 0.300) | 2.834 | 0.001 | 14.177 | 0.012 | Q |
| (0.490, 0.035, 0.175, 0.300) | 2.832 | 0.001 | 14.200 | 0.003 | Q |

**Table A.2:** List of cubic lattice parameters retrieved from the XRD fits for all single-phase spinel compositions in this thesis. The list provides the fitted $a_{cub}$ parameter along with its calculated error $\delta a_{cub}$. The compositions are written in the format (Li, Ni, Mn, Co), where each atomic symbol is the metallic fraction of the element dispensed in the sample and their values have been rounded to three decimal places. Since lithium loss during synthesis is negligible for these materials, the final compositions are expected to be within 3 % of the reported dispensed compositions as explained in Sections 2.6 and 4.2. Sample cooling rate is indicated by 'Q' for quenching and 'RC' for regular-cooling.

| Single-Phase Cubic Spinel | | | |
|---|---|---|---|
| Dispensed Composition (Li, Ni, Mn, Co) | $a_{cub}$ (Å) | $\delta a_{cub}$ (Å) | Cooling Rate (Q or RC) |
| (0.171, 0.225, 0.504, 0.100) | 8.261 | 0.002 | RC |
| (0.137, 0.252, 0.511, 0.100) | 8.276 | 0.002 | RC |
| (0.103, 0.279, 0.518, 0.100) | 8.308 | 0.002 | RC |
| (0.068, 0.306, 0.526, 0.100) | 8.317 | 0.002 | RC |
| (0.034, 0.333, 0.533, 0.100) | 8.336 | 0.002 | RC |
| (0.000, 0.360, 0.540, 0.100) | 8.354 | 0.003 | RC |
| (0.171, 0.198, 0.531, 0.100) | 8.281 | 0.002 | RC |
| (0.137, 0.225, 0.538, 0.100) | 8.299 | 0.002 | RC |

Table A.2 – continued from previous page

| Dispensed Composition (Li, Ni, Mn, Co) | $a_{cub}$ (Å) | $\delta a_{cub}$ (Å) | Cooling Rate (Q or RC) |
|---|---|---|---|
| (0.103, 0.252, 0.545, 0.100) | 8.323 | 0.003 | RC |
| (0.068, 0.279, 0.553, 0.100) | 8.340 | 0.003 | RC |
| (0.034, 0.306, 0.560, 0.100) | 8.341 | 0.002 | RC |
| (0.000, 0.333, 0.567, 0.100) | 8.367 | 0.003 | RC |
| (0.171, 0.171, 0.558, 0.100) | 8.270 | 0.003 | RC |
| (0.364, 0.036, 0.500, 0.100) | 8.151 | 0.002 | RC |
| (0.329, 0.072, 0.499, 0.100) | 8.167 | 0.002 | RC |
| (0.295, 0.108, 0.497, 0.100) | 8.189 | 0.002 | RC |
| (0.261, 0.144, 0.495, 0.100) | 8.210 | 0.002 | RC |
| (0.227, 0.180, 0.493, 0.100) | 8.229 | 0.002 | RC |
| (0.364, 0.000, 0.536, 0.100) | 8.153 | 0.002 | RC |
| (0.329, 0.036, 0.535, 0.100) | 8.164 | 0.002 | RC |
| (0.295, 0.072, 0.533, 0.100) | 8.198 | 0.002 | RC |
| (0.261, 0.108, 0.531, 0.100) | 8.230 | 0.002 | RC |
| (0.227, 0.144, 0.529, 0.100) | 8.245 | 0.002 | RC |
| (0.193, 0.180, 0.527, 0.100) | 8.270 | 0.002 | RC |
| (0.329, 0.000, 0.571, 0.100) | 8.144 | 0.004 | RC |
| (0.295, 0.036, 0.569, 0.100) | 8.203 | 0.002 | RC |
| (0.261, 0.072, 0.567, 0.100) | 8.213 | 0.002 | RC |
| (0.270, 0.090, 0.540, 0.100) | 8.199 | 0.002 | RC |
| (0.180, 0.180, 0.540, 0.100) | 8.258 | 0.002 | RC |
| (0.090, 0.270, 0.540, 0.100) | 8.304 | 0.002 | RC |
| (0.000, 0.360, 0.540, 0.100) | 8.354 | 0.002 | RC |
| (0.315, 0.090, 0.495, 0.100) | 8.145 | 0.002 | RC |
| (0.270, 0.135, 0.495, 0.100) | 8.167 | 0.003 | RC |
| (0.315, 0.045, 0.540, 0.100) | 8.131 | 0.003 | RC |
| (0.270, 0.090, 0.540, 0.100) | 8.196 | 0.002 | RC |

**Table A.2 – continued from previous page**

| Dispensed Composition (Li, Ni, Mn, Co) | $a_{cub}$ (Å) | $\delta a_{cub}$ (Å) | Cooling Rate (Q or RC) |
|---|---|---|---|
| (0.315, 0.000, 0.585, 0.100) | 8.159 | 0.004 | RC |
| (0.270, 0.045, 0.585, 0.100) | 8.192 | 0.003 | RC |
| (0.270, 0.135, 0.495, 0.100) | 8.200 | 0.002 | Q |
| (0.270, 0.090, 0.540, 0.100) | 8.222 | 0.001 | Q |
| (0.180, 0.180, 0.540, 0.100) | 8.264 | 0.002 | Q |
| (0.090, 0.270, 0.540, 0.100) | 8.314 | 0.001 | Q |
| (0.000, 0.360, 0.540, 0.100) | 8.356 | 0.002 | Q |
| (0.270, 0.045, 0.585, 0.100) | 8.209 | 0.002 | Q |
| (0.270, 0.000, 0.630, 0.100) | 8.226 | 0.001 | Q |
| (0.180, 0.090, 0.630, 0.100) | 8.239 | 0.006 | Q |
| (0.240, 0.160, 0.400, 0.200) | 8.167 | 0.002 | RC |
| (0.320, 0.040, 0.440, 0.200) | 8.120 | 0.002 | RC |
| (0.280, 0.080, 0.440, 0.200) | 8.149 | 0.002 | RC |
| (0.240, 0.120, 0.440, 0.200) | 8.193 | 0.002 | RC |
| (0.320, 0.000, 0.480, 0.200) | 8.139 | 0.002 | RC |
| (0.280, 0.040, 0.480, 0.200) | 8.175 | 0.001 | RC |
| (0.240, 0.080, 0.480, 0.200) | 8.213 | 0.001 | RC |
| (0.160, 0.160, 0.480, 0.200) | 8.244 | 0.002 | RC |
| (0.240, 0.160, 0.400, 0.200) | 8.206 | 0.002 | Q |
| (0.240, 0.120, 0.440, 0.200) | 8.198 | 0.002 | Q |
| (0.160, 0.160, 0.480, 0.200) | 8.233 | 0.001 | Q |
| (0.240, 0.080, 0.480, 0.200) | 8.207 | 0.002 | Q |
| (0.280, 0.000, 0.520, 0.200) | 8.208 | 0.002 | Q |
| (0.240, 0.040, 0.520, 0.200) | 8.229 | 0.002 | Q |
| (0.240, 0.000, 0.560, 0.200) | 8.244 | 0.003 | Q |
| (0.160, 0.080, 0.560, 0.200) | 8.287 | 0.002 | Q |
| (0.080, 0.160, 0.560, 0.200) | 8.317 | 0.002 | Q |

**Table A.2 – continued from previous page**

| Dispensed Composition (Li, Ni, Mn, Co) | $a_{cub}$ (Å) | $\delta a_{cub}$ (Å) | Cooling Rate (Q or RC) |
|---|---|---|---|
| (0.000, 0.240, 0.560, 0.200) | 8.351 | 0.002 | Q |
| (0.210, 0.140, 0.350, 0.300) | 8.153 | 0.002 | RC |
| (0.140, 0.210, 0.350, 0.300) | 8.222 | 0.002 | RC |
| (0.210, 0.105, 0.385, 0.300) | 8.168 | 0.002 | RC |
| (0.210, 0.070, 0.420, 0.300) | 8.179 | 0.001 | RC |
| (0.000, 0.280, 0.420, 0.300) | 8.317 | 0.004 | RC |
| (0.245, 0.000, 0.455, 0.300) | 8.140 | 0.002 | RC |
| (0.140, 0.140, 0.420, 0.300) | 8.248 | 0.002 | Q |
| (0.070, 0.210, 0.420, 0.300) | 8.315 | 0.002 | Q |
| (0.000, 0.280, 0.420, 0.300) | 8.307 | 0.004 | Q |
| (0.210, 0.035, 0.455, 0.300) | 8.212 | 0.002 | Q |
| (0.210, 0.000, 0.490, 0.300) | 8.208 | 0.002 | Q |
| (0.140, 0.070, 0.490, 0.300) | 8.269 | 0.002 | Q |

# Appendix B

# License Details

Thank you very much for your order.

This is a License Agreement between Colby R Brown ("You") and Elsevier ("Elsevier"). The license consists of your order details, the terms and conditions provided by Elsevier, and the payment terms and conditions.

Get the printable license.

| | |
|---|---|
| License Number | 3481440165510 |
| License date | Oct 03, 2014 |
| Order Content Publisher | Elsevier |
| Order Content Publication | Solid State Ionics |
| Order Content Title | Analysis of the cubic spinel region of the Li–Co–Mn oxide pseudo-ternary system |
| Order Content Author | Colby R. Brown,E. McCalla,J.R. Dahn |
| Order Content Date | 15 December 2013 |
| Licensed content volume number | 253 |
| Licensed content issue number | n/a |
| Number of pages | 5 |
| Type of Use | reuse in a thesis/dissertation |
| Portion | figures/tables/illustrations |
| Number of figures/tables/illustrations | 6 |
| Format | both print and electronic |
| Are you the author of this Elsevier article? | Yes |
| Will you be translating? | No |
| Title of your thesis/dissertation | Combinatorial Study of the Li-Ni-Mn-Co Oxide Pseudo-Quaternary System for Use in Li-Ion Battery Materials Research |
| Expected completion date | Nov 2014 |
| Estimated size (number of pages) | 90 |
| Elsevier VAT number | GB 494 6272 12 |
| Price | 0.00 USD |
| VAT/Local Sales Tax | 0.00 USD / 0.00 GBP |
| Total | **0.00 USD** |